D3.8 Verification Report for Demos 2, 3 and 4

Primary Author(s)	Leon Tolksdorf | TH Ingolstadt
	Lars Schories | ZF Friedrichshafen AG
	Jacint Castells | Applus IDIADA
	Ioannis Gragopoulos | CERTH
	Carina Vogl | CARIAD SE
	Mouna Karoui | CEA

Related Work Package	WP3
Version/Status	1.4 | Final version
Issue date	30.05.2023
Deliverable type	R
Dissemination Level	PU

Project Acronym	SAFE-UP
Project Title	proactive SAFEty systems and tools for a constantly UPgrading road environment
Project Website	www.safeup.eu
Project Coordinator	Núria Parera | Applus IDIADA
Grant Agreement No.	861570

This project has received funding from the European Union's Horizon 2020 research and innovation programme under Grant Agreement 861570.

Co-Authors

Name	Organisation
Daniel Weihmayr	THI
Robin Smit	TNO
Timm Gloger	Robert Bosch GmbH
Sylvie Mayrargue	CEA
Johann Stoll	CARIAD SE
Kristin Blum	CARIAD SE
Manuel Muñoz Sánchez	TU/e
Valérian Mannoni	CEA
Benoît Denis	CEA

Reviewers

Version	Date	Reviewer (Name/Organisation)	Action (Checked/Approved)
1.3	09/05/2023	Harald Kolk (Vif)	approved
1.3	16/05/2023	Christian Birkner (THI)	approved
1.3	16/05/2023	Jacint Castells	approved

Document Distribution

Version	Date	Distributed to
1.4	30/05/2023	Coordination Team
1.4	30/05/2023	Submission in the EC System
		Approved by the EC

This project has received funding from the European Union's Horizon 2020 research and innovation programme under Grant Agreement 861570.

Copyright statement

This project has received funding from the European Union's Horizon 2020 research and innovation programme under Grant Agreement 861570.

Executive summary

The SAFE-UP project aims to proactively address the novel safety challenges of the future mobility systems through the development of tools and innovative safety methods that lead to improvements in road transport safety.

Future mobility systems will rely on partially and fully automated vehicles to reduce traffic collisions and casualties by removing causal factors like driver distraction, fatigue or infractions and by reacting autonomously to emergency situations. On the other hand, they may introduce new collision risk factors or risky behaviours when interacting with other traffic participants. SAFE-UP's Work Package 3 is handling the "Active safety systems for vehicle-VRU interaction" which is split up into 3 demonstrators.

The first demonstrator of WP3 (Demo 2) analyses and improves the perception of the active safety system in good and in adverse weather conditions. Here, the focus lies on understanding the limitations and improving of object detection algorithms. These are essential for the design of active safety systems, triggering emergency manoeuvres to avoid collisions with VRUs. Directly leading to the second demonstrator, of WP3, namely Demo 3. This demo focuses on developing a functional automated emergency steering (AES) and automated emergency breaking (AEB) system, specifically for the avoidance of VRUs. Additionally, the algorithms are deployed in a functional architecture which coincides with state-of-the-art research in automated driving.

While Demo 3 focuses on a system design, given a collision is detected, the third demonstrator (Demo 4) focuses on preventive measures. Here, Demo 4 uses C-ITS communication for exchanging information and generating warnings for the driver and the VRU. The goal is to transmit a timely warning to all actors in case a collision might occur on the current trajectories.

The objective of this report is to verify the technical characteristics of each Demo. The technical specifications to verify against are provided by previous reports. If no specifications are provided, this report derives metrics that measure the system's performance and quantifies the developed technologies against these metrics, such that future research can build upon the found specifications.

For Demo 2, it is found that the detection of static VRUs under adverse weather can be reasonably well modelled; however, dynamic VRUs leave an open challenge. Another finding is that current testing efforts and capabilities are insufficient for deriving a generalized weather model. Demo 3 successfully demonstrates the capabilities of an in-lane AES+B system. It is also designed such that it can directly enable higher levels of automation. The bottleneck, however, is the inaccuracy of the perception for short observation times leading to false maneuver decisions in some cases. Verifying Demo 4 shows that the assumptions WP5 takes for the overall assessment are technically feasible. The last conclusion is that for future work, it is highly recommended to combine the proposed technologies over Demo 2 – 4 into one system and use this document as a basis for future technical specifications.

This project has received funding from the European Union's Horizon 2020 research and innovation programme under Grant Agreement 861570.

Table of Contents

This project has received funding from the European Union's Horizon 2020 research and innovation programme under Grant Agreement 861570.

List of figures

This project has received funding from the European Union's Horizon 2020 research and innovation programme under Grant Agreement 861570.

This project has received funding from the European Union's Horizon 2020 research and innovation programme under Grant Agreement 861570.

This project has received funding from the European Union’s Horizon 2020 research and innovation programme under Grant Agreement 861570.

This project has received funding from the European Union's Horizon 2020 research and innovation programme under Grant Agreement 861570.

List of tables

This project has received funding from the European Union's Horizon 2020 research and innovation programme under Grant Agreement 861570.

1. Introduction

SAFE-UP's work package 3 is handling the "Active safety systems for vehicle and vulnerable road user interaction" which is tasked with developing three demonstrators. The three demonstrators are denoted Demo 2, Demo 3 and Demo 4 respectively.

Demo 2, as reported in (Löffler, et al., 2021), concerns improving the object detections of vulnerable road users (VRUs) in adverse weather conditions. Demo 3, see (Löffler, et al., 2021), introduces active safety functions, i.e., automated emergency braking (AEB) and automated emergency steering (AES) to avoid collisions with VRUs. Furthermore demo 4, see (Nikolaou, Castells, Lorente Mallada, Gragkopoulos, & Tsetsinas, 2021), proposes an on-time warning interface between a vehicle and VRU in case a potential collision is imminent.

The objective of this report is the technical verification of the individual demos. That is, verifying whether the demos meet technical specifications. We approach this task by utilizing the methodology provided by (ISO 15288 , 2015). The technical specifications are partly provided in the earlier deliverables (Nikolaou, et al., D3.1 Active Safety Systems Specification and Risk Analysis , 2021), (Nikolaou, et al., D3.9 Active Safety Systems Specification and Risk Analysis Update, 2022). Since the demonstrators serve as a proof-of-concept of novel technologies, technical specification is not always given by previous reports. This is due to the nature of researching and exploring new technologies, where the performance outcome is unknown. In cases where technical specifications were not provided, we quantified our systems so that future work could verify their systems against our system's performance. Thus, we also provide novel metrics to measure the system's performance and set the ground for future research, given the prospects of our findings.

The remainder of this report is structured as follows. Section 2 briefly outlines state-of-the-art verification methodologies. Sections 3 – 5 verify and quantify the respective Demos. Lastly, Section 6 concludes the report and provides and provides an outlook for future work.

This project has received funding from the European Union's Horizon 2020 research and innovation programme under Grant Agreement 861570.

2. Verification Methodology

The methodology applied for verification of the developed systems is based on the INCOSE Systems Engineering Handbook (Systems Engineering, 2000) and (ISO 15288 , 2015), which is a guide for System Life Cycle processes and activities. Specifically, the technical process description of the verification shall be used as guideline.

Given the guideline, the verification can be carried out on different system levels, i.e.:

1. overall system
2. sub-system, module
3. component.

Given the context of SAFE-UP, the overall system requirements are the reduction of killed or severely injured (KSI) vulnerable road users (VRUs). The assessment of the impact of the proposed technologies in the reduction of KSI is done in WP5. Thus, the verification and quantification of this report focus on the sub-system, module, and component level. The inputs and outputs of software and hardware components are measured for the module level. For the lowest level, i.e., the component level, we measure the performance of individual algorithms whenever necessary. The necessity of measuring is determined by the expert's knowledge about the criticality of this component for the overall system performance. *For example*, the runtime of complex algorithms is of great importance for real-time decision-making and, hence essential to measure. Contrarily, algorithms performing simple tasks with low complexity do not require measuring since the computational effort of more complex algorithms is relatively greater on the order of multiple magnitudes.

Generally, for the task of verification, several techniques are proposed in (ISO 15288 , 2015), which we apply throughout this report. These are:

- Inspection – no stimuli, visual inspection
- Analysis – analytical evidence, using mathematical or probabilistic calculation
- Demonstration – show correct operation without using physical measurements (test equipment). Observations are made against expected responses
- Test – functional, measurable characteristics with special test equipment
- Analogy or similarity
- Simulation – models and mock-ups (not on physical elements) to show features and performance is met
- Sampling – verification using samples

This project has received funding from the European Union's Horizon 2020 research and innovation programme under Grant Agreement 861570.

3. Demo 2

3.1 High-Level Description

For the demo 2 development, extensive measurements have been performed (see (Löffler, et al., 2021)). The measurements focus on the influence of weather on the perception performance of the test vehicle. Over several measurement campaigns, different weather conditions, target types (VRUs), sensors, and perception algorithms are tested. The obtained data is utilized to develop two simulation models, of which the verification is reported in the following section. The first development is referred to as the *field of view model* (FoV model), and the other development is termed the *weather filter*.

The objective of the FoV model is to understand the impact of weather on the sensor performance and to be able to integrate those effects into simulations. Therefore, a reduced field of view (due to adverse weather conditions) of a sensor suit is implemented in a simulation environment, simulating common scenarios where a vehicle equipped with AEB and AES encounters a VRU, triggering a system response.

The objective of the weather filter is to distort good weather sensor input into a degraded perception performance, which simulates the weather effects on the perception system of an automated vehicle. This task is approached by combining a physical model, representing primary weather effects (e.g., attenuation), with the obtained empirical measurements accounting for secondary weather effects (e.g., rain droplets on sensor surfaces).

3.2 Verification

The verification is split into two parts, where each model is evaluated individually.

3.2.1 Field of View Model

In this chapter, the derived FoV model based on the second measurement campaign (static) described in (Löffler, et al., 2022) is further analyzed in terms of the resulting size reduction of the FoV and the variances of the used radar locations (estimated reflection points from the radar) at different rain intensities. It is followed by an evaluation of the third measurement campaign (dynamic), which is described in (Löffler, et al., 2022) in more detail, and an analysis of the performed simulations, where the FoV models based on static testing are integrated. The chapter concludes with a comparison of the simulative results to the dynamic sensor performances in rainy weather conditions and identifies potential further work.

This project has received funding from the European Union's Horizon 2020 research and innovation programme under Grant Agreement 861570.

3.2.1.1 Field of View Model analysis

The FoV model is derived from the second measurement campaign (static), where a dummy was placed at different positions in relation to the vehicle to assess the detection ability of the sensors. For generating continuous FoVs of the used radar and camera sensor, which can be integrated into simulations, the theoretical shapes of the sensor FoVs are scaled such that they match to the measurement results. Table 1 gives the resulting size and additionally the respective size reduction of the FoV model for the different rain amounts. The results indicate that the camera sensor is more influenced by rain than the radar sensor, as the FoV reduction is clearly larger for the camera sensor than for the radar sensor.

Table 1: Size and respective size reduction of the FoV model for different rain amounts.

	Radar FoV range 0°	**Radar FoV relative size**	**Camera FoV range 0°**	**Camera FoV relative size**
0 mm/h	72.2 m	100 %	70.0 m	100 %
16 mm/h	63.7 m	88.2 %	44.8 m	64.0 %
66 mm/h	54.4 m	75.3 %	38.5 m	55.0 %
98 mm/h	46.6 m	64.5 %	-	-

In the following, variances of the radar locations from the second measurement campaign are analysed to assess if there are effects visible with varying positions or varying rain intensities. The unbiased sample variance is calculated from the x-values of the radar locations inside a defined bounding box as well as from the y-values of the radar locations inside a defined bounding box. To obtain the variances of the radar locations in x-direction, a bounding box of 4 m in x-direction (depth), 1 m in y-direction (width), and 2 m in z-direction (height) is used at the corrected dummy positions for filtering the radar locations. Figure 1 shows the variances for the radar location at the different positions at the angle setting with 0° (car directly facing towards the pedestrian dummy) for 0 mm/h, 16 mm/h, 66 mm/h and 98 mm/h rain. At the two closest positions (1 and 2), the variance increases with increasing rain intensity. However, at higher distances, this effect is not visible. Also, no tendency can be detected, whether the variances increase or decrease with higher distance.

This project has received funding from the European Union's Horizon 2020 research and innovation programme under Grant Agreement 861570.

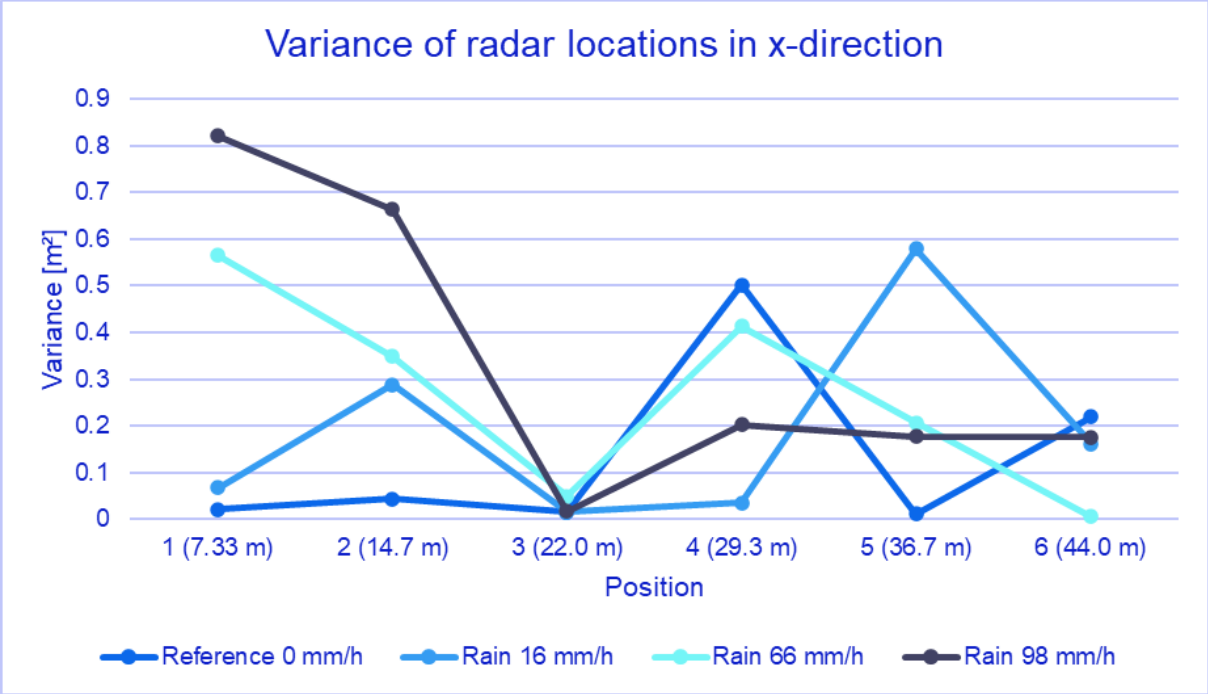

Figure 1: Variance of radar locations from second measurement campaign in x-direction at 0° vehicle rotation.

To obtain the variances of the radar locations in y-direction, a bounding box of 1 m in x-direction (depth), 4 m in y-direction (width), and 2 m in z-direction (height) is placed at the corrected dummy positions for filtering the radar locations. Figure 2 shows the variances for the radar location at the different positions at the angle setting with 0° (car directly facing towards the pedestrian dummy) for 0 mm/h, 16 mm/h, 66 mm/h and 98 mm/h rain. At the two closest positions (1 and 2), the variance increases with increasing rain intensity. However, at higher distances, this order is not always kept. Also, it cannot directly be concluded that the variances increase with higher distance due to several inconsistencies.

It can be summarized that the variance of the radar locations increases with increasing rain intensity in our measurements for the positions with distances of 7.33 m and 14.7 m, but this effect cannot be generalized over all positions. No clear trend has been detected if the variances of radar locations increase or decrease with increasing distance.

This project has received funding from the European Union's Horizon 2020 research and innovation programme under Grant Agreement 861570.

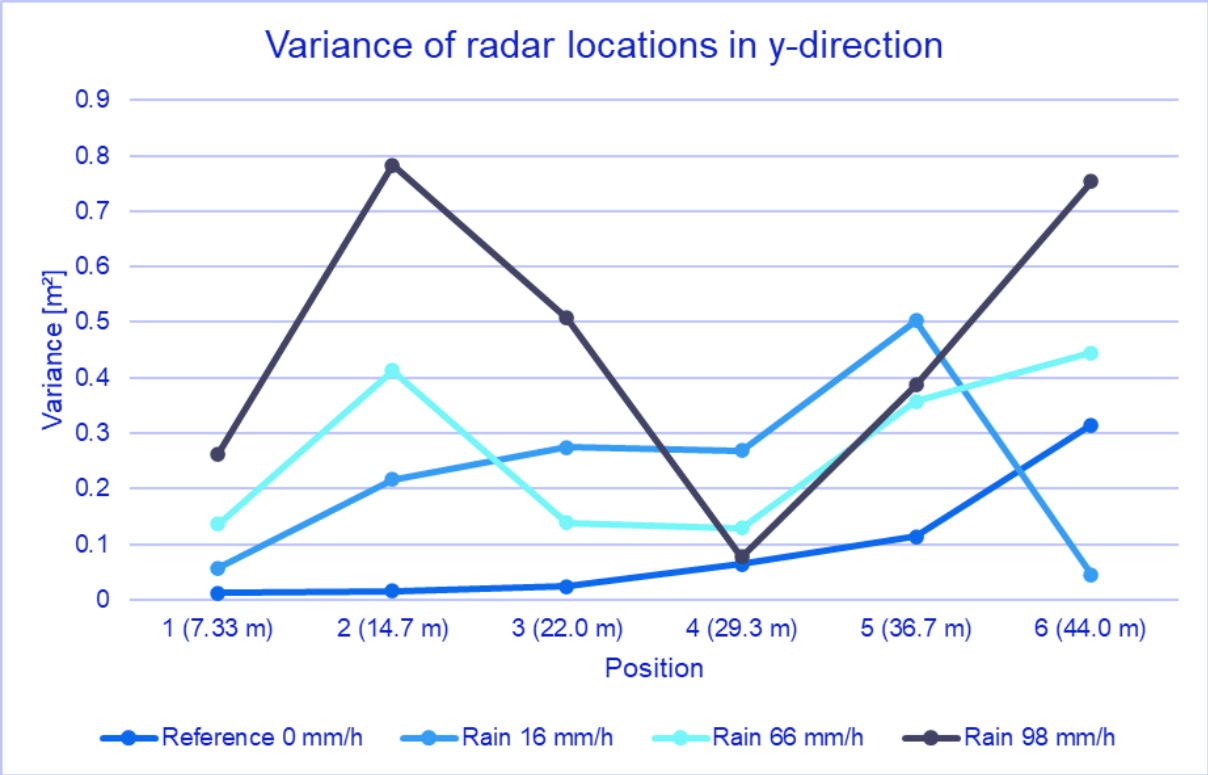

Figure 2: Variance of radar locations from second measurement campaign in y-direction at 0° vehicle rotation.

3.2.1.2 Results of the third/ dynamic measurement campaign

The goal of the third measurement campaign is to generate data to compare the simulative results, where FoV models based on static testing are integrated, with dynamic performances in rainy weather conditions. Therefore, scenarios are selected, which are testable in the rain area of the test hall and are controllable for the test driver in test hall. The measurement setup for one example is shown in Figure 3 and a more detailed description can be found in (Löffler, et al., 2022).

The following parameters are varied and tested leading to eight configurations, which are tested in the third measurement campaign and compared to simulations:

- Target: Pedestrian
- Weather settings: Dry, rain 16 mm/h, rain 66 mm/h, rain 98 mm/h
- Vehicle velocity: 2 configurations near 15 kph and 35 kph, which were controllable by a human driver
- Target velocity: 8 kph (velocity is adjusted based on light barriers)

This project has received funding from the European Union's Horizon 2020 research and innovation programme under Grant Agreement 861570.

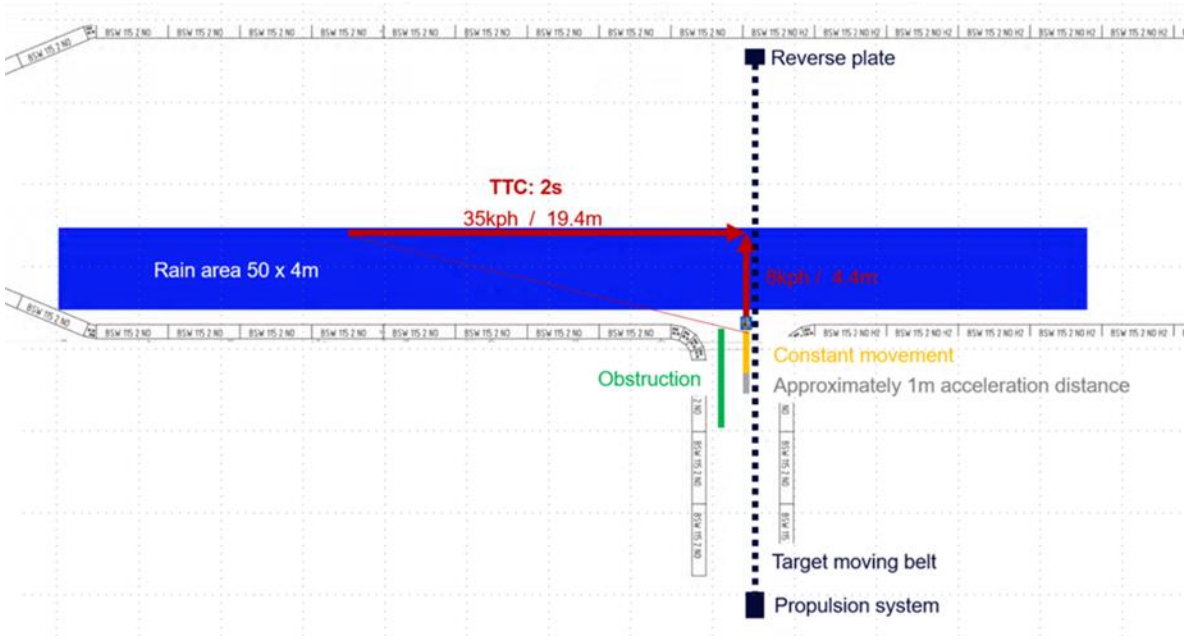

Figure 3: Measurement setup on the example of a mirrored scenario from cluster P-CLwoSO (35 kph vehicle velocity, 8 kph pedestrian velocity, and a TTC of 2 s) (Löffler, et al., 2022).

The focus of the measurement campaign is on the perception performance of the radar and camera sensor of the Demo 3 vehicle. No AEB was triggered in the tests. In the following, the methodology is described how the measurement campaign is evaluated and the results are presented.

At first, the different position data (BOSCH indoor position, THI indoor position, 4activeSystem target position) was transformed into one common coordinate system, which is aligned with the floorplan of the test hall to simplify the visualization. Figure 4 shows the trajectory of the vehicle in blue according to the THI position information, the trajectory of the moving vehicle in red according to BOSCH position information, and the trajectory of the moving pedestrian target in yellow according to the propulsion system information. Additionally, the target moving belt is visualized with a long blue line, the wall for obstructing the target outside the rain area with a short blue line, and the rain area of the test hall with a blue rectangle. The vehicle trajectories are recorded by a rover, which is mounted in the middle of the vehicle roof with a distance to the radar sensor/vehicle front of + 2.4 m and a distance to the camera sensor of + 0.74 m.

This project has received funding from the European Union's Horizon 2020 research and innovation programme under Grant Agreement 861570.

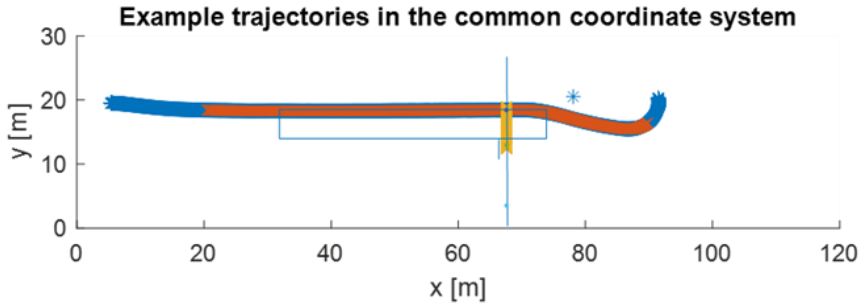

Figure 4: Test setup and trajectories transformed into one common coordinate system aligned with the test hall walls for one example test case (blue trajectory - THI indoor position, red trajectory - BOSCH indoor position, yellow trajectory – 4activeSystem target position).

As the target propulsion system had no GPS connection in the test hall and it was not possible with the available equipment to connect the target propulsion system to the test hall indoor positioning system, also synchronized UTC timestamps are missing for the target positions. Hence, the time recorded by the vehicle and the time recorded by the target needed to be aligned. Therefore, the timestamp, when the front wheels drive over the target belt according to the position information of the vehicle, and the timestamp, when the dummy velocity suddenly decreases (by - 6 kph in 20 ms), are matched. There is a mechanism of the propulsion system to stop, when the belt is shortly blocked. However, with this approach small errors in the time alignment can occur, especially due to the sampling rate at which the position of the vehicle is available (each 20 ms) and the sampling rate at which the velocity information of the target is available (each 10 ms).

As the focus for the comparison to simulative results is on the perception performance of the radar and camera sensor of the Demo 3 vehicle, particularly interesting is the time information at which the pedestrian target is available in the object lists. Therefore, at first the time stamps and positions of the vehicle are identified for each test case at which the respective sensor is theoretically able to detect the pedestrian. This is defined as when the line between the investigated sensor and the target is no longer discontinued by the obstruction wall. In Figure 5 the parts of the trajectories are shown, where the respective sensor is theoretically able to see the target for test case ID 1 (see Table 2 for test case list).

This project has received funding from the European Union's Horizon 2020 research and innovation programme under Grant Agreement 861570.

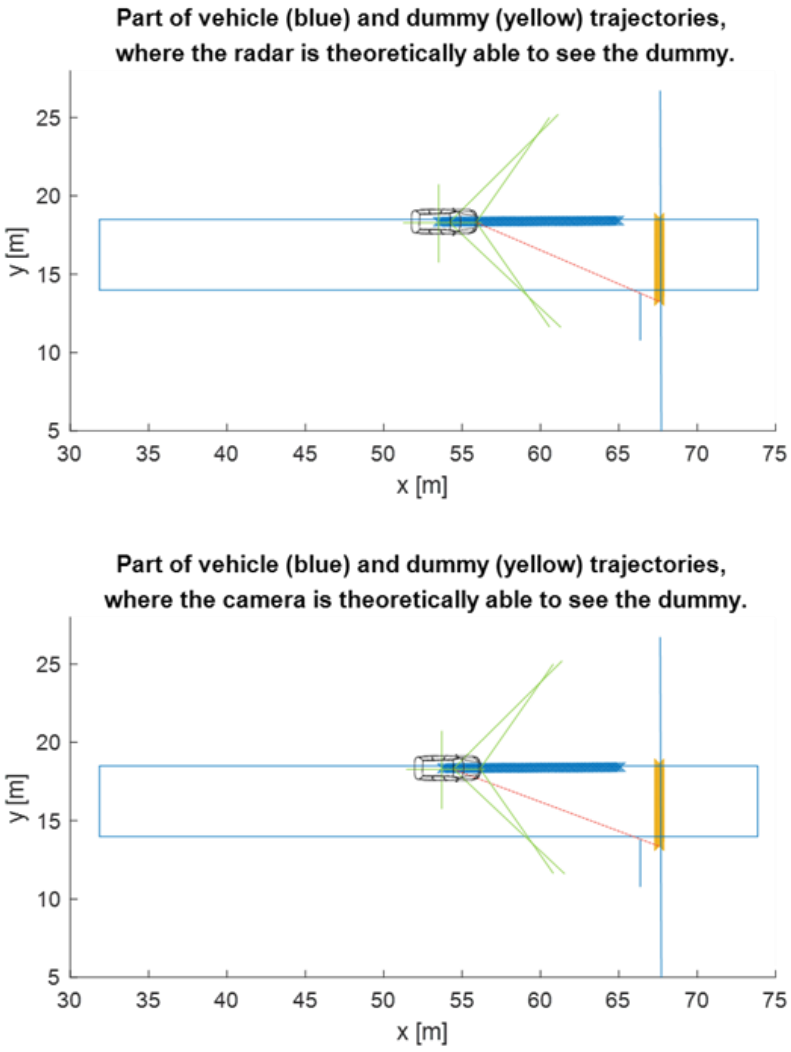

Figure 5: Parts of trajectories of test case ID 1, where the radar (top) and camera (bottom) sensors are theoretically able to the dummy.

For each test case, it is evaluated at which position and timestamp the vehicle detected the object. For the camera sensor an object list is available, which is filtered based on the object with type 4 (pedestrian). For classifying the pedestrian target as detected with the camera sensor, no threshold for the probability that the detected object is a pedestrian was necessary as this value in the data is always 1 for type 4. There is no object list exclusively for the radar sensor available, but an object list based on the fused sensors. In case the radar sensor has detected an object but the camera sensor not, the detection of the radar sensor only can be extracted. For classifying the pedestrian target as detected with the fused

This project has received funding from the European Union's Horizon 2020 research and innovation programme under Grant Agreement 861570.

sensors or the radar sensor only, a threshold of 0.5 is used for the probability that the detected object is a pedestrian.

For the first detections of the pedestrian, the time and TTC values are extracted, which is exemplarily shown for test case ID 1 in Figure 6. The TTC values are calculated with the vehicle velocity in x-direction at the current timestamp and the distance in x-direction to the targeted hitpoint. The velocity is subject to fluctuations in the test runs as the speed was controlled by a human driver. Hence, these fluctuations also influence the TTC calculation.

It can be seen in Figure 6Figure 6 that the fused sensors detected the pedestrian 820 ms after the target was not obstructed anymore for the radar sensor at a calculated TTC of 1.8 s. The camera sensor detected the pedestrian 260 ms after the target was not obstructed anymore for the camera sensor at a calculated TTC of 2.4 s. In general, the camera sensor detected the object faster than the fused sensors due to the time required for the fusion algorithm.

Additionally, the end of the ground-truth dummy position shows that the hitpoint was in this test case as intended near to the middle of the vehicle, which was not always as well aligned in other test runs.

This project has received funding from the European Union's Horizon 2020 research and innovation programme under Grant Agreement 861570.

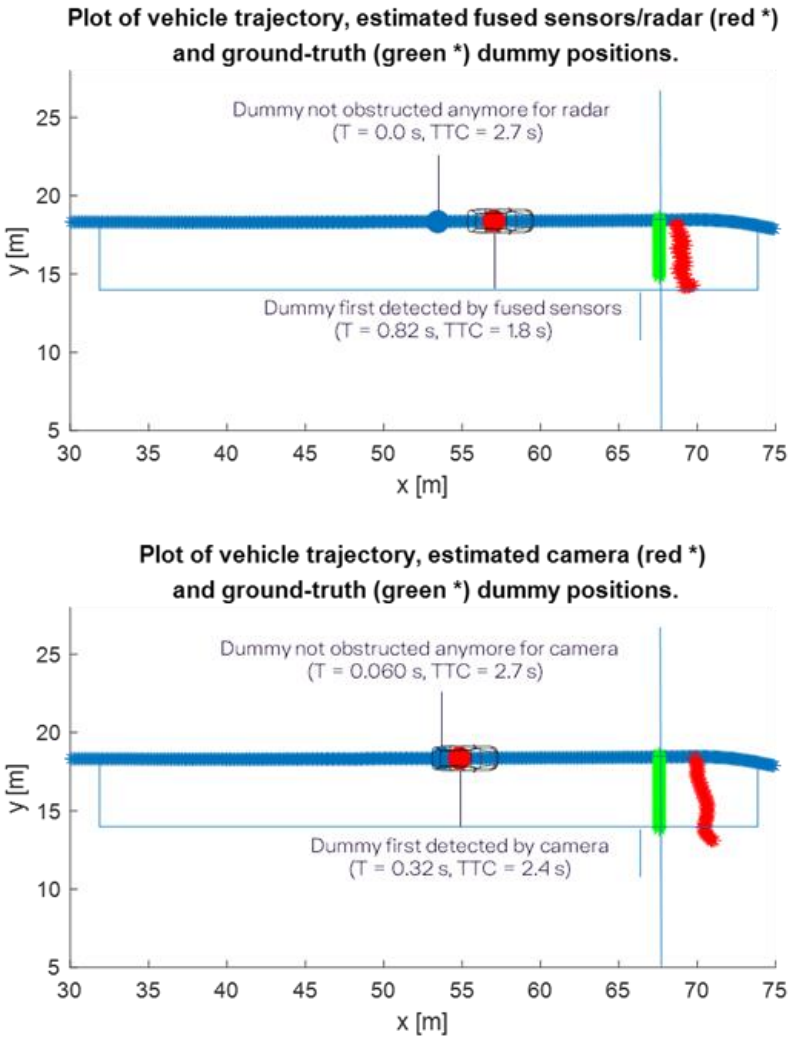

Figure 6: Example visualization (test case ID 1) of estimated dummy positions and ground-truth positions of the fused sensors (top) and the camera sensor (bottom). Additionally, extracted time and TTC values for the not obstruction and first detection positions are given.

This evaluation was conducted with all test cases and is summarized in Table 2, where the TTC values are listed for those positions, at which the target is not obstructed and at which the target is first detected. Additionally, the time passed between those two positions is calculated. The given vehicle velocity in Table 2Table 1 is the extracted velocity from the position, at which the radar sensor can theoretically first see the target. In the following, always this velocity is referenced, which is why sometimes for comparisons between the same desired velocity configuration two velocities are given. The pedestrian velocity given in Table 2 is

This project has received funding from the European Union's Horizon 2020 research and innovation programme under Grant Agreement 861570.

the desired speed programmed into the target system, which is also not constant during the test runs due to readjustments from the light barriers.

Table 2: Summary of the key detection performance results of the third, dynamic measurement campaign (in the cases with * only radar detections are available).

Test case ID	Rain [mm/h]	Vehicle velocity [kph]	Target velocity [kph]	TTC [s]		UTC time offset [s]	
				first not obstructed	first detected testing	not obstructed until detected	
				radar	camera	fused	camera
1	0	15	8	2.75	2.67	1.82	2.38
2	0	35	8	1.97	1.96	1.12	1.57
3	16	16	8	2.55	2.46	1.75	2.30
4	16	32	8	2.39	2.37	0.53*	
5	66	17	8	3.14	3.10		
6	66	33	8	2.25	2.23		
7	98	14	8	3.31	3.26		
8	98	32	8	2.46	2.46		

Only for test case ID 1, 2, and 3 the camera object list as well as the fused object list contains the pedestrian. For test case ID 4, only the radar sensor has detected the pedestrian, and at all other test cases, the pedestrian was neither detected by the camera sensor nor the radar sensor.

The results do not show a degradation of the detection performance due to adverse weather at the settings with 15/16 kph at 0 mm/h and 16 mm/h. At 0 mm/h with 15 kph, the camera sensor detected the pedestrian at a TTC of 2.38 s and at 16 mm/h with 16 kph, the camera sensor detected the pedestrian at a TTC of 2.30 s. At 0 mm/h with 15 kph, the fused sensors detected the pedestrian at a TTC of 1.82 s and at 16 mm/h with 16 kph, the fused sensors detected the pedestrian at a TTC of 1.75 s. Comparing the UTC time difference between the object being not obstructed and being detected, less time passed for the fused sensors as well as the camera sensor at 16 mm/h with 16 kph than at 0 mm/h with 15 kph.

However, the results show a degradation of the detection performance due to adverse weather at the settings with 35/32 kph at 0 mm/h and 16 mm/h. At 0 mm/h with 35 kph, the camera sensor detected the pedestrian at a TTC of 1.57 s and at 16 mm/h with 32 kph, the camera sensor did not detect the pedestrian. At 0 mm/h with 35 kph, the fused sensors detected the pedestrian at a TTC of 1.12 s and at 16 mm/h with 32 kph, only the radar sensor detected the pedestrian at a TTC of 0.53 s. Comparing the UTC time difference between the object being not obstructed and being detected, less time passed for the fused sensors at the setting with 0 mm/h and 35 kph, than for the radar at 16 mm/h with 32 kph. The time passed for the camera sensor cannot be compared, as the camera sensor did not detect the pedestrian at the setting with 16 mm/h and 32 kph.

The results also indicate a degradation in detection performance due to higher vehicle velocities at the settings with 15 kph and 35 kph at 0 mm/h. The TTC values for the

This project has received funding from the European Union's Horizon 2020 research and innovation programme under Grant Agreement 861570.

detections are lower with 35 kph compared to 15 kph, which can mainly be explained by the higher vehicle velocity. However, comparing the UTC time difference between the object being not obstructed and being detected, less time passed for the fused sensors as well as the camera sensor at 0 mm/h with 15 kph, than at 0 mm/h with 35 kph. The time passed between the pedestrian being not obstructed for the radar sensor and being detected by the fused sensors was 820 ms at 0 mm/h with 15 kph, and 920 ms at 0 mm/h with 35 kph. The time passed between the pedestrian being not obstructed for the camera sensor and being detected by the camera sensor was 260 ms at 0 mm/h with 15 kph, and 420 ms at 0 mm/h with 35 kph.

Based on these results, it can be assumed that vehicle velocities higher than 15 kph in combination with rain impede the detection performance and, contrary to the expectations from the static measurements, also the rain rate of 16 mm/h can be challenging for radar and camera sensors in dynamic settings for vehicle velocities higher than 15 kph. Even if a detection was possible here, it was with a high time delay.

As it is also visible from the offset between the estimated (red) and ground-truth (green) dummy position in Figure 6, the estimated dummy positions underlie a systematic error, which stems besides detection errors also from the vehicle speed with which the vehicle drives during the time of sensor data processing. Under the assumption that the fused sensors or the radar sensor can perfectly estimate the position of the target in x-direction, from the mean error in x-direction and the vehicle speed, an estimation of the processing time can be calculated. For test case ID 1, this results in a processing time of 342 ms, for test case ID 2 in a processing time of 251 ms, for test case ID 3 in a processing time of 200 ms, and for test case ID 4 in a processing time of 201 ms (radar sensor only). These values are similar to the results of Demo 3, where a mean processing time of 220 ms was estimated.

3.2.1.3 Results of the simulation

To be able to compare the test results to simulations, all of the test cases from Table 2 are simulated according to the same methodology as described in (Löffler, et al., 2022). Therefore, the scenarios were created in CarMaker and the FoV models for the respective rain rates from (Löffler, et al., 2022) included. Figure 7 shows the CarMaker setup for test case ID 3 and the integrated radar FoV model for 16 mm/h, where also the test hall boundaries, the obstruction wall and the rain area are visualized.

This project has received funding from the European Union's Horizon 2020 research and innovation programme under Grant Agreement 861570.

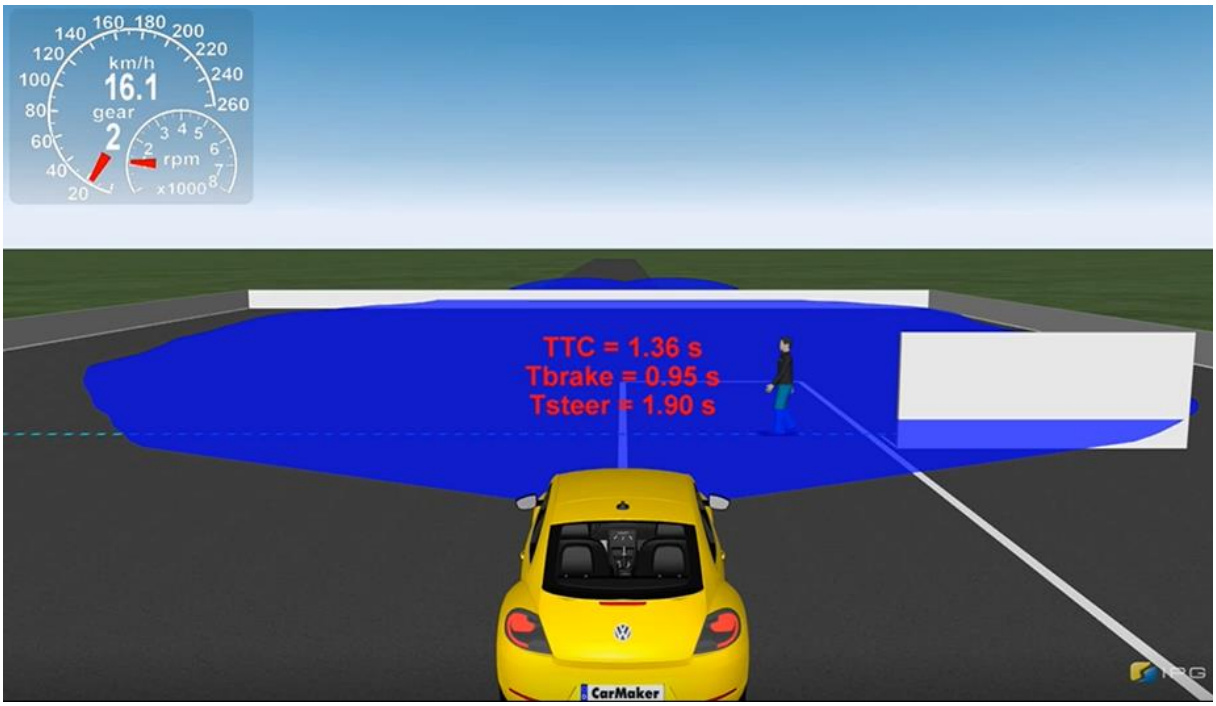

Figure 7: Remodeling of the test hall scenarios in CarMaker.

For each of the test cases, the method described in (Löffler, et al., 2022) is executed and the values for the following parameters extracted

- the estimated time required for braking (t_brake)
- the estimated time required for steering (t_steer)
- the intervention type selected by the system
- the TTCs values where the object was detected with camera and radar sensor
- the TTCs values where the intervention was triggered with camera and radar sensor
- the binary information to the occurrence of a collision
- the remaining collision velocity (v_collision), in case the collision was not prevented

In all eight test cases, the calculated time required for braking (t_brake) is smaller than the calculated time required for steering (t_steer), which is why in each simulated test case the generic AEB function was triggered. In total, 14 simulations were performed, as the test cases with rain amounts between 0 mm/h and 66 mm/h are simulated once with the radar FoV model and once with the camera FoV model and the test cases with rain amounts of 98 mm/h solely once with the radar FoV model, as no model could have been generated for the camera sensor at this rain intensity. At all performed simulations, the TTCs at which the pedestrian is detected with the radar as well as the camera sensor are larger than the

This project has received funding from the European Union's Horizon 2020 research and innovation programme under Grant Agreement 861570.

calculated times required for braking (t_brake), which is why the generic AEB intervention is triggered based on when the TTC is around the t_brake value. At the speed configuration with 32/33 kph and rain intensities of 66 mm/h and 98 mm/h, collisions occurred with the investigated sensors nevertheless, as the reduced friction coefficient was not considered for calculating the time required for braking (t_brake). In all other performed simulations, the accident could have been prevented.

Table 3: Summary of the simulation results of the test cases.

Test case ID	Rain [mm/h]	Friction coeffi-cient	Vehicle velocity [kph]	Target velocity [kph]	t_brake [s]	t_steer [s]	Intervention type	TTC [s]				Collision		v_collision [kph]	
								object detected		intervention					
								radar	camera	radar	camera	radar	camera	radar	camera
1	0	0.9	15	8	0.94	1.9	break	1.89	1.85	0.95	0.95	0	0	0	0
2	0	0.9	35	8	1.26	1.9	break	1.73	1.73	1.26	1.26	0	0	0	0
3	16	0.8	16	8	0.95	1.9	break	1.88	1.84	0.96	0.96	0	0	0	0
4	16	0.8	32	8	1.21	1.9	break	1.75	1.73	1.22	1.22	0	0	0	0
5	66	0.6	17	8	0.96	1.9	break	1.87	1.84	0.98	0.98	0	0	0	0
6	66	0.6	33	8	1.21	1.9	break	1.75	1.73	1.22	1.22	1	1	10.4	10.4
7	98	0.4	14	8	0.92	1.9	break	1.92		0.93		0		0	
8	98	0.4	32	8	1.21	1.9	break	1.74		1.21		1		19.9	

3.2.1.4 Comparison of the results of the third measurement campaign and of the simulations

In the following, the results from the third, dynamic measurement campaign are compared to the results from simulations, in which FoV models derived from the second, static measurement are integrated. Therefore, a special focus is given to the TTCs at which the pedestrian is detected in testing compared to in simulations. The TTC values are considered as similar when the difference between the testing result and the simulation result is smaller than 150 ms. As no object list exclusively for the radar sensor is available for the measurements, the object list based on the fused sensors is compared to the results from simulation with the radar FoV models.

Figure 8 shows the resulting TTCs for the camera sensor. At the rain intensities of 0 mm/h and 16 mm/h and the vehicle velocity of 15/16 kph, the pedestrian was detected with the camera sensor at a TTC of 2.38 s and 2.30 s in testing. In simulations, the pedestrian was detected at a TTCs of 1.85 s and 1.84 s, which is 531 ms and 460 ms later than in the testing. At the rain intensity of 0 mm/h and the vehicle velocity of 35 kph, the pedestrian was detected with the camera sensor at a TTC of 1.57 s in testing. In simulation, the pedestrian was detected at a TTC of 1.73 s, which is 156 ms earlier than in the testing. Against our assumptions from simulation, no detection with the camera sensor in testing was possible at the rain intensities of 16 mm/h and 66 mm/h with the vehicle velocities of 32/33 kph and at the rain intensity of 66 mm/h and 17 kph. In line with our assumptions as no simulations

This project has received funding from the European Union's Horizon 2020 research and innovation programme under Grant Agreement 861570.

were performed for these cases, no detection with the camera sensor in testing was possible at the rain intensity of 98 mm/h and the vehicle velocities of 14 and 32 kph.

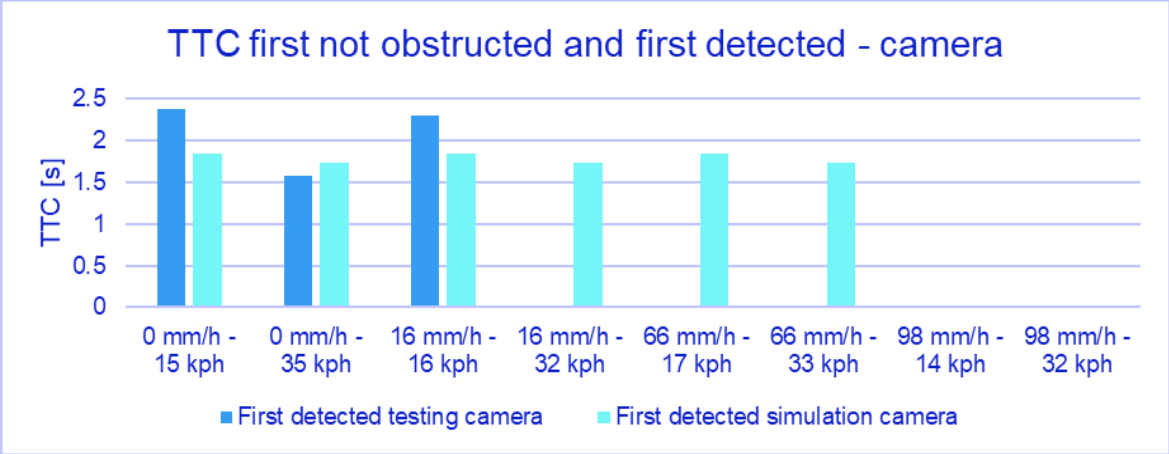

Figure 8: Comparison of TTCs, where the pedestrian was first detected by the camera sensor in testing and by the camera sensor in simulation.

Figure 9 shows the investigated TTCs for the fused sensors and the radar sensor. At the rain intensities of 0 mm/h and 16 mm/h and the vehicle velocity of 15/16 kph, the pedestrian was detected with the fused sensors at a TTC of 1.82 s and 1.75 s in testing. In simulations, the pedestrian was detected at a TTC of 1.89 s and 1.88 s, which is similar (65.9 ms and 129 ms difference). At the rain intensity of 0 mm/h and the vehicle velocity of 35 kph, the pedestrian was detected with the fused sensors at a TTC of 1.12 s in testing. In simulation, the pedestrian was detected at a TTC of 1.73 s, which is 610 ms earlier than in the testing. At the rain intensity of 16 mm/h and the vehicle velocity of 32 kph, the pedestrian could have been detected solely with the radar sensor at a TTC of 0.53 s in testing. In simulation, the pedestrian was detected with the radar sensor at a TTC of 1.78 s, which is 1.22 s earlier than in the testing. Against our assumptions from simulation, no detection with the radar sensor in testing was possible at the rain intensities of 66 mm/h and 98 mm/h with both vehicle velocity configurations.

This project has received funding from the European Union's Horizon 2020 research and innovation programme under Grant Agreement 861570.

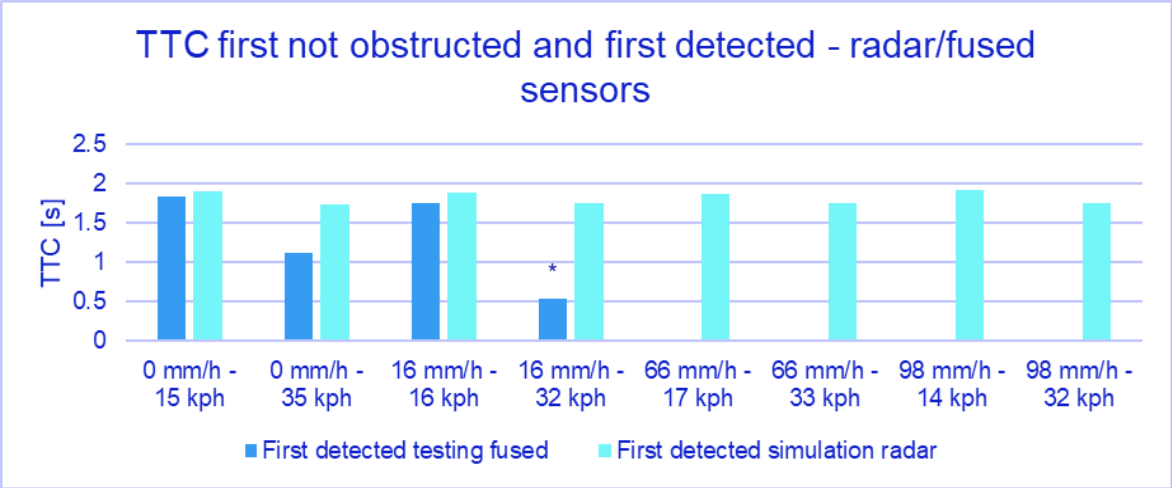

Figure 9: Comparison of TTCs, where the pedestrian was first detected by the fused sensors in testing and by the radar sensor in simulation (in the case with * only radar sensor detections are available).

3.2.1.5 Conclusion of the comparison

Table 4 summarizes the compared TTC values from the third, dynamic measurements to the simulation results, where the FoV models derived from the second, static measurement are integrated. In addition, the TTCs at which the intervention was initiated in simulations is included, which shows that at 0 mm/h and 16 mm/h with the vehicle velocity of 35/32 kph, the detection of the pedestrian with the fused sensors or the radar sensor in testing would have been later than when the generic AEB function has been triggered in simulations.

In conclusion, the detection performance in the dynamic measurement was considerably lower than to be expected from the results of the simulations, where the results of the static measurement are integrated, especially as no detection with any sensor at any time was possible at the rain intensity of 66 mm/h and 98 mm/h. Due to no detection degradation between the rain intensities 0 mm/h and 16 mm/h at the vehicle velocity configuration of 15/16 kph, but an obvious detection degradation between the rain intensities 0 mm/h and 16 mm/h at the vehicle velocity configuration of 35/32 kph, it is assumed that the influence of the rain rate on sensors should not be evaluated independently of the vehicle velocity.

Therefore, it must be assumed that the sensor models derived from static measurements in (Löffler, et al., 2022) might lack the capability of being also applicable to dynamic scenarios and that the perception performance at vehicle velocities above 15 kph as well as at rain intensities above 16 mm/h is probably overestimated in the simulations in (Löffler, et al., 2022). However, these effects can also originate to some extend from other limitations, which are summarized in the following chapter and should be addressed in future work to develop reliable sensor models.

This project has received funding from the European Union's Horizon 2020 research and innovation programme under Grant Agreement 861570.

Table 4: Comparison of the results of the third, dynamic measurement campaign to simulations, where FoV models derived from the second, static measurement are integrated (in the cases with * only radar sensor detections are available or only simulations with radar FoV models are performed).

Test case ID	Rain [mm/h]	Vehicle velocity [kph]	Target velocity [kph]	TTC [s]						
				first not obstructed		first detected testing		first detected simulation		intervention simulation
				radar	camera	fused	camera	radar	camera	
1	0	15	8	2.75	2.67	1.82	2.38	1.89	1.85	0.95
2	0	35	8	1.97	1.96	1.12	1.57	1.73	1.73	1.26
3	16	16	8	2.55	2.46	1.75	2.30	1.88	1.84	0.96
4	16	32	8	2.39	2.37	0.53*		1.75	1.73	1.22
5	66	17	8	3.14	3.10			1.87	1.84	0.98
6	66	33	8	2.25	2.23			1.75	1.73	1.22
7	98	14	8	3.31	3.26			1.92		0.93*
8	98	32	8	2.46	2.46			1.74		1.21*

3.2.1.6 Limitation of the comparison and future work

One limitation of the comparison is that with a moving vehicle, also the reflections within the test hall can increase, which could also influence the reliability of the performed tests. Therefore, a comparison between in-hall test and outside tests would be required to be able to assess this effect and evaluate if the higher deviation at higher speeds can also stem from these effects.

Another constraint is that due to the high test effort, only a limited number of tests was performed. Each test specification was conducted only once. Variations would also be expected between different runs of one test case. Therefore, performing tests with same specifications several times would increase the confidence in the results. Additionally, further variations of test specifications would be needed. The results indicate that the velocity of the vehicle has an influence on the detection performance, but no data is available for other speeds than 15 kph and 35 kph and also the velocity of the pedestrian can have an influence on the detection performance.

Another limitation is that the level, at which the sensor data was used to determine the detection performance, differs between the second and third measurement campaign. For evaluating the third measurement campaign the final object lists were used, which were not available for the radar or the fused sensors in the second measurement campaign. Hence, several assumptions were made for evaluating the radar locations of the second measurement campaign, which differ from the algorithmic implementation of the third measurement.

As the detection performance is dependent on the hardware and software, there is no possibility to generalize the results. It is likely that changes in hardware or software directly influence the performance and tests would need to be revaluated with every change.

This project has received funding from the European Union's Horizon 2020 research and innovation programme under Grant Agreement 861570.

3.2.2 Weather Filter

3.2.2.1 Analysis of the first measurement campaign

Similar to Section 3.2.1.1, we first analyse the measurement data with respect to the variances. The measurements are detailed in D3.2. Recall, that we placed a static dummy at eight different positions, see Figure 10.

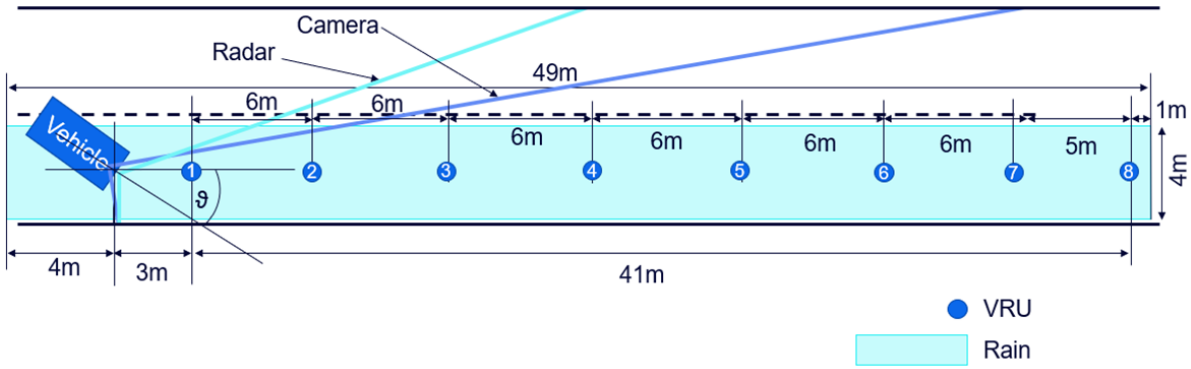

Figure 10: Test setup, static measurements.

To obtain the variances, we positioned a box of 4 meters depth (x-direction), one meter width (y-direction) and two meters high (z-direction) around each dummy position and computed the variances in all directions for each point within the box. Since the measurements are between 8-10 seconds long, we used the average over all obtained frames (framerate of 100ms). The tested weather settings are: reference (no rain or fog), rain low (16mm/h rain), rain high (98mm/h rain), fog 20m (20m visual range), for max (fog with <10m visual range). The variances for the radar in all directions are displayed in Figure 11 - Figure 13.

This project has received funding from the European Union's Horizon 2020 research and innovation programme under Grant Agreement 861570.

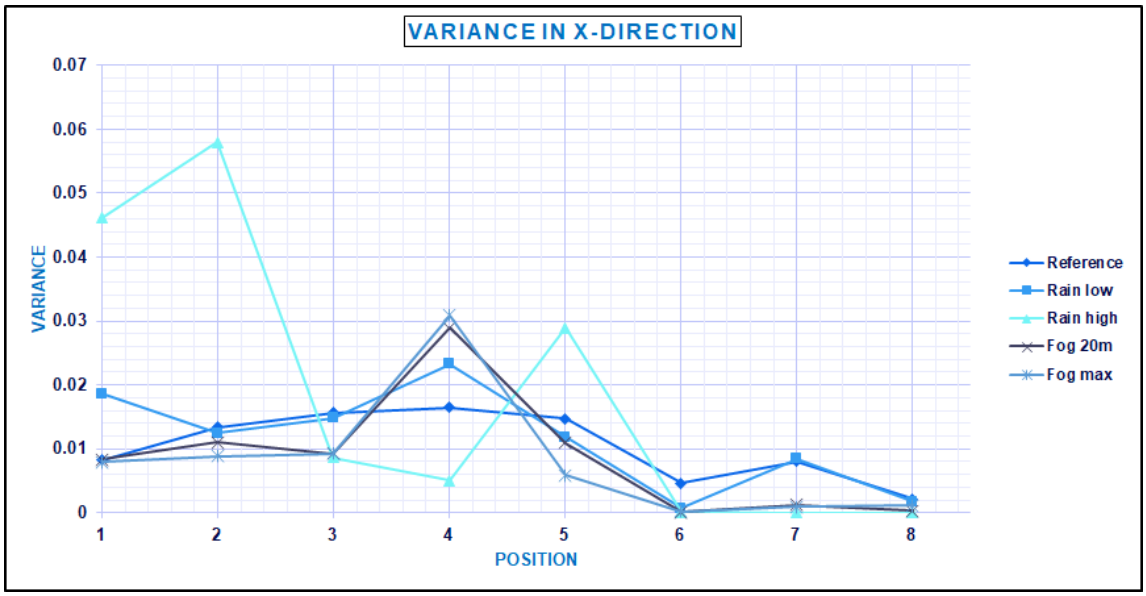

Figure 11: Variances in the longitudinal (x) direction.

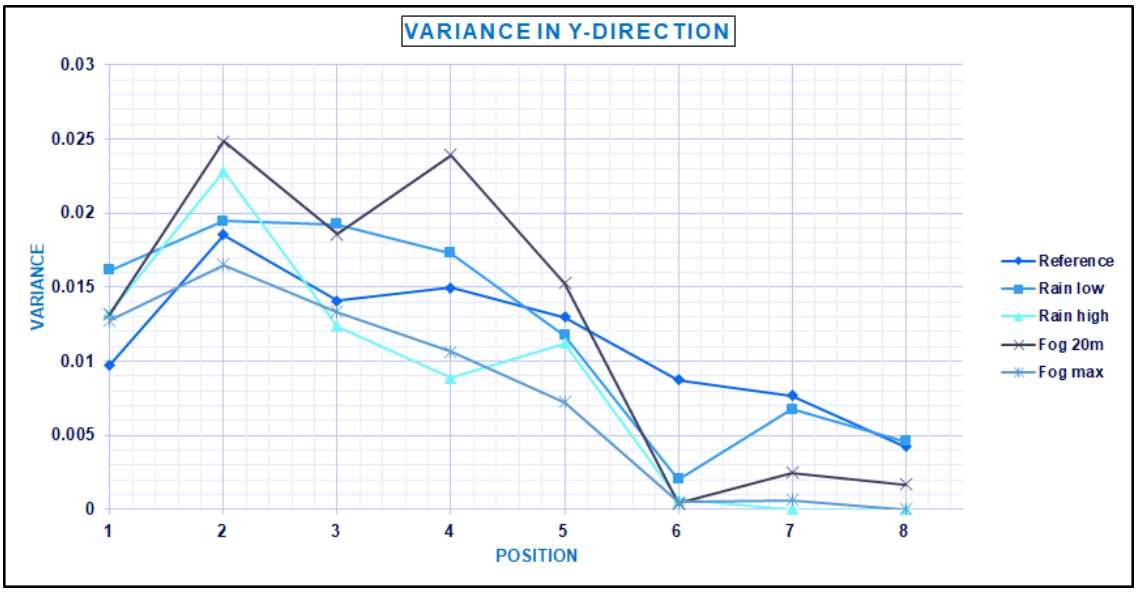

Figure 12: Variances in the lateral (y) direction.

This project has received funding from the European Union's Horizon 2020 research and innovation programme under Grant Agreement 861570.

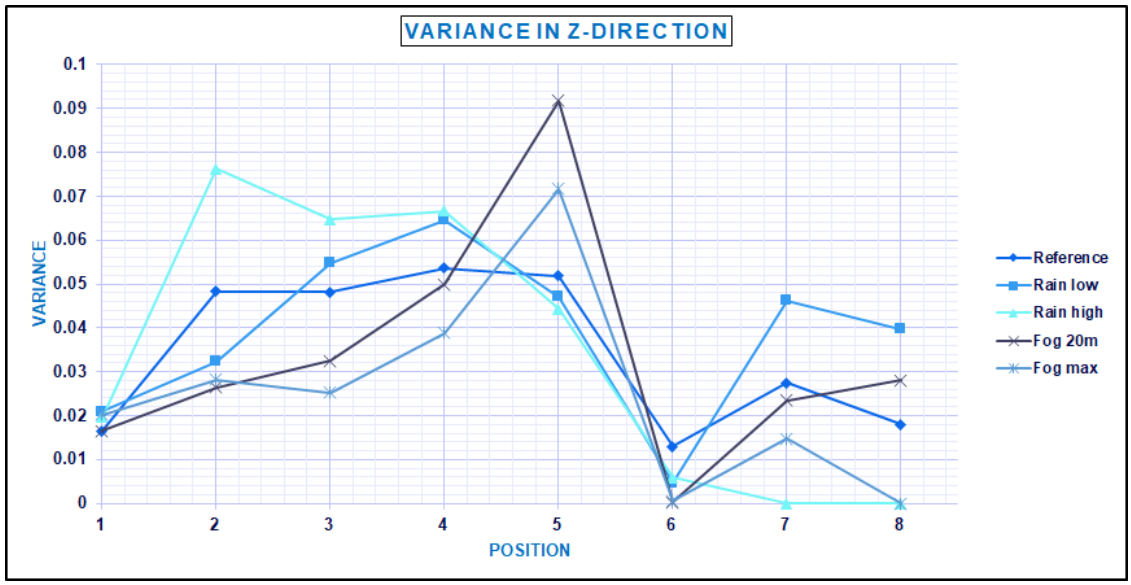

Figure 13: Variances in the z- direction.

In Figure 11 - Figure 13 one can see that the variances are decreasing with increasing distance to the dummy. However, a difference between the various weather settings cannot be concluded.

3.2.2.2 Development of the weather filter

Based on the first measurement campaign and the advanced sensor technology used here, the weather filter was defined and continuously developed, and adapted. In the following, two weather filter models are compared, which are calibrated on the one hand on the data of measurement campaign one and on the other hand on measurement campaign two. The second measurement campaign represents state-of-the-art sensor technology. Due to the complexity of the weather influences on sensors, a hybrid approach is chosen, which is based on empirical or physical models depending on the data availability.

The following Figure 14 and Figure 15 show the comparison of the state-of-the-art radar sensors with the prototype radar sensors (dashed line).

This project has received funding from the European Union's Horizon 2020 research and innovation programme under Grant Agreement 861570.

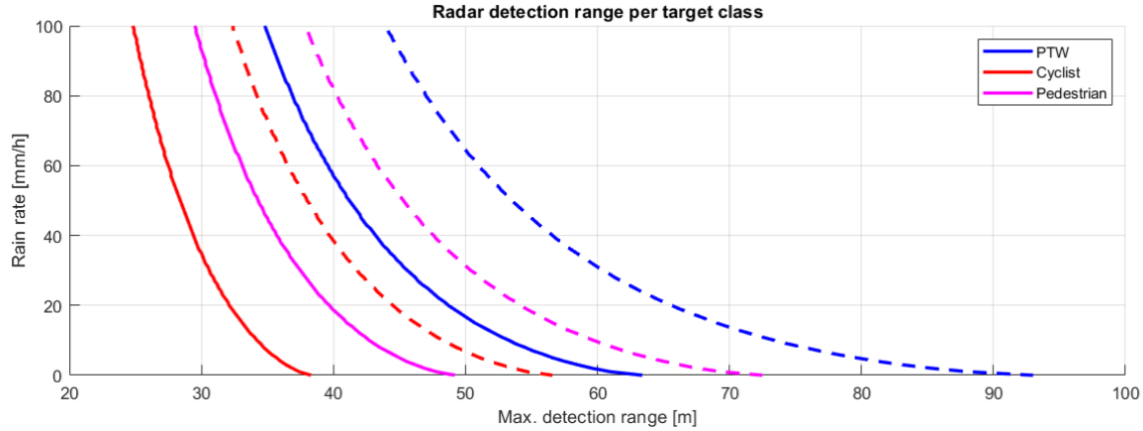

Figure 14: Radar detection range under rain.

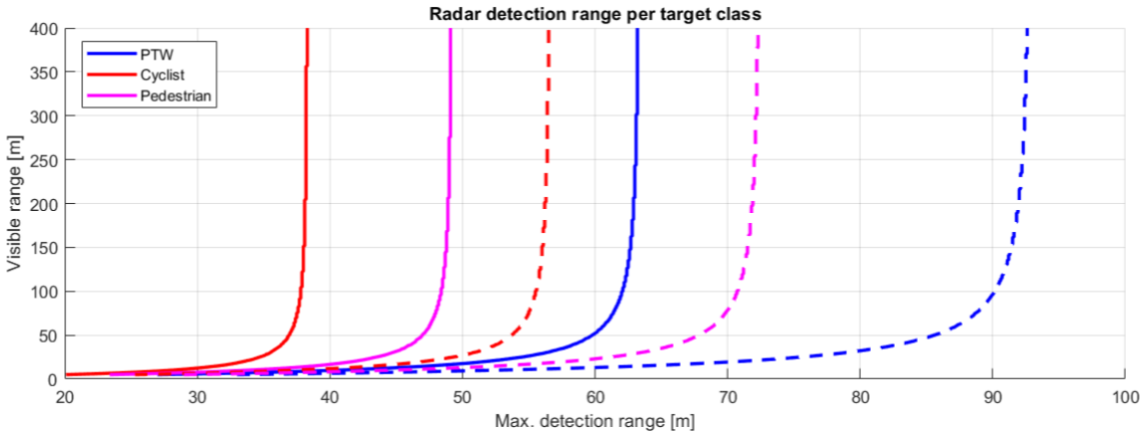

Figure 15: Radar detection range under fog.

In Figure 16, the comparison of both camera systems is plotted with significant improvements in the maximum range. The observation under fog was excluded here, since the visual range of sight assumption applies equally to both systems.

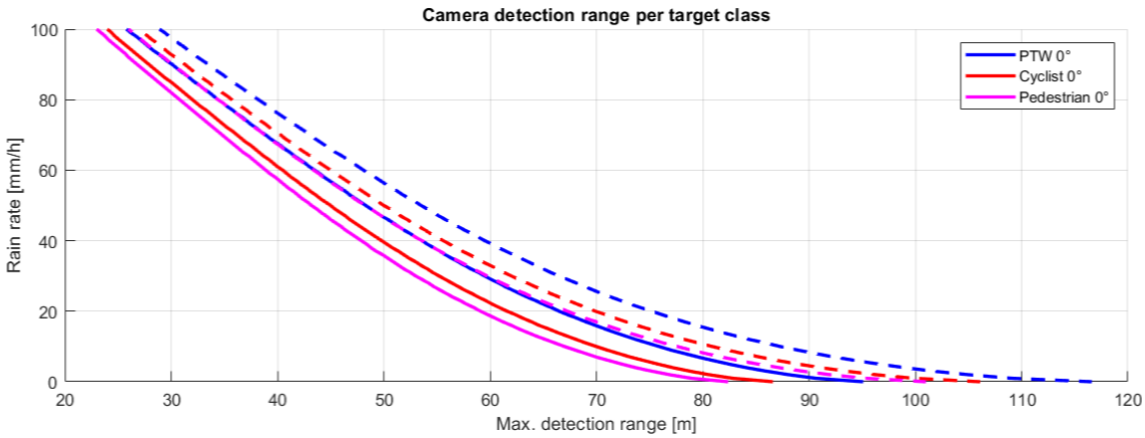

Figure 16: Camera detection range under rain.

This project has received funding from the European Union's Horizon 2020 research and innovation programme under Grant Agreement 861570.

The lidar sensor is not compared here, since no information is available on a state-of-the-art lidar sensor. For the sake of completeness, only the data of the prototype sensor are listed below in Figure 17and Figure 18.

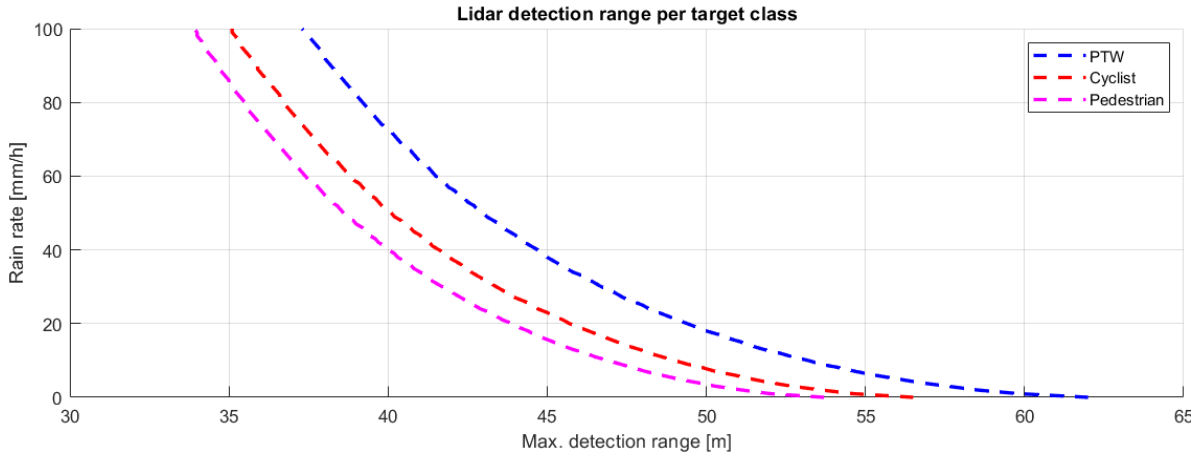

Figure 17: Lidar detection range under rain.

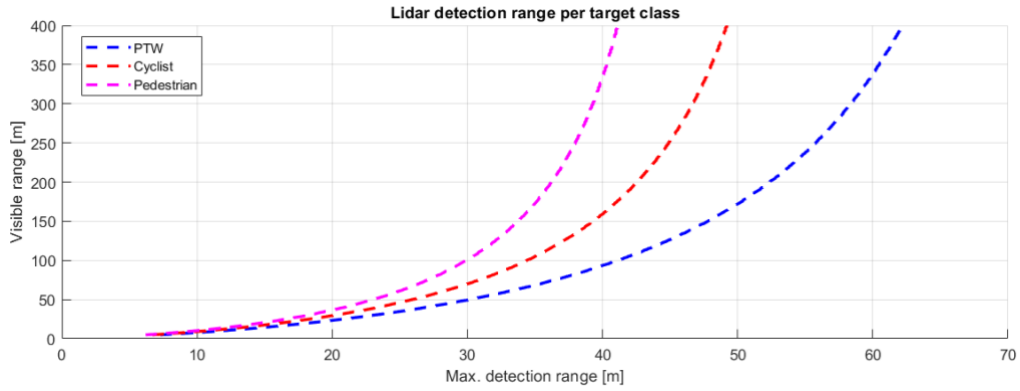

Figure 18: Lidar detection under fog.

3.2.2.3 Results and conclusion of the weather filter

As the weather filter has been developed based on the first measurement campaign, we compared it with data from the second measurement campaign. The second campaign, however, has been carried out with advanced hardware representing future sensor technologies. For the radar, it can be seen in Figure 14 and Figure 15 that a substantial performance improvement with better hardware is to be expected. For the camera, however, small improvements can be expected; see Figure 16. The next steps for the development process of the weather filter are further measurement campaigns to check the validity of the weather filter's results.

This project has received funding from the European Union's Horizon 2020 research and innovation programme under Grant Agreement 861570.

Additionally, modelling secondary weather effects, such as rain droplets on the sensors, must be integrated. The conclusion is in many points similar to the FoV model (see Section 3.2.1.5), in that more testing is required, and the needed effort exceeds all previous efforts by magnitudes, while the results remain hardware and software dependent. Therefore, it remains a challenge for the future to have a generalized and validated model accurately representing weather effects on perception hardware and software in simulation.

This project has received funding from the European Union's Horizon 2020 research and innovation programme under Grant Agreement 861570.

4. Demo 3

4.1 High-Level Description

The objective of the demo 3 is to develop a vehicle capable of avoiding collisions with VRU's in selected scenarios (see (Löffler, et al., 2021) and (Löffler, et al., 2022)). The vehicle utilizes autonomous driving technologies and can perform automated emergency braking (AEB) and automated emergency steering (AES) manoeuvres. The software architecture of the vehicle's functionality is modular, such that each project partner can develop their own software module and each module can communicate in real time with other modules. The architecture is displayed in Figure 19. Since the verification with an emphasize of reduction in killed and severely wounded VRUs is performed in WP5, this report will focus on quantifying the performance of each of the individual modules.

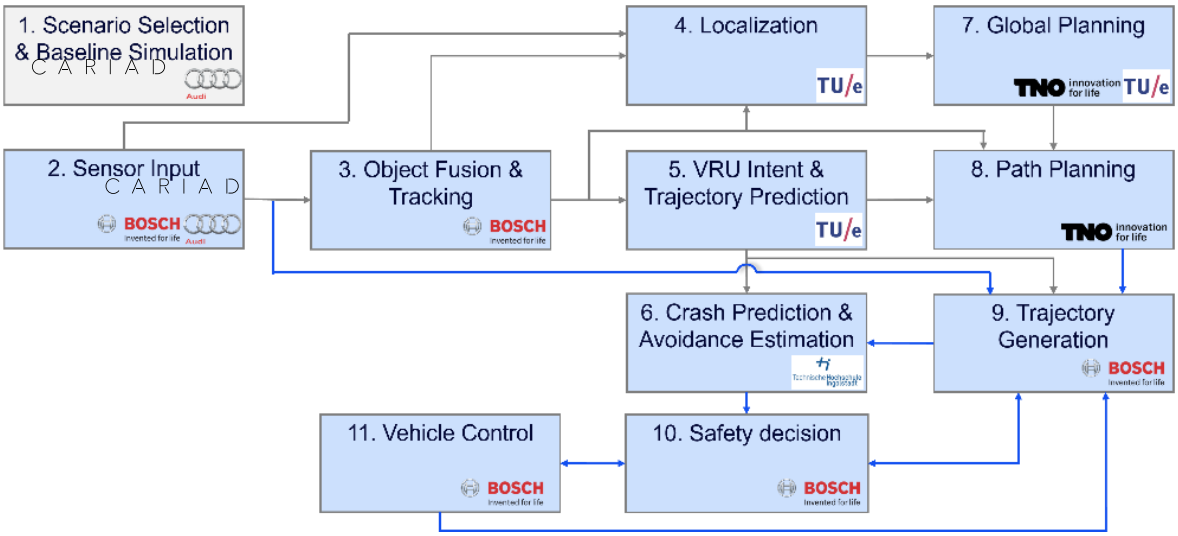

Figure 19: Demo 3 vehicle architecture.

4.2 Quantification

This section quantifies the performance of each of the individual system modules within the architecture individually. Here, the capabilities of each module are emphasized, because there are no defined KPIs for each algorithm of the demonstrator. Indeed, the nature of the demonstrator is it to quantify the prospects of a potential technology, rather than present a fully developed product for series production.

This project has received funding from the European Union's Horizon 2020 research and innovation programme under Grant Agreement 861570.

4.2.1 Path planning

The vehicle path planning is performed by a Model Predictive Control (MPC) algorithm, which is described in deliverable D3.6 and (Ploeg, Smit, Teerhuis, & Silvas, 2022). Although the path planning system is capable of following different difficult road structures and doing nominal VRU evasive manoeuvring, the aim of the path planner in the scope of the Demo 3 verification is to bring the vehicle in a repeatable initial condition at the time of triggering AEB/AES. This means following the lane center, regardless of test starting position. Note that we assume that the lane input reference, obtained from measurement data, is perfect in this quantification analysis.

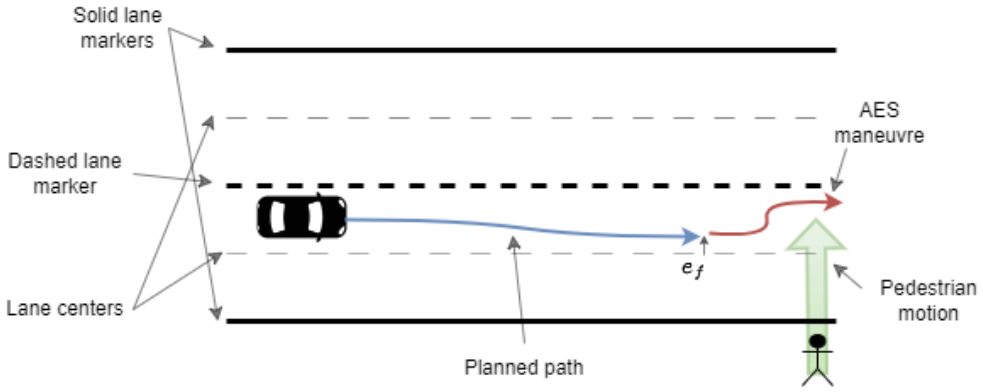

Figure 20 Vehicle path planning prior to AES manoeuvre

In order to quantify the performance of the path planner, the following KPI's are defined:

1. Lateral and heading deviation from the lane center at the end point of the calculated paths: The path should be long enough the steer the vehicle back to the lane center. In the final path position, the vehicle should be aligned both in lateral position and heading with the observed lane center. The lateral error in indicated by e_f in Figure 20. The heading error at the end of the planned path with respect to the lane center will henceforth be referred to as e_θ.
2. During testing, we have identified that the sufficient update rate f_d is 1 Hz. The second KPI is the difference between the desired and achieved replanning frequency. If the desired update rate is not achieved, the resulting path can be outdated with respect to the current situation and system performance and repeatability cannot be guaranteed.
3. The trajectory controller designed by Bosch demands a kinematic feasible path. This is achieved by the constraint that the MPC controller should be compliant with the prescribed kinematic vehicle model. Although it is not possible to prove this, based on the recorded path data, visual inspection can confirm the compliance of the system to this KPI. Note, however, that kinematic compliance

This project has received funding from the European Union's Horizon 2020 research and innovation programme under Grant Agreement 861570.

is incorporated in the optimization program and deviation thereof would result in infeasibility of the optimization program.

4.2.1.1 Lateral deviation

As the lane output (left and right line and estimated lane center) of the perception system is given by a (x,y)-pointcloud, the lateral deviation from the lane center at the end point of the calculated path will be computed by comparing the final path point to the closest lane center point. To mitigate the effect of the linear spacing between consecutive road points and prevent additional errors by polynomial fitting, the lane centers are interpolated with a very high resolution (approx. 1 cm) using linear interpolation. Figure 21 shows all computed paths (red) together with all line observations (blue), for one of the tests. Here, it is shown that the test is carried out in the middle of three lanes. Furthermore, the line observations in the global frame are not always very accurate, due to amongst others observation delays, resulting in jittering line plots. However, for this analysis, the lane center estimations from the perception system are considered ground truth.

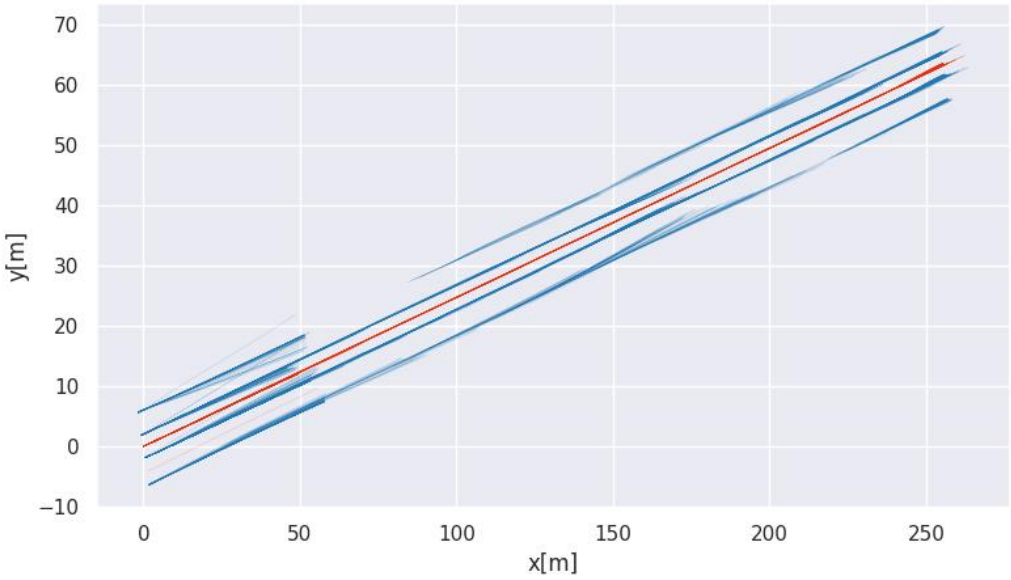

Figure 21 Calculated paths (red) and line observations (blue)

For the first test carried out, the lateral distance to the closest lane center at the end of the calculated path is depicted in Figure 22. Here it is shown that there are two outliers, approximately at N = 95. The calculated path and observed lane markers for one of the outliers is shown in Figure 23. In this figure, it is shown that the right lane marker of the host lane is not observed at this timestep. This leads to a temporary absence of the correct lane center, and consequently to an increased lateral error of approximately a full lane width (+- 4 meters).

This project has received funding from the European Union's Horizon 2020 research and innovation programme under Grant Agreement 861570.

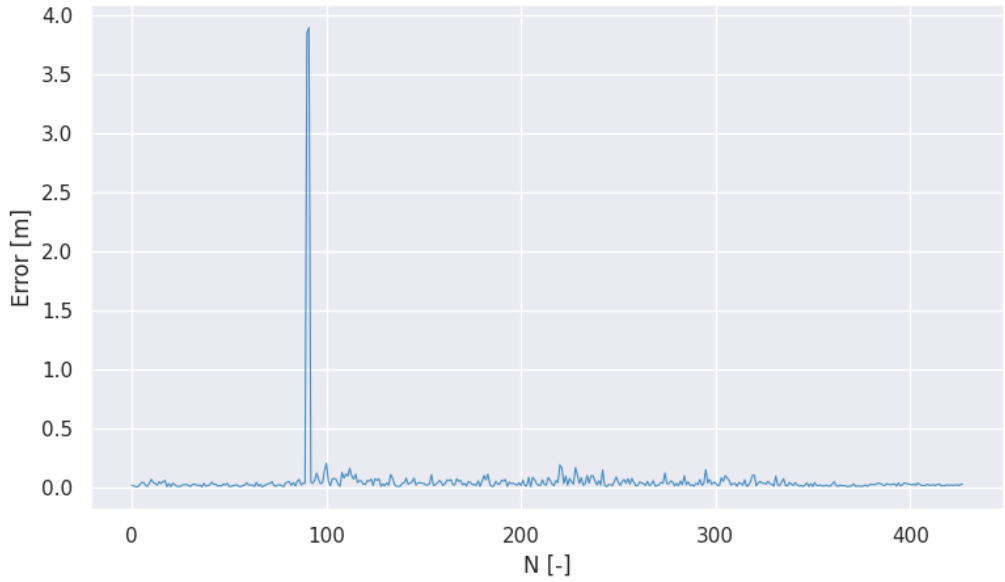

Figure 22 Lateral distance w.r.t. closest lane center

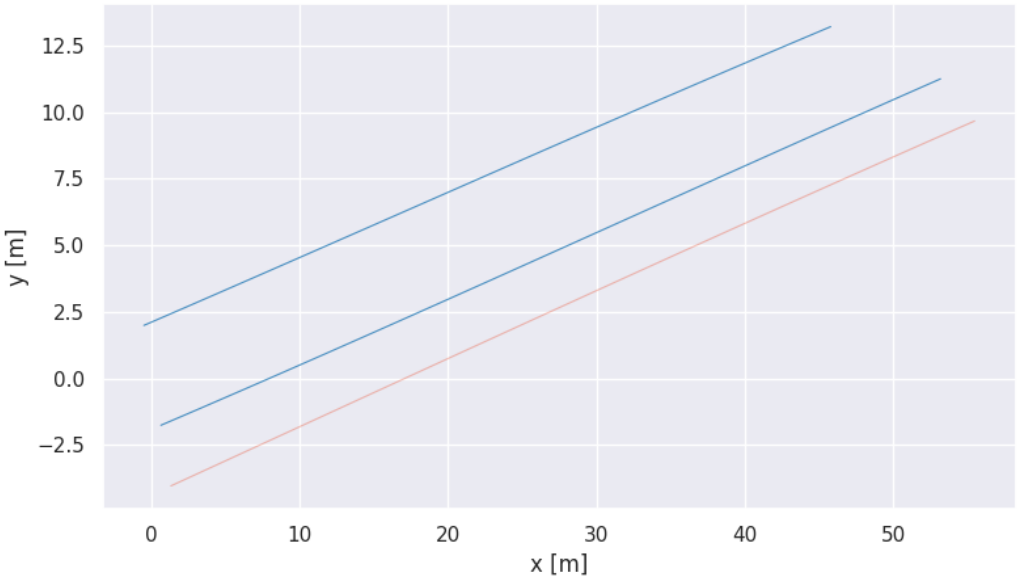

Figure 23 Calculated path (red) and observed lane markers (blue) at error outlier

Ignoring the error outliers caused by the failing perception system, the lateral distance error is shown in Figure 24. Here it is shown that the maximum error is approximately 0.2m. The average error is 0.033m.

This project has received funding from the European Union's Horizon 2020 research and innovation programme under Grant Agreement 861570.

To verify the repeatability of the results, the lateral error is calculated over 10 successful runs of the scenario. The results are depicted in Table 5.

Table 5 Lateral error to lane center over 10 runs

Run #	Lateral error [m]
1	0.033
2	0.100
3	0.081
4	0.137
5	0.296
6	0.129
7	0.072
8	0.035
9	0.165
10	0.102
Mean	0.115

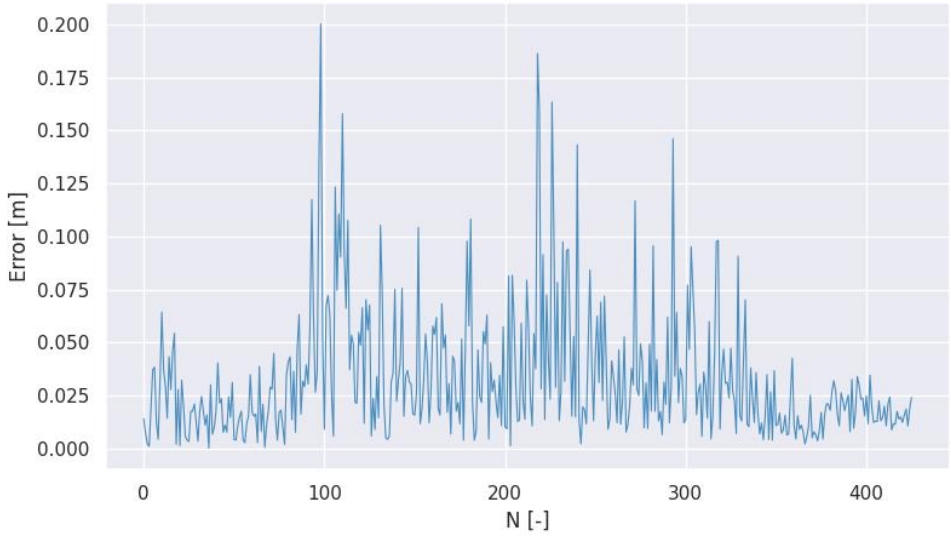

Figure 24 Lateral distance to closest lane center with outlier removed

4.2.1.2 Update rate

As mentioned in the requirement definition, the required update rate for the planner is 1Hz. Note that this is not the maximum update rate of the software, as the planner has been

This project has received funding from the European Union's Horizon 2020 research and innovation programme under Grant Agreement 861570.

running on 10-15Hz as well on the same embedded hardware. However, to save computational load, without hindering the overall performance of the system, the update rate is limited to 1Hz. The achieved mean frequency for 10 runs is shown in Table 6, together with the overall mean frequency over these runs.

Table 6 Update frequency over 10 runs

Run #	Frequency [Hz]
1	0.9998541091168452
2	1.0000763868544298
3	1.0000286110480607
4	1.000169564225108
5	0.9981629088937747
6	1.0004128729541502
7	1.0002272088870336
8	1.0002660560057177
9	1.0002026968699311
10	1.0001671260827019
Mean	0.9999567540937754

4.2.1.3 Kinematic feasibility

Visual assessment is carried out to confirm the kinematic feasibility of the computed paths. Amongst others, this means that there cannot be any discrete jumps in the (x,y)-position states in time. shows four samples of trajectories computed in a single scenario, respectively after 1.0, 10.1, 20.1 and 30.1 seconds. Here, it is shown that both the x- and y-positions don't contain any unexpected discrete jumps or discontinuities.

This project has received funding from the European Union's Horizon 2020 research and innovation programme under Grant Agreement 861570.

Table 7 X-Position, Y-position and trajectory plot at four time instances

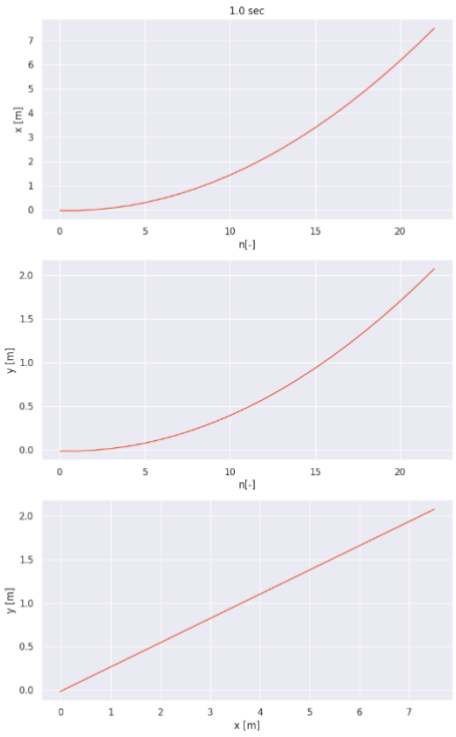	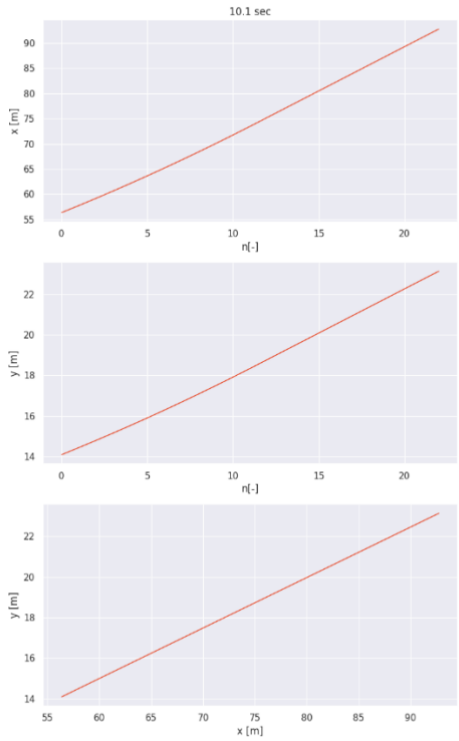

This project has received funding from the European Union's Horizon 2020 research and innovation programme under Grant Agreement 861570.

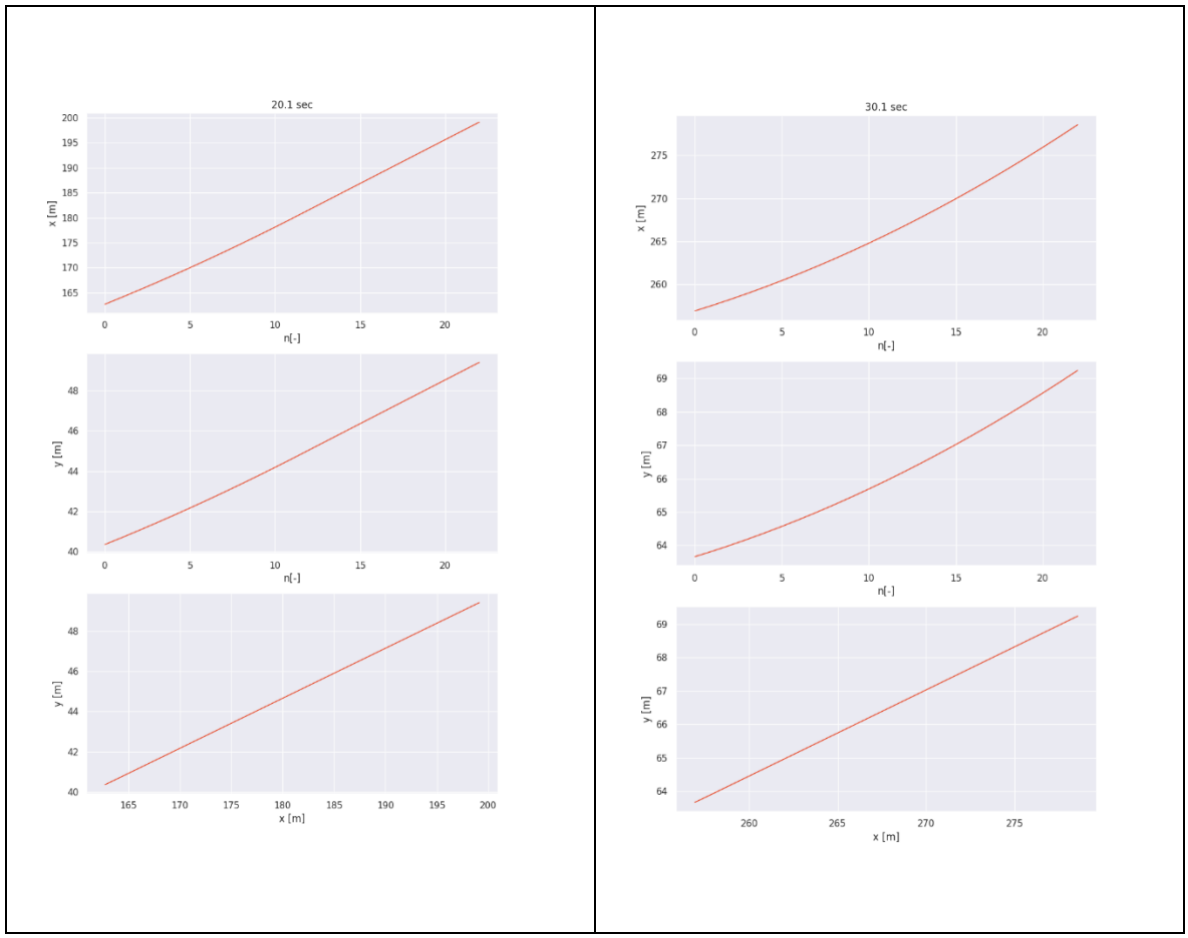

4.2.2 Object Fusion and Tracking

Ensuring safety requires a highly precise object fusion and tracking subsystem. This is because the output of this subsystem serves as input to several subsequent submodules, which may trigger unexpected behavior if object tracking is not accurate enough, such as initiating an emergency maneuver unnecessarily.

To determine the accuracy of the object fusion and tracking module, the measured positions and velocities of the dummy system are compared to the ground truth at each time step. Ground truth data is provided by a differential-GNSS based localization system employed to the VuT and the dummy system (OxTS RT-Range-S (OXTS, 2023)) with specified position and velocity accuracies of 0.03 m (RMS) and 0.02 m/s (RMS) respectively. The accuracy of tracking is affected when an emergency maneuver is carried out. As a result, we analyzed the accuracy by setting a reference time t_I as zero, which is the time when the emergency maneuver is initiated. Measurements taken before this intervention are represented by negative time values, while measurements taken after the intervention are represented by positive time values. For each feature, the mean average error (MAE), standard deviation (std.), maximum (max.) and minimum (min.) errors are reported.

This project has received funding from the European Union's Horizon 2020 research and innovation programme under Grant Agreement 861570.

Figure 25 and Figure 26 depict the results of the analysis before and after t_I, respectively, while tables Table 8 and Table 9 provide specific values for certain timesteps. As illustrated in Figure 25 and Table 9, the average error in tracked positions is roughly 1m longitudinally and 0.1m laterally before triggering an intervention. Nevertheless, there are instances in which maximum errors are significantly higher, reaching up to 3m longitudinally and more than 0.5m laterally. Similarly, the average velocity errors are about 0.1m/s longitudinally and 0.3m/s laterally.

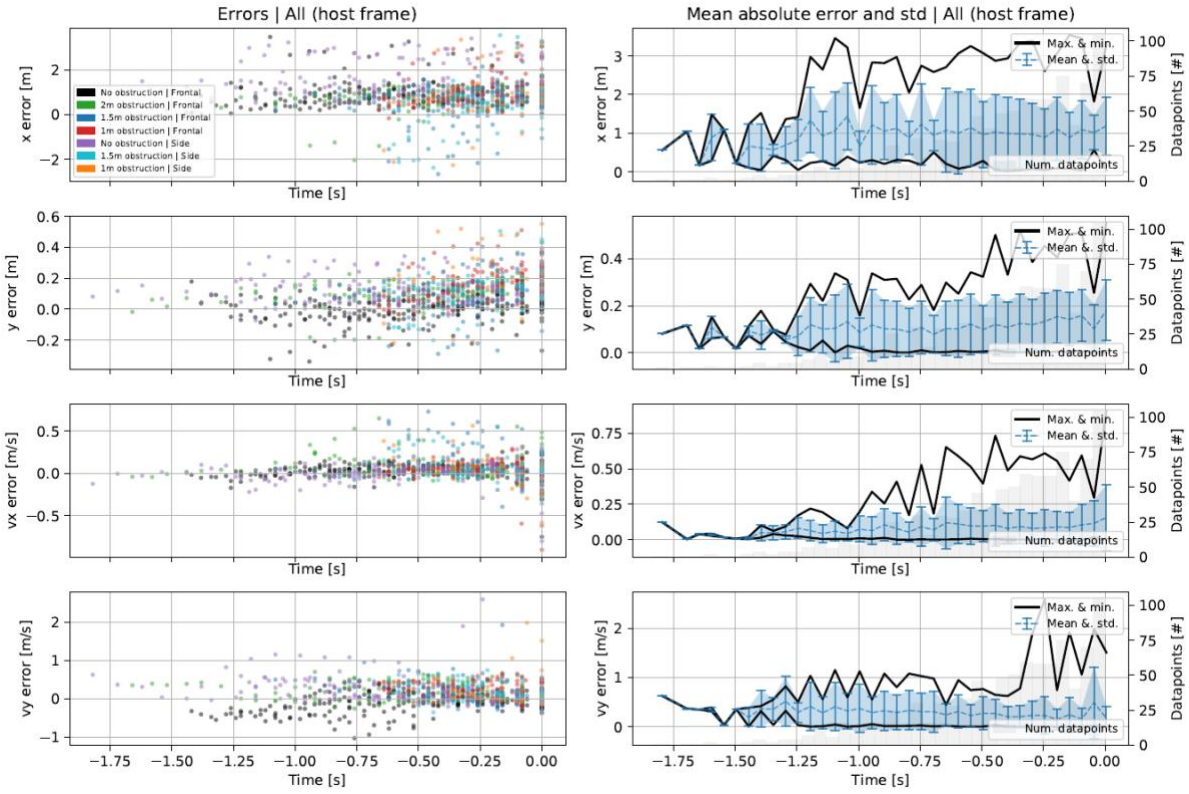

Figure 25: Tracking accuracy before an emergency maneuver is triggered. All errors are shown on the left, and their mean absolute error, standard deviation, minimum and maximum errors on the right.

This project has received funding from the European Union's Horizon 2020 research and innovation programme under Grant Agreement 861570.

Table 8: Tracking MAE, std, max. and min. errors before an emergency maneuver is triggered for some timesteps.

Time [s]		-1.25	-1.0	-0.75	-0.5	-0.25	0.0
x [m]	MAE	0.83	0.66	1.23	0.96	0.89	1.19
	std.	0.53	0.4	1.06	0.86	0.73	0.75
	Min.	0.05	0.24	0.18	0.28	0.05	0.04
	Max.	1.42	1.65	2.75	3.08	2.61	3.28
y [m]	MAE	0.07	0.09	0.11	0.1	0.13	0.18
	std.	0.08	0.06	0.11	0.1	0.12	0.13
	Min.	0.02	0.02	0.01	0.0	0.0	0.0
	Max.	0.18	0.16	0.29	0.32	0.46	0.55
vx [m/s]	MAE	0.08	0.07	0.09	0.1	0.08	0.16
	std.	0.07	0.09	0.14	0.11	0.13	0.23
	Min.	0.03	0.01	0.0	0.0	0.01	0.0
	Max.	0.17	0.2	0.53	0.4	0.61	0.91
vy [m/s]	MAE	0.29	0.37	0.31	0.27	0.23	0.17
	std.	0.2	0.49	0.37	0.33	0.39	0.24
	Min.	0.03	0.01	0.03	0.0	0.01	0.0
	Max.	0.5	1.13	1.03	0.77	2.59	1.51

Upon analysing the tracking errors after triggering an emergency intervention, we observe a significant increase for approximately 1.5 seconds during the maneuver, particularly affecting lateral positions and velocities, after which they return to previous values. During this period, average lateral position errors can reach 0.5m, while average lateral velocity errors can go up to 1m/s. Three samples contain extreme positional errors of up to 8 meters, which are considered outliers and non-critical since they only occur after intervention, but are deliberately included to report on this limitation.

This project has received funding from the European Union's Horizon 2020 research and innovation programme under Grant Agreement 861570.

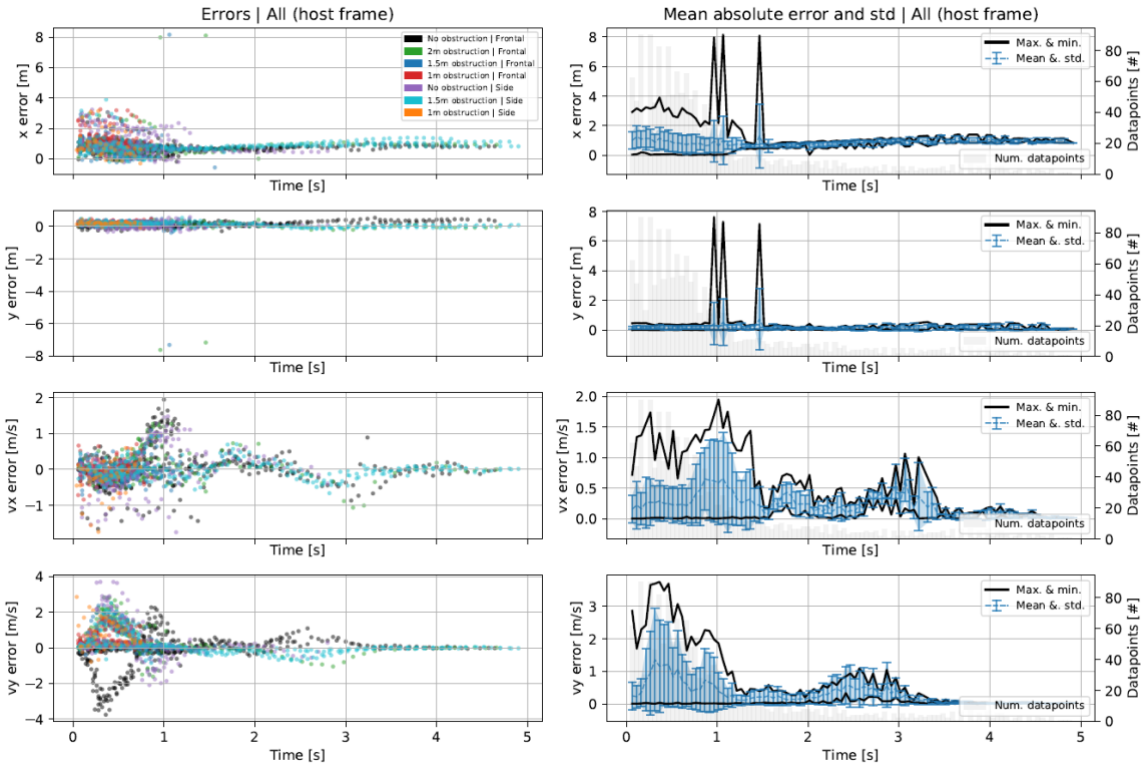

Figure 26: Tracking accuracy after an emergency maneuver is triggered. All errors are shown on the left, and their mean absolute error, standard deviation, minimum and maximum errors on the right.

This project has received funding from the European Union's Horizon 2020 research and innovation programme under Grant Agreement 861570.

Table 9: Tracking MAE, std, max. and min. errors after an emergency maneuver is triggered for some timesteps.

Time [s]		0.05	0.35	0.65	0.95	1.25	1.55	1.85
x [m]	MAE	1.0	1.15	0.71	0.95	0.7	0.61	0.67
	std.	0.59	0.72	0.64	1.39	0.29	0.42	0.14
	Min.	0.03	0.04	0.04	0.01	0.47	0.49	0.46
	Max.	2.92	3.9	2.89	7.98	1.7	0.67	0.86
y [m]	MAE	0.17	0.18	0.16	0.43	0.25	0.12	0.1
	std.	0.09	0.14	0.11	1.43	0.2	0.08	0.06
	Min.	0.0	0.0	0.01	0.01	0.08	0.0	0.04
	Max.	0.45	0.41	0.35	7.63	0.59	0.26	0.17
vx [m/s]	MAE	0.16	0.29	0.21	0.62	0.26	0.07	0.24
	std.	0.22	0.33	0.29	0.67	0.37	0.08	0.2
	Min.	0.0	0.01	0.03	0.0	0.0	0.0	0.04
	Max.	0.72	1.4	1.11	1.7	1.11	0.16	0.55
vy [m/s]	MAE	0.24	1.16	0.61	0.6	0.11	0.25	0.13
	std.	0.43	1.42	0.69	0.84	0.16	0.3	0.15
	Min.	0.01	0.03	0.01	0.02	0.02	0.03	0.02
	Max.	2.86	3.76	1.64	1.98	0.46	0.58	0.27

4.2.3 VRU Prediction Accuracy

Standard trajectory prediction evaluation approaches assess prediction accuracy reporting the average displacement error (ADE) and final displacement error (FDE) for a fixed prediction horizon (Munoz Sanchez, Elfring, Silvas, Molengraft, & Rene, 2022). If predictions are generated at every time step where a road user is visible, and their accuracy is assessed at each point of the prediction horizon, then there would be no distinction on its relevance for determining whether the vehicle's trajectory should have been altered.

To illustrate this situation, consider the example shown in Figure 27. Three predictions p^i, $i \in \{1,2,3\}$ generated for a pedestrian at different points in time for the next H seconds, resulting in final predicted positions p_H^i typically used to compute FDE, and intermediate positions p_t^i with $0 < t \leq H$ used to compute ADE. However, for each of the generated predictions, the horizon that can trigger an intervention (AEB or AES maneuver) could be different. For instance, p^1 does not overlap with the driving corridor and no maneuver is

This project has received funding from the European Union's Horizon 2020 research and innovation programme under Grant Agreement 861570.

triggered, p^2 enters the driving corridor at horizon h', while for p^3 this happens towards the middle of the prediction at horizon h''.

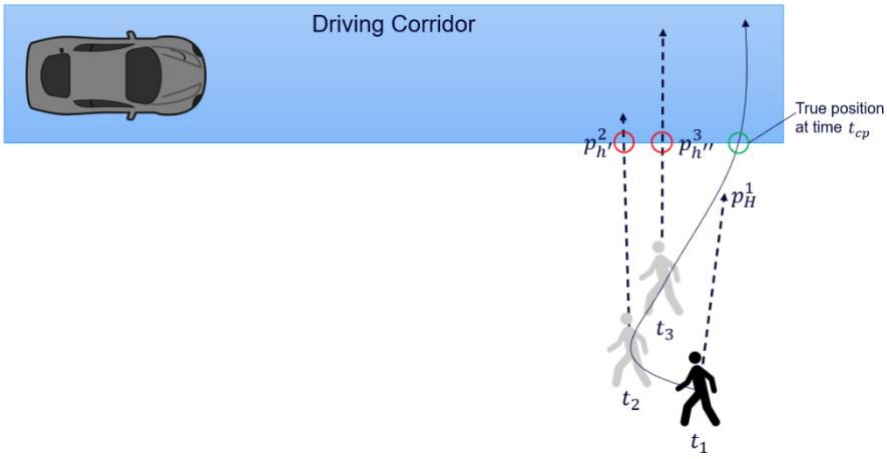

Figure 27: Illustration of the reason for deviating from standard prediction evaluation practices. The part of the prediction causing an emergency maneuver might occur at different horizons, hence accuracy is reported for this point.

We are interested in assessing predictive accuracy at the point where an emergency maneuver is triggered. To that end, we deviate from standard evaluation practices and compute FDE as follows:

1. For each VRU, determine t_I, the time at which a VRU prediction ultimately triggers an emergency maneuver.
2. For each VRU prediction, determine the predicted position corresponding to time t_I. If no such position is available, that prediction is not considered for evaluation.
3. Use those predicted positions to compute FDE w.r.t. the VRU's ground truth position at time t_I. In the reported figures t_I corresponds to time = 0 seconds, and negative values denote how much time prior to t_I the VRU was visible and the prediction was made. Hence, a time of –2 seconds corresponds to predictions made 2 seconds before the VRU (prediction) enters the driving corridor and triggers an emergency maneuver.

Prediction accuracy is heavily affected by tracking accuracy, and since high-fidelity tracking is not always available, two evaluations are performed to validate the prediction module: one where the tracking from the demonstrator vehicle is used directly, and one where the reference data from the dummy system is used to simulate a high-fidelity state of the art tracking system. Figure 28 shows the mean and standard deviation of the predictions' FDE at the intervention time based on 89 measurements. For clarity, specific values at certain horizons can be found in Table 10As can be observed in the figures, under the lower-fidelity tracking system, the FDE of the predictions before intervention time is approximately 1.5m with significant variance. In contrast, with the high-fidelity tracking system, the FDE remains

This project has received funding from the European Union's Horizon 2020 research and innovation programme under Grant Agreement 861570.

below 0.4 with significantly lower variance, highlighting the potential enhancements of the prediction module through the use of a more mature perception module.

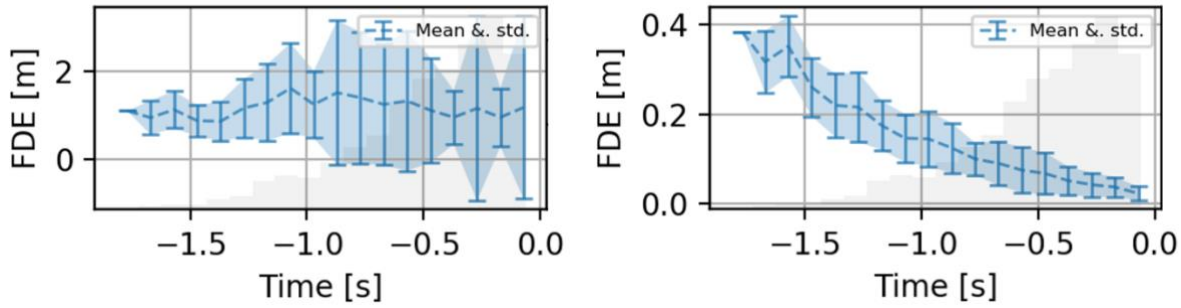

Figure 28: FDE mean and standard deviation of predictions when using lower-fidelity object tracking (left) and high-fidelity object tracking (right).

Table 10: FDE mean and standard deviation of some prediction horizons when using lower-fidelity object tracking and high-fidelity tracking.

	Time [s]	-1.6	-1.3	-1.0	-0.7	-0.4	-0.1
Lower-fidelity tracking	FDE [m]	1.37	1.55	1.59	1.38	1.47	1.37
	FDE std. [m]	0.31	0.22	0.6	0.69	0.8	0.92
High-fidelity tracking	FDE [m]	0.4	0.33	0.18	0.11	0.07	0.03
	FDE std. [m]	0.0	0.05	0.09	0.07	0.03	0.02

4.2.4 Crash Prediction & Avoidance Estimation

The crash prediction and avoidance estimation are performed by a risk-based algorithm, see (Löffler, et al., 2022). The algorithm decides whether to perform an AEB, AES, or nominal following manoeuvre. We measure the performance of the decision-making by placing the test vehicle within a scenario, where only one decision is correct. By repeated testing, we measure the number of correct decisions. Additionally, we measure the false-positive and false-negative decisions.

4.2.4.1 Test Scenario

The test scenario is presented in
Figure 29. Given that no collision will occur, i.e., the VRU passes before or after the ego vehicle, the ego vehicle should follow a nominal trajectory. In case of a collision, the vehicle should perform an AEB maneuver if it will entirely avoid the collision. If AES is the only option to avoid a collision successfully, the ego vehicle should follow an AES trajectory. To provoke a triggering of an AES maneuver, an obstruction is placed such that the ego vehicle detects the VRU at a given time (dependent on the placement of the obstruction). If the obstruction is placed close to the VRU, the stopping distance would exceed the remaining distance to

This project has received funding from the European Union's Horizon 2020 research and innovation programme under Grant Agreement 861570.

the VRU, in that case, only AES would be viable. Therefore, this scenario is sufficient to test the full range of the decision-making process. The ego vehicle velocity is throughout all tests 50 kph and the VRU's velocity is 3 kph. The impact point of the VRU onto the ego vehicle is defined to be the front right corner. To trigger an AEB decision, the variable distance of the obstruction is 3.65 m, leaving enough time to safely execute an AEB. For the AES test case, the variable obstruction distance was 1.25 m. Thus, the detection is too late for executing an AEB, such that AES is the only option to avoid an accident.

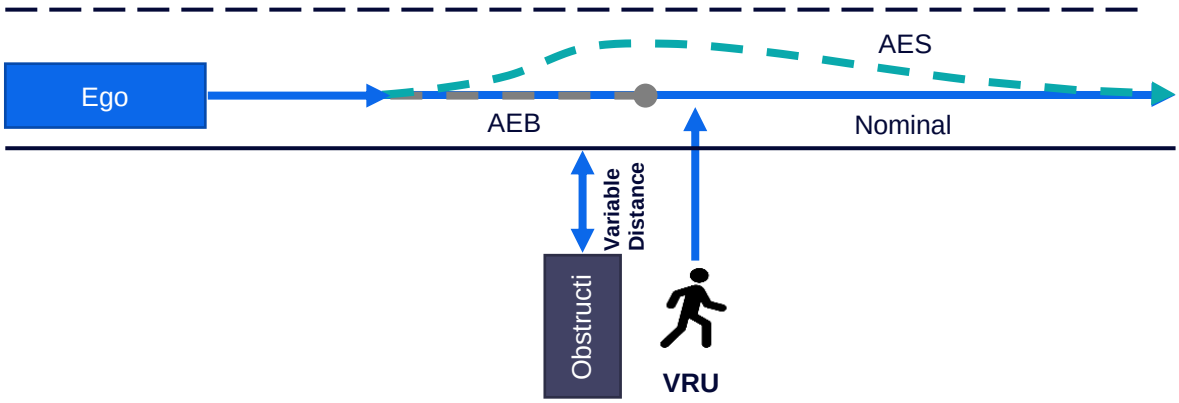

Figure 29: Testing setup for the risk-based decision-making.

4.2.4.2 Results

In total 43 test runs where performed. The results of the repetitive test runs are displayed in Table 11.

Table 11: Testing results, risk-based decision-making.

In Table 11, it can be seen that five out of 16, times the system decided to execute an AEB maneuver, even though a different maneuver would have been the correct decision. The high number of wrong decisions can be attributed to the system's parameterization. The system is tuned such that when high uncertainty about the VRU's trajectory is present, an AEB maneuver is generally preferable. This is because breaking always reduces the kinetic energy of a potential collision and thus is said to be the safe option if information (i.e., measurement and estimation) is inconclusive.

Regarding the AES, the decisions were correct for all test cases. Nevertheless, two collisions occurred. These collisions represent side impacts where full avoidance was not possible. The severity and relevance of these collisions are not investigated in this project. Still, we speculate that two factors are relevant to consider. First, the dummy system always keeps walking in the forward direction, even if the vehicle side is already facing the dummy. This behaviour must not represent human behaviour. Second, the injuries sustained from a side collision instead of a head-on collision may be less severe.

This project has received funding from the European Union's Horizon 2020 research and innovation programme under Grant Agreement 861570.

The nominal maneuver test in Table 11 can be understood as a false-positive test. While half of the decisions were incorrect, none of the taken decisions led to a collision. Out of the six wrong decisions, three were decided to an AES and AEB, respectively. To improve the false positive rate, less uncertainty in measurement and estimation is required, such that more accurate collision timing and positions can be computed. The tolerances in the measurement and estimation pipeline are provided in the previous Sections 4.2.2 and 4.2.3.

4.2.5 Trajectory following

Trajectory following performance is assessed using the data acquired during the Demo 3 physical testing activities (SAFE-UP, 2023). The data is comprised of 66 AES maneuvers and 61 AEB maneuvers, that were recorded with full logging of the trajectory planners employed in the trajectory generation module (c.f. Figure 19, block 9), the outputs of the vehicle control module (c.f. Figure 19, block 11) and logging of the vehicle state in terms of its position, orientation, velocity, acceleration (using a iMAR iTraceRT 402/7 GNSS+IMU unit (iMAR) equipped to the demonstrator.) and road wheel angle (as reported by the vehicles steering system).

Based on this data, the trajectory following performance is quantified in terms of deviations of the planned vehicle states from the and actual vehicle states, where the following quantities have been chosen for the analysis:

- the longitudinal deviation $\Delta x(t) = x_{\text{driven}}(t) - x_{\text{planned}}(t)$ of the vehicle position from the planned trajectory,
- the lateral deviation $\Delta y(t) = y_{\text{driven}}(t) - y_{\text{planned}}(t)$ of the vehicle position from the planned trajectory,
- the deviation $\Delta\Psi(t) = \Psi_{\text{driven}}(t) - \Psi_{\text{planned}}(t)$ of the actual vehicle orientation (yaw) from its planned orientation,
- the deviation $\Delta\delta(t) = \delta_{\text{driven}}(t) - \delta_{\text{planned}}(t)$ of the vehicle road wheel angle and
- the deviation $\Delta a_x(t) = a_{x\,\text{driven}}(t) - a_{x\,\text{planned}}(t)$ of the vehicle's longitudinal acceleration.

Here the "planned" subscript is used to indicate quantities planned by the trajectory generation module, whereas the "driven" subscript indicates vehicle quantities measured during the execution of the maneuvers. All quantities except the road wheel angle and the vehicle orientation are given in the body frame of the vehicle at time t with its origin at the center of the demonstrator's rear axle.

Each maneuver contains an initial part of nominal driving (following of nominal trajectories) when the vehicle approaches the testing site and the actual emergency maneuver (following of emergency trajectories) itself. During nominal driving, a cyclic replanning of the vehicles trajectory is performed at a rate of about 200ms, where each trajectory planning is initialized with the current vehicle state (Löffler, et al., 2022). In between two trajectory plannings, the

This project has received funding from the European Union's Horizon 2020 research and innovation programme under Grant Agreement 861570.

vehicle is operated by a feed-forward control of the road wheel angle δ, based on the last planned trajectory only. The overall planned trajectory for nominal driving therefore consists of a concatenation of trajectory sections each covering a duration of about 200 ms that is discontinuous, due to the reinitialization of trajectory planners to the actual vehicle state. During the emergency part of the maneuver, the planning behaviour is changed. For an AEB maneuver, further trajectory planning is stopped once the braking system is engaged, as the maneuvers are always planned to bring the vehicle to standstill utilizing the maximum available deceleration. Thus, additional trajectory replanning cannot lead to any change in the employed control action. During an AES maneuver, cyclic replanning is performed to be able to adapt to changes of the motion of the VRU that shall be evaded. Here the trajectory planning is not reinitialized with the actual vehicle state, but with the state planned by the last planning iteration for the current point (Löffler, et al., 2022) This leads to continuous planned AES trajectories.

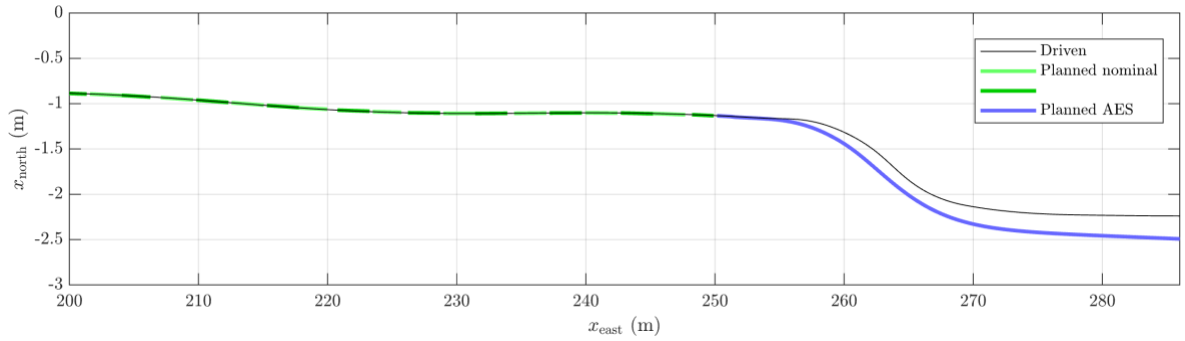

Figure 30: Exemplary trajectory of an AES maneuver displayed in an earth-fixed frame.

An example of the trajectories of such a maneuver is depicted in Figure 30. There, the planned nominal trajectory is given as green solid line where the individual replanning section is indicated by the interleaving light and dark color-tones. The emergency part of the maneuver is an AES maneuver, where the respectively planned trajectory is given as blue solid line. The black thin solid line displays the actually driven trajectory of the vehicle.

A detailed report on the developed trajectory generation, trajectory selection logic and vehicle control can be found in (Löffler, et al., 2022). Here it shall be noted, that due to unforeseen problems of the demonstrator vehicle, it was not possible to implement the high-frequency trajectory tracking controllers described in (Löffler, et al., 2022) within the time frame of the SAFE-UP project. Hence all driving is based on a low-frequency feedback control realized via the cyclic trajectory replanning and planner initialization on the current vehicle state. During each iteration of this feedback loop, the vehicle is controlled using feed-forward control of the steering angle and longitudinal acceleration only.

The following subsections will characterize the trajectory following performance of the demonstrator separately for nominal driving, AES maneuvers and AEB maneuvers, to be able to fairly evaluate the specifics of each trajectory planning.

This project has received funding from the European Union's Horizon 2020 research and innovation programme under Grant Agreement 861570.

4.2.5.1 Nominal trajectory following

Due to the fact that each planning cycle reinitializes the nominal trajectory planner to the current vehicle state and as such the deviations between planned and actually driven trajectory are reset at each time of replanning, the evaluation of nominal trajectory following is performed on the level of trajectory sections.

The physical testing data contains about 10000 nominal trajectory sections, with each planned trajectory sampled at a time discretization of 20 ms. For each sampled time step the deviations between planned and driven trajectories are calculated and estimations of their probability density distribution are performed by the computation of histograms of the respective data (probability density of each histogram bin is estimated as relative frequency divided by bin width).

Figure 31 shows timeseries of histograms for the deviations of roadwheel angle $\Delta\delta(t)$, vehicle yaw $\Delta\Psi(t)$, and vehicle position in its longitudinal and lateral directions $\Delta x(t)$ and $\Delta y(t)$, where $t = 0$ is the time of trajectory replanning for each section. The first sample of a planned trajectory corresponds to $t = 0.02\,\mathrm{s}$. For each series of distributions, the overlayed solid line displays the median of the respective quantity ($\widetilde{(\cdot)}$) and the dashed lines display the bounds of the 68.28% confidence interval ($\mathrm{CI}_{68}(\cdot)$) centred around the median.

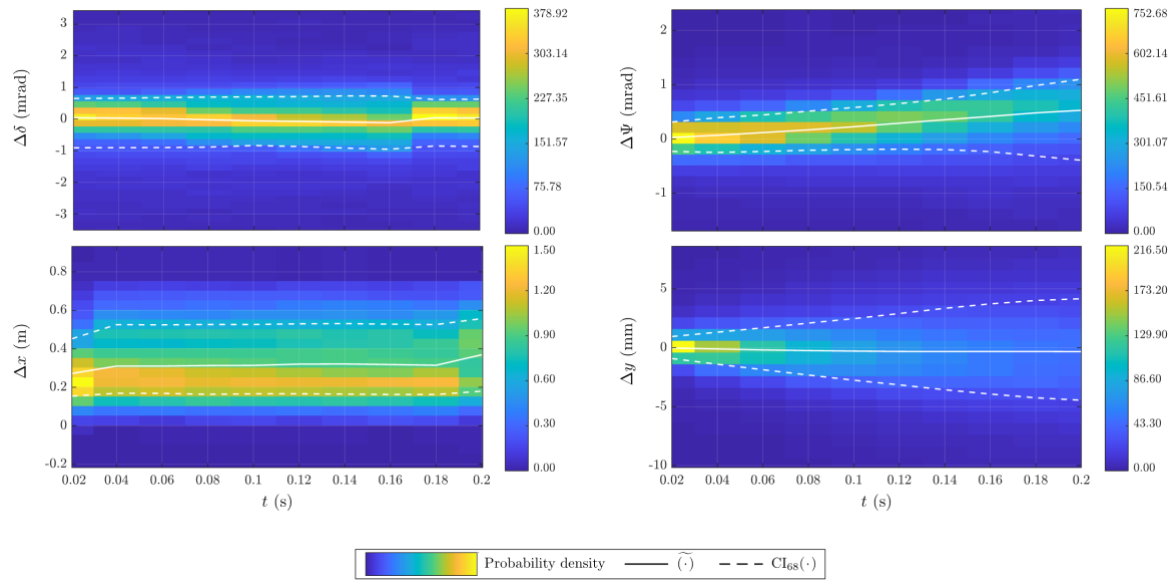

Figure 31: Distribution of deviations between planned and driven nominal trajectories.

The deviations of roadwheel angle primarily characterize the accuracy of the steering system and yield a maximum confidence interval of $\mathrm{CI}_{68}(\Delta\delta) = [-0.95, 0.72]\,\mathrm{mrad}$ for nominal (straight) driving. The seemingly abrupt change in the time evolution of the distribution of deviations at a time of about $t = 0.18\,\mathrm{s}$ originates in the compensation of the steering systems dead time that is incorporated in the trajectory planning. At each replanning the dead time of the steering system of about $\tau_{\mathrm{dead}} = 0.16\,\mathrm{s}$ forces the trajectory planners

This project has received funding from the European Union's Horizon 2020 research and innovation programme under Grant Agreement 861570.

to not directly use the current vehicle state (at $t = t_{\text{plan}}$) for initialization, but use a prediction of the state evolution (including δ) from $t = t_{\text{plan}}$ to $t_{\text{init}} = t_{\text{plan}} + \tau_{\text{dead}}$ to estimate the correct initialization state. During this timespan, the road wheel angle is governed by the respective parts of the previously planned trajectory due to the systems dead time. As such the road wheel angle at time t_{init} is estimated by $\delta(t_{\text{init}}) = \delta_{\text{driven}}(t_{\text{plan}}) + \int_{t_{\text{plan}}}^{t_{\text{init}}} \mathrm{d}t\, \dot{\delta}_{\text{prev}}(t)$, which should approximate the steering systems internal controller behaviour. Here, $\delta_{\text{driven}}(t_{\text{plan}})$ is the actual road wheel angle at the time of replanning as reported by the steering system and $\dot{\delta}_{\text{prev}}(t)$ is the road wheel angle velocity of the previously planned trajectory. The errors of those approximations accumulated over the timespan of the dead time lead to slight discontinuities in the planned road wheel angle that can be observed as the abrupt change of the deviation distribution.

The deviations of the vehicle yaw display a second important trait of the demonstrator vehicle. Besides the expansion of the yaw confidence interval $\mathrm{CI}_{68}(\Delta\Psi)$ over the timespan of one trajectory section that is to be expected due to the lack of any feedback control on these timescales, also an approximately linear evolution of the distributions median $\widetilde{\Delta\Psi}$ can be observed. This increasing error in the vehicles orientation is caused by a residual offset error of the steering systems road wheel angle sensor that remains after calibration of the system. During nominal driving this error is compensated by the cyclic reinitialization of the trajectory planner to the actual vehicle state resulting in a maximum confidence interval of $\mathrm{CI}_{68}(\Delta\Psi) = [-0.4, 1.1]\ \mathrm{mrad}$.

For the deviations of the vehicles position from the planned trajectory in longitudinal direction Δx, an offset can be observed that is almost constant within a replanning cycle and exists even at the first sampling time after replanning$t = 0.02$ s). This offset reveals a previoulsy unknown bug in the control of the demonstrator vehicle that leads to an off-by-one error in the execution of planned trajectories in general. That is, there is a one-time sample (20 ms) offset between the actual and the assumed execution of the control actions. In the physical testing scenarios, the demonstrator drives at a speed of about 13.9 m/s, which then corresponds to a change in longitudinal position of about 0.27 m within 20 msΔx). The overall errors that are introduced by this time mismatch of 20 ms $\mathrm{CI}_{68}(\Delta\mathrm{x}) - \widetilde{\Delta\mathrm{x}} = [-0.18, 0.56]\ \mathrm{m}$). It has to be noted that the longitudinal motion of the vehicle during nominal driving is assumed to at constant speed and not under active control of any system component, but controlled by the driver only.

The deviations of the vehicles position from the planned trajectory in lateral direction Δy show the expected behaviour of an approximately linear expansion of the distribution's confidence interval $\mathrm{CI}_{68}(\Delta\mathrm{y})$, while the median is almost constant$\widetilde{\Delta\mathrm{y}} \approx 0$). The$\mathrm{CI}_{68}(\Delta\mathrm{y}) = [-4.4, 4.1]\ \mathrm{mm}$).

4.2.5.2 AES trajectory following

In difference to nominal trajectory following, the evaluation of AES trajectory following is performed on the full maneuver level.

This project has received funding from the European Union's Horizon 2020 research and innovation programme under Grant Agreement 861570.

The available data contains 66 AES maneuvers, where 12 maneuvers execute an evasive trajectory in direction of the vehicles left side (in the following referred to as *left-sided AES*) and 54 maneuvers execute the respective maneuver in direction of the vehicles right side (in the following referred to as *right-sided AES*). Due to the residual offset error of the steering systems road wheel angle sensor (c.f. Section 4.2.5.1), and the fact that the AES trajectory planner is not reinitialized based on the actual vehicle state during its replanning cycles, the driven trajectories differ significantly between left-sided and right-sided AES. Figure 32 shows a comparison of the vehicle's road wheel angle δ and yaw angle Ψ for (a) left-sided AES maneuvers and (b) right-sided AES maneuvers. The upper row depicts the median of all planned and actually driven road wheel angle trajectories ($\tilde{\delta}_{\text{planned}}$ and $\tilde{\delta}_{\text{driven}}$) and their median-centered 68.28% confidence intervals ($\text{CI}_{68}(\cdot)_{\text{planned/driven}}$) and the lower row the respective quantities of the vehicles yaw angle.

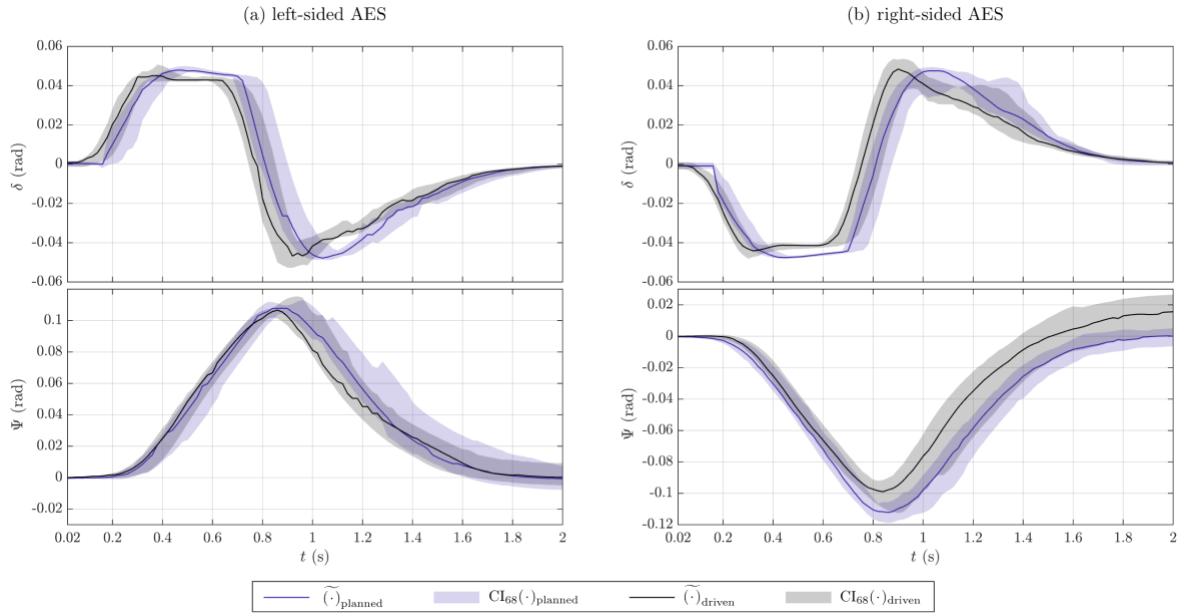

Figure 32: Road wheel angle and yaw during left-sided and right sided AES maneuvers.

Besides a flipped sign, there is no significant difference between the road wheel angles for left-sided and right-sided AES. The same holds true for the planned yaw angle of the maneuvers. For the yaw angle that was realized by the vehicle during the maneuvers Ψ_{driven}, the effects of accumulating the residual offset error of the steering system is clearly visible and results in an error of about 0.02 radians at the end of a right-sided AES. Due to that, the analysis of the AES trajectory following performance must be performed separately for left-sided and right-sided AES maneuvers.

The analysis is done in the same way as the analysis of the nominal trajectory following. For each sampled time step the deviations between planned and driven trajectories are calculated and based on these estimates of their probability density distribution are computed. Figure 33 shows the timeseries of histograms for the deviations of roadwheel

This project has received funding from the European Union's Horizon 2020 research and innovation programme under Grant Agreement 861570.

angle $\Delta\delta(t)$, vehicle yaw $\Delta\Psi(t)$, and vehicle position in its longitudinal and lateral directions $\Delta x(t)$ and $\Delta y(t)$, where $t = 0$ is the time of the planning of the initial AES trajectory. For each series of distributions, the overlayed solid line displays the median of the respective quantity ($\widetilde{(\cdot)}$) and the dashed lines display the bounds of the 68.28% confidence interval ($\mathrm{CI}_{68}(\cdot)$) centred around the median.

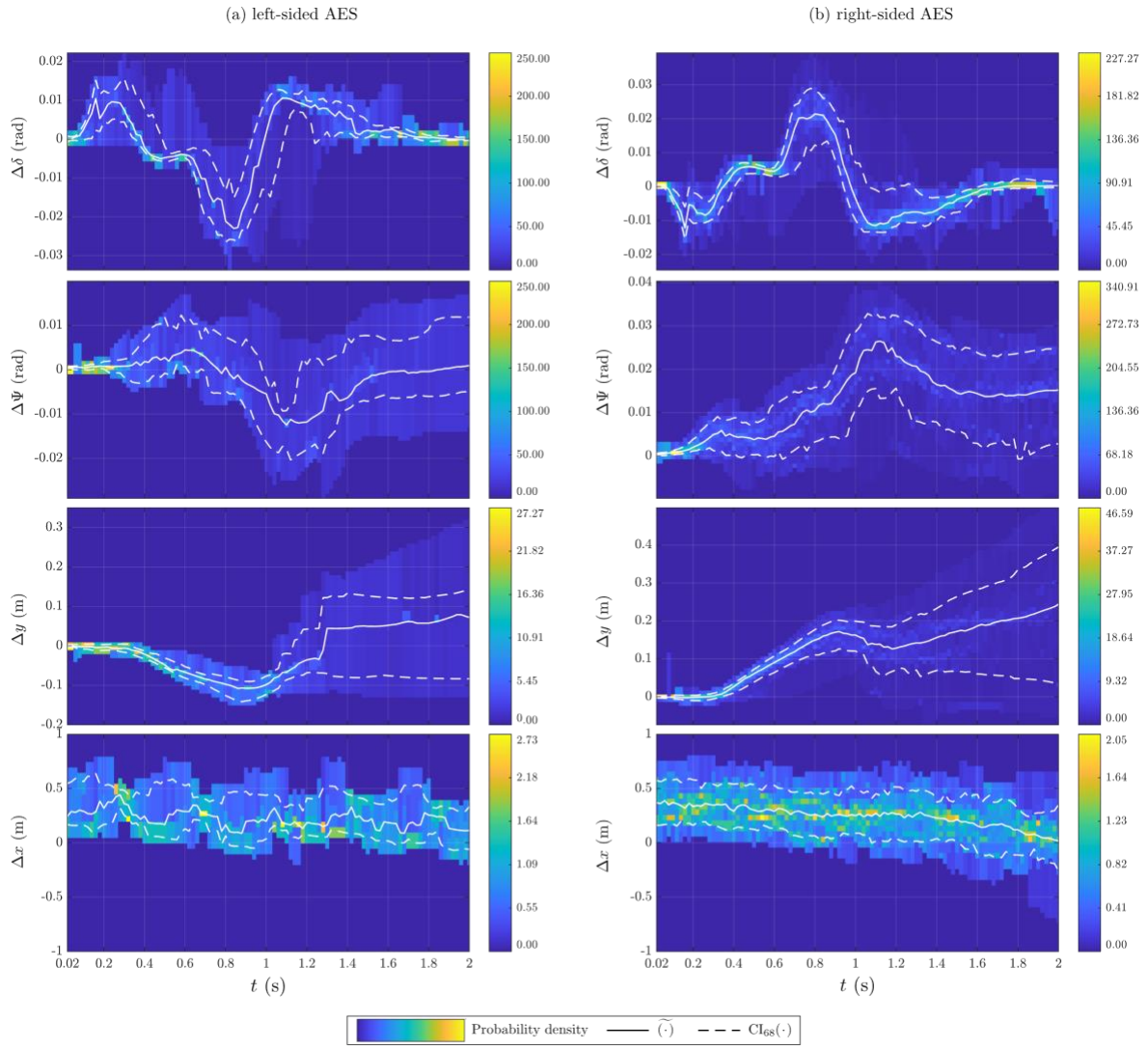

Figure 33: Distribution of deviations between planned and driven AES trajectories.

As the AES maneuver is designed to utilize the available dynamics of the steering system to maximum extent (Löffler, et al., 2022) also the deviations of roadwheel angle increase by about one order of magnitude compared to nominal trajectory following. For the latter, the steering systems controller was able to quite accurately follow the quasi-static requests, resulting in deviations on the milliradian level. For the AES maneuvers this level of deviations can be observed only at the beginning and the end of the maneuver when steering dynamics

This project has received funding from the European Union's Horizon 2020 research and innovation programme under Grant Agreement 861570.

are low. During the high-dynamics part (between $t \approx 0.1\ s$ and $t \approx 1.5\ s$) deviations of up to $\pm 30\ \mathrm{mrad}$ can be observed. These deviations are mainly a result of the fact, that the trajectory generation models the behaviour of the closed-loop steering system as just a signal delay (or dead time) between requested and actual road wheel angle (while as well taking constraints of the system performance regarding amplitude and velocity into account (Löffler, et al., 2022)), while the real behaviour of the closed-loop system is more complex. Therefore, the delay assumed by the trajectory planners (τ_{dead}) is a compromise between matching the dynamic steering behaviour during an AES maneuver and matching the less dynamic steering behaviour during nominal driving. As can be seen in Figure 32 this results in a slight overestimation of τ_{dead} by about 50 ms, compared to a delay estimation that would be optimized solely for the AES maneuver.

The deviations of the vehicle yaw angle depict what has already been discussed above. Due to the residual error of the steering systems road wheel angle sensor, a significant deviation between planned and driven trajectories is accumulated during the right-sided AES maneuver, leading to a final vehicle orientation that is not parallel to its initial orientation at the start of the maneuver. The final vehicle yaw deviation (at time $t = 2\ s$) is characterized by a confidence interval of $\mathrm{CI}_{68}(\Delta\Psi) = [-5, 12]\ \mathrm{mrad}$ for the left-sided AES and $\mathrm{CI}_{68}(\Delta\Psi) = [3, 25]\ \mathrm{mrad}$ for the right-sided AES.

The deviations of the vehicles lateral position Δy are affected by the same effect. Besides this, the confidence intervals of the lateral deviations expand through the course of the maneuver as expected for a system without feedback control subject to external disturbances. For the left-sided AES, this leads to a confidence bound of about $[-0.14, 0.14]\ \mathrm{m}$ over the full maneuver duration and of about $[-0.01, 0.38]\ \mathrm{m}$ for the right-sided AES.

These results strongly show the necessity of the originally planned implementation of a feedback loop for the execution of the AES maneuvers (Löffler, et al., 2022), either via a (low-frequency) cyclic reinitialization of the trajectory planner with the actual vehicle state and/or a (cascaded) high-frequency trajectory tracking control.

As expected for a maneuver that executes no control on the vehicles longitudinal motion, the deviations of the vehicles longitudinal position do neither differ between left-sided and right-sided AES nor in comparison to the deviations observed during nominal driving (c.f. Figure 31). A slight decrease of the deviations over the duration of the AES maneuver can be observed, that originates in the manual control of the vehicle's velocity by the test driver: once the AES maneuver is initiated the driver most often stops his active control of the velocity and disengages the throttle, such that the vehicles speed is slowly reduced by air and road friction.

4.2.5.3 AEB trajectory following

AEB trajectories are identical to nominal trajectories (in terms of executed control as well as in terms of replanning cycle and reinitialization of the trajectory planner with the actual vehicle state) up to the point in time ($t = t_{\mathrm{brake}}$) where the braking system is engaged

This project has received funding from the European Union's Horizon 2020 research and innovation programme under Grant Agreement 861570.

(Löffler, et al., 2022). As explained in the beginning of Section 4.2.5, no further trajectory planning is executed after t_{brake} and the steering system is constantly requested with road wheel angle of $\delta = 0$. As such performance of the AEB trajectory following is identical to nominal trajectory following prior to t_{brake} and only maneuver date post t_{brake} will be included in the analysis presented in this section.

Figure 34 shows a comparison of the planned and driven longitudinal acceleration of the vehicle in terms of the median of all planned and driven acceleration trajectories ($\widetilde{a_x}_{\text{planned}}$ and $\widetilde{a_x}_{\text{driven}}$) and their median-centered 68.28% confidence intervals ($\text{CI}_{68}(\cdot)_{\text{planned/driven}}$), where $t = 0$ is the time of initially engaging the braking system. The model of the braking dynamics that is used for trajectory planning assumes an acceleration build up with a constant gradient, followed by constant acceleration until vehicle standstill. The overall maneuver is delayed by a system dead time caused by communication delay and the time needed to pressurize the brakes hydraulics (see (Löffler, et al., 2022), Section 4.2.5.3 for details). The model assumptions for the gradient of the acceleration build up matches the real braking system reasonably well, but the assumed dead time is overestimated by about 90 ms. In addition, there are two effects originating from the braking system controller that are not covered by the employed model. The first effect is the overshoot of the actual acceleration over the request ($-8\ \text{m/s}^2$) between $t \approx 0.3$ s and $t \approx 0.75$ s. The second effect is the reduction of acceleration for low vehicle speeds that can be observed between $t \approx 1.7$ s and $t \approx 2.0$ s. The final overshoot and slight oscillation of the actual vehicle acceleration beginning at $t \approx 2.0$ s is a measurement artifact: the vehicle frame is rocking back and forth due to the suspension of the vehicle chassis. This acceleration does not cause a real longitudinal movement of the car (as it can also be seen from the time evolution of the deviation in longitudinal position depicted in Figure 35). The variation in the duration of the planned vehicle acceleration that causes the increase in $\text{CI}_{68}(a_x)_{\text{planned}}$ when switching from maximum back to zero acceleration is caused by the variation of initial speeds of the vehicle.

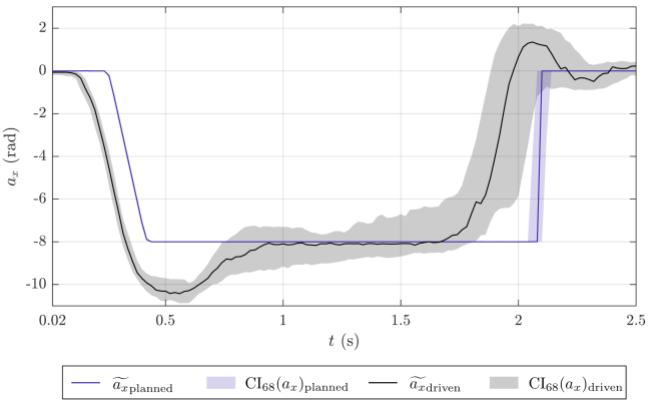

Figure 34: Longitudinal acceleration during the AEB maneuvers.

This project has received funding from the European Union's Horizon 2020 research and innovation programme under Grant Agreement 861570.

Figure 35 again shows the timeseries of histograms for the deviations of longitudinal acceleration $\Delta a_x(t)$, vehicle yaw $\Delta\Psi(t)$, and vehicle position in its longitudinal and lateral directions $\Delta x(t)$ and $\Delta y(t)$, where $t = 0$ is the time of initially engaging the braking system. For each series of distributions, the overlayed solid line displays the median of the respective quantity ($\widetilde{(\cdot)}$) and the dashed lines display the bounds of the 68.28% confidence interval ($\mathrm{CI}_{68}(\cdot)$) centred around the median.

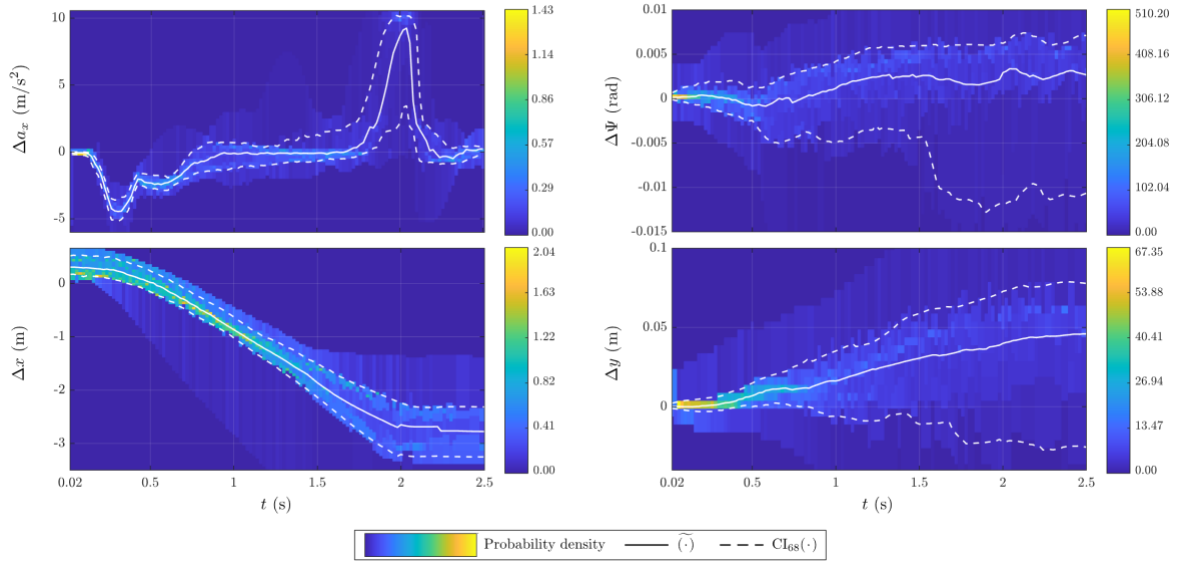

Figure 35: Distribution of deviations between planned and driven AEB trajectories.

The deviations of the longitudinal acceleration Δa_x also clearly reveal the effects regarding the mismatch between the model of the braking dynamics and the real vehicles braking dynamics that has been discussed above.

The deviations of the vehicles yaw $\Delta\Psi$ increase slowly over the duration of the maneuver as expected from the prior discussions on the residual offset error of the steering systems road wheel angle sensor. Although, for the AEB maneuvers the effect is mitigated by the decreasing vehicle speed.

The same effect can be observed for the deviations of the vehicles lateral position Δy. The deviations show a significant systematic shift during the AEB maneuver, that is caused by the residual road wheel angle error. In addition, disturbances of the road wheel angle caused by the strong forces acting on the steering rack during an emergency braking maneuver result in a 30-fold expansion of the deviations confidence interval from about $\mathrm{CI}_{68}(\Delta \mathrm{y}) = [-1.1, 2.2]\ \mathrm{mm}$ at the beginning of the maneuvers to about $\mathrm{CI}_{68}(\Delta \mathrm{y}) = [-25, 78]\ \mathrm{mm}$ when the vehicle is at standstill.

The deviations of the vehicles longitudinal position Δx show the results of the mismatch between modelled and real braking dynamics with respect to the vehicle's assumed and actual braking distance. The underestimation of the vehicle's acceleration build-up in the

This project has received funding from the European Union's Horizon 2020 research and innovation programme under Grant Agreement 861570.

beginning of the maneuver (between $t \approx 0.3$ s and $t \approx 0.75$ s) leads to a quasi constant increase of Δx during mid-maneuver (between $t \approx 0.75$ s and $t \approx 1.7$ s). During these periods, the width of the confidence interval $\mathrm{CI}_{68}(\Delta \mathrm{x})$ is approximately constant (at about 0.4 m) and compatible to those observed during nominal driving. Only at the end of the maneuver, when the vehicle speed dependent reduction of acceleration takes place (between $t \approx 1.7$ s and $t \approx 2.0$ s), the width of the confidence interval expands to about 0.9 m, which reflects the variations in braking distance due to the variation of initial vehicle speeds.

The confidence interval of Δx at the end of the AEB maneuvers (vehicle at standstill) is given by $\mathrm{CI}_{68}(\Delta \mathrm{x}) = [-2.4, -3.3]$ m.

This project has received funding from the European Union's Horizon 2020 research and innovation programme under Grant Agreement 861570.

5. Demo 4

5.1 High Level Description

The overarching goal of Demo 4 is the development of a VRU C-ITS communication system, which can provide information to and between road users via On-Board-Units for bicyclists, Road-Side-Units (RSUs), and vehicles. Multiple Deliverables are available, which describe the developed system and functionalities. Deliverable (Nikolaou, et al., D3.1 Active Safety Systems Specification and Risk Analysis , 2021) and (Nikolaou, et al., D3.9 Active Safety Systems Specification and Risk Analysis Update, 2022) for the component specification and risk assessment, D.3.7 (Nikolaou, Castells, Lorente Mallada, Gragkopoulos, & Tsetsinas, D3.7 Demo 4 System for on-time warning provisions to VRUs and drivers in critical condiions update, 2022) for the Demo 4 demonstrator presentation (Balint, et al., 2022) and (Kovaceva, et al., 2023) for the safety performance assessment of the Demo 4 technology. In this Deliverable the technical verification of Demo 4 components is documented. For Demo 4, this will be done in two separate steps. In Sections 5.2 and 5.3, the module, component and system verification are shown. The Basis and terminology used for this is the INCOSE Systems Engineering Handbook (ISO15288) technical verification process. Moreover, the assumptions that were made and the technical feasibility for the performance simulation are assessed and documented in terms of validity.

The INCOSE Systems Engineering Handbook describes the complete systems engineering process. The process and terminology of technical verification was used and applied to the technical requirements for Demo4 components and (sub-)systems. The Verification Techniques from INCOSE are described in Section 2.

5.2 Module and Component Requirement Verification

This Section describes the individual verified requirements for Demo 4 modules and components. In Table 12 the different key modules, main requirements, the verification criteria and techniques are described. Additionally, the failed and passed criteria are documented. Results, which are part of the already given deliverables, are not documented any further, but referenced to the corresponding SAFE-UP literature.

The different key modules, main requirements, the verification criteria and techniques are described. Additionally, the failed and passed criteria are documented.

This project has received funding from the European Union's Horizon 2020 research and innovation programme under Grant Agreement 861570.

Table 12: Demo 4 module verification.

Index	Requirement	Verification Criteria	Verif. Tech.	Result (passed, failed)
All Communication modules				
1	all modules shall be able to communicate with CAM messages via ITS-G5	Communication signal	Test	Passed. Verification included in D3.4
2	all modules shall be able to communicate in a range of 150m via ITS-G5 in open space	Valid range	Test	Passed; with a range of at least 150m. Results in section 5.2.1
VRU communication module				
3	the VRU-pedestrian-module shall be able to encode and transmit CAM messages with 10 Hz rate (1 CAM transmission every 100 ms)	Valid CAM transmission, with the specified rate	Test	Passed Results in D3.4
4	The VRU pedestrian module shall be able to receive and decode CAM messages from the vehicle's communication module according to its transmission rate (agreed at 10 Hz).	CAM reception and successful decoding	Test	Passed Results in D3.4
5	the VRU-bicyclist module shall be able to encode and transmit CAM messages with 10 Hz rate (1 CAM transmission every 100 ms)	Valid CAM transmission, with the specified rate	Test	Passed Results in D3.7
6	the VRU-bicyclist module shall be able to receive and decode CAM messages from the vehicle's communication module	CAM reception and successful decoding	Test	Passed Results in D3.7

This project has received funding from the European Union's Horizon 2020 research and innovation programme under Grant Agreement 861570.

	according to its transmission rate (agreed at 10 Hz).			
7	The CAM message shall at the very least include location coordinates, heading, speed, station type	Valid available information in the corresponding fields	Test	Passed
Vehicle Function Module (IDIADA)				
8	The vehicle module shall be able to send and receive CAM-signals to the within 10Hz (max 100ms/signal).		Test	Passed Results in D3.7 and section 5.2.2
9	V2X latency (from app to app) shall be lower than 100ms		Test	Passed, Results in section 5.2.3
10	A driver warning is triggered on-time prior the AEB		Test	Passed Results in section 5.2.4
11	The data fusion shall fuse V2X and perception data		Analysis	Passed Result in section 5.2.5
12	The perception shall be able to provide location coordinates, heading, speed and station type		Test	Passed Result in section 5.2.6
13	The CAM messages shall at the very least include {location coordinates, heading, speed, station type}		Test	Passed Result in section 5.2.7
14	It shall calculate the TTC and warning signal, AEB trigger		Simulations	Passed

This project has received funding from the European Union's Horizon 2020 research and innovation programme under Grant Agreement 861570.

			and tests	Results in section 5.2.4
RSU Function module (IDIADA)				
15	Shall detect targets, at least, at 10Hz		Test	Passed Results in section 5.2.8
16	the RSU--module shall be able to send CAM-signals to the function within 10Hz (max 100ms/signal)?		Test	Passed Results in section 5.2.3
17	The CAM message shall at the very least include location coordinates, heading, speed, station type		Test	Passed Results in section 5.2.7

The following sub-sections describe the verification techniques and the results followed during the verification processes for the different requirements.

5.2.1 Test Result communication module

The pedestrian VRU device was designed and developed in a portable way, such that a person can hold it conveniently in their hands without discomfort. This approach injected some challenges regarding the V2X communication part of the device and especially the used antennas. A normal C-ITS G5 communication module is installed in vehicles or road infrastructure where there is no lack of space and the antennas can permanently be installed in the most efficient orientation for best communication performance. This is not the case for a portable handheld device where everything is embedded inside its case and is meant to be carried by a human. For this reason, Demo 4 carried special communication tests to evaluate range vs received signal strength and packet loss for this device.

For the tests, the Demo 4 VRU device was mounted on a tripod at a height of approximately 1.40 meters. The VRU device transmitted V2X messages (CAM) at a constant rate of 10Hz.

The receiver device was also mounted on a tripod at a height of approximately 1.40 meters. This device received the CAM messages from the VRU device and calculated statistics about the RSSI levels and received packets for each test run. The V2X G5 antennas on this receiving device were dual dipole with 5 dBi gain.

This project has received funding from the European Union's Horizon 2020 research and innovation programme under Grant Agreement 861570.

In Figure 36 a photo illustrating both devices on the test field is presented.

Figure 36: Photograph of the RF communication test configuration.

The tripod with the VRU device was placed at four positions with **5**, **46**, **91** and **154** meters distance from the receiver. At every occasion there was **line of sight (LoS)** but since the test area was not fully closed, there were occasionally a few obstacles (moving vehicles) in-between that could not be avoided. At each position the VRU device was mounted with 4 different orientations presented in Figure 37 and Figure 38.

This project has received funding from the European Union's Horizon 2020 research and innovation programme under Grant Agreement 861570.

Figure 37: a) Orientation A (parallel to the ground)

This project has received funding from the European Union's Horizon 2020 research and innovation programme under Grant Agreement 861570.

Figure 38: Orientation B (perpendicular to the ground), c) orientation C (perpendicular to the ground and right hand 90° turn), d) orientation D (perpendicular to the ground and left hand 90° turn).

A total of 4x4 individual tests were conducted for every chosen position and orientation. Each test includes the transmission of V2X messages from the VRU device at a constant rate and the calculation of statistics on the receiver side. The obtained results are presented in Table 13.

This project has received funding from the European Union's Horizon 2020 research and innovation programme under Grant Agreement 861570.

Table 13: VRU device range test results - RSSI and packet loss ratio.

Distance (m)	Orientation	$RSSI_{Min}$ (dBm)	$RSSI_{Max}$ (dBm)	$RSSI_{Mean}$ (dBm)	Packet loss ratio
5	A	-53	-49	-50.87	< 1%
	B	-61	-53	-57	< 1%
	C	-64	-55	-60.45	< 1%
	D	-67	-57	-60.91	< 1%
46	A	-67	-58	-62.37	< 1%
	B	-69	-64	-66.53	< 1%
	C	-71	-64	-67.67	< 1%
	D	-75	-67	-69.87	< 1%
91	A	-71	-66	-69.12	< 1%
	B	-86	-74	-78.76	< 1%
	C	-88	-75	-80.53	< 1%
	D	-84	-76	-80.86	< 1%
154	A	-83	-67	-70.36	< 1%
	B	-91	-72	-75.5	< 1%
	C	-95	-76	-81.45	< 1%
	D	-95	-79	-86.77	< 1%

The results clearly show that the best orientation for the VRU device is the orientation A with regards to the RSSI of the opposite device, something that was expected, because it is the one with the most similarities with how a pedestrian may hold it and its antennas were designed with that in mind. In all cases, the communication can be considered reliable for all tested ranges. The maximum tested distance was the largest that we could achieve in our premises with the LoS condition existing.

This project has received funding from the European Union's Horizon 2020 research and innovation programme under Grant Agreement 861570.

5.2.2 Vehicle module V2X message rate

The standard (ETSI, 2019) defines the Cooperative Awareness (CA) service and establishes a variable message rate between 1 and 10 Hz, depending on “station” speed and on channel congestion, but for most cases it shall be set to 10Hz.

To ensure that the vehicle and RSU modules can send and receive messages at the required rate, a test scenario has been defined as indicated on Figure 39: V2X rate test scenario diagram. On test scenarios, the RSU module has been set to send CAM messages and in parallel, the vehicle module has been set as a receiver.

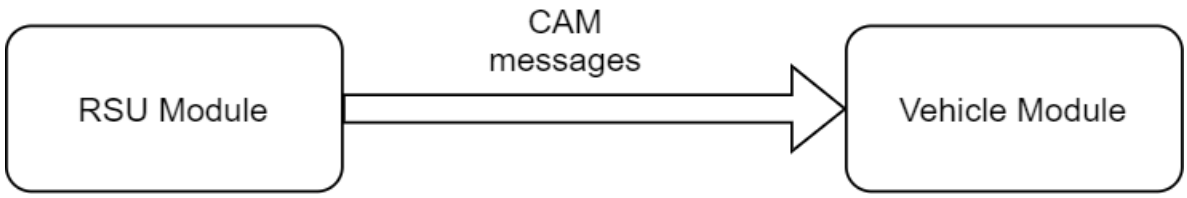

Figure 39: V2X rate test scenario diagram.

Both systems had logging activated so we could check how many messages have been sent, and how many of them were received. After analysing log files like the one shown on Figure 40, we can conclude that a sending/receiving rate of 10Hz is maintained throughout the entire test and no packets have been lost.

	Time	Source	Destination	Protocol	Length	Info
2	2023-04-05 11:33:21.249629	UnexTech_b6:73:00	Broadcast	ITS	131	CAM(v2)
3	2023-04-05 11:33:21.350137	UnexTech_b6:73:00	Broadcast	ITS	131	CAM(v2)
4	2023-04-05 11:33:21.449961	UnexTech_b6:73:00	Broadcast	ITS	131	CAM(v2)
5	2023-04-05 11:33:21.550257	UnexTech_b6:73:00	Broadcast	ITS	131	CAM(v2)
6	2023-04-05 11:33:21.650165	UnexTech_b6:73:00	Broadcast	ITS	131	CAM(v2)
7	2023-04-05 11:33:21.750389	UnexTech_b6:73:00	Broadcast	ITS	131	CAM(v2)
8	2023-04-05 11:33:21.850490	UnexTech_b6:73:00	Broadcast	ITS	131	CAM(v2)
9	2023-04-05 11:33:21.950434	UnexTech_b6:73:00	Broadcast	ITS	131	CAM(v2)
10	2023-04-05 11:33:22.049686	UnexTech_b6:73:00	Broadcast	ITS	131	CAM(v2)
11	2023-04-05 11:33:22.150243	UnexTech_b6:73:00	Broadcast	ITS	131	CAM(v2)
12	2023-04-05 11:33:22.250299	UnexTech_b6:73:00	Broadcast	ITS	131	CAM(v2)
13	2023-04-05 11:33:22.349608	UnexTech_b6:73:00	Broadcast	ITS	131	CAM(v2)
14	2023-04-05 11:33:22.450051	UnexTech_b6:73:00	Broadcast	ITS	131	CAM(v2)
15	2023-04-05 11:33:22.550244	UnexTech_b6:73:00	Broadcast	ITS	131	CAM(v2)
16	2023-04-05 11:33:22.650221	UnexTech_b6:73:00	Broadcast	ITS	131	CAM(v2)
17	2023-04-05 11:33:22.750344	UnexTech_b6:73:00	Broadcast	ITS	131	CAM(v2)
18	2023-04-05 11:33:22.850247	UnexTech_b6:73:00	Broadcast	ITS	131	CAM(v2)
19	2023-04-05 11:33:22.950114	UnexTech_b6:73:00	Broadcast	ITS	131	CAM(v2)
20	2023-04-05 11:33:23.050173	UnexTech_b6:73:00	Broadcast	ITS	131	CAM(v2)

Figure 40: Wireshark capture of V2X messages.

This project has received funding from the European Union’s Horizon 2020 research and innovation programme under Grant Agreement 861570.

5.2.3 RSU and Vehicle latency test

To evaluate the V2X latency, a testing application has been developed which sends a request to the RSU module (via UDP connection) to sends a V2X message with a specified content over IEEE 802.11p, which is the V2X communication protocol used in Demo 4. On the other side the vehicle will receive the V2X message and forward the content of the message to the testing app which will compute the elapsed time between the request has been done to the RSU and the Vehicle module reception.

A scheme of the application workflow can be seen on Figure 41.

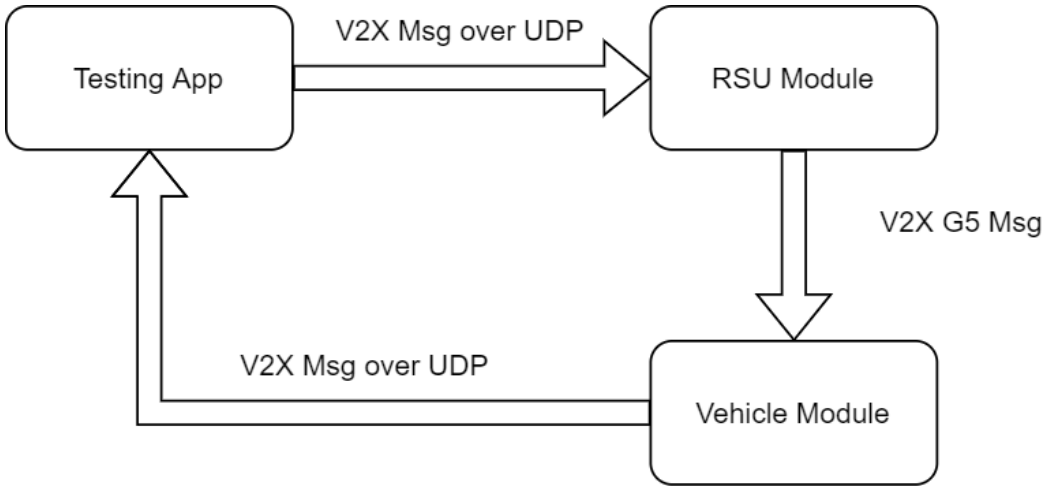

Figure 41: Latency test diagram.

With this scenario, and after 120 iterations (messages sent), the mean latency time (in milliseconds) has been 64.53ms and with the dispersion shown on Figure 42.

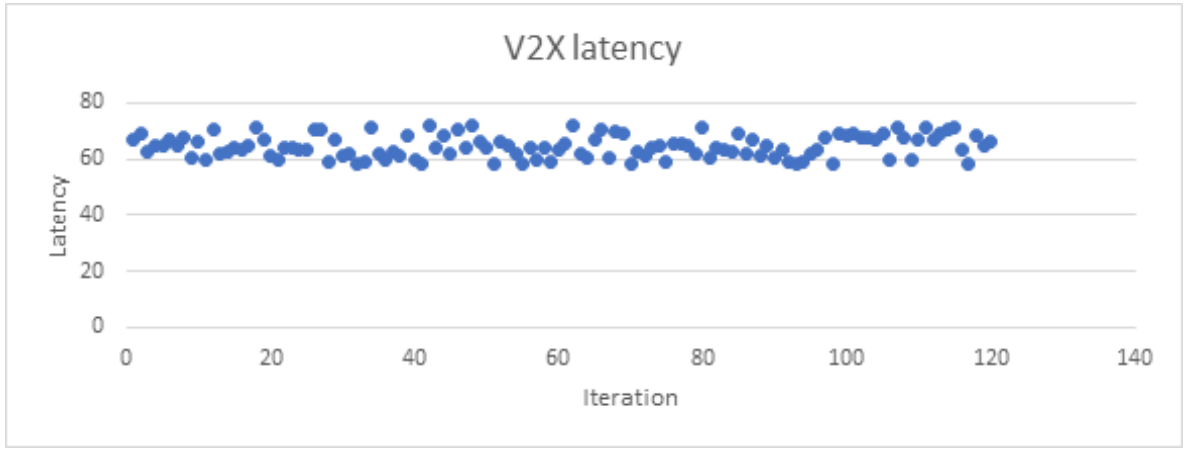

Figure 42: V2X latency diagram.

These values seem quite high, but we need to note that these results contain the time needed to send a request to the RSU module, the codification and sending of this message,

This project has received funding from the European Union's Horizon 2020 research and innovation programme under Grant Agreement 861570.

the reception and decoding of the message in the receiver and the transmission to the test app.

5.2.4 Driver warning trigger and AEB trigger verification

This system, as well as the AEB trigger, have been validated in a simulated environment (more information available in (Nikolaou, Castells, Lorente Mallada, Gragkopoulos, & Tsetsinas, D3.7 Demo 4 System for on-time warning provisions to VRUs and drivers in critical condiions update, 2022) and verified afterwards in dedicated tests. Figure 43 shows recorded signals of the AEB system on a sample test run where:

- Orange signal represents the longitudinal distance to the target [m]
- Purple signal is the ego vehicle speed [kph]
- Blue signal is the AEB activation.
- Pink signal is the Driver Warning signal.
- Sky blue signal is the computed time to collision [s]

This project has received funding from the European Union's Horizon 2020 research and innovation programme under Grant Agreement 861570.

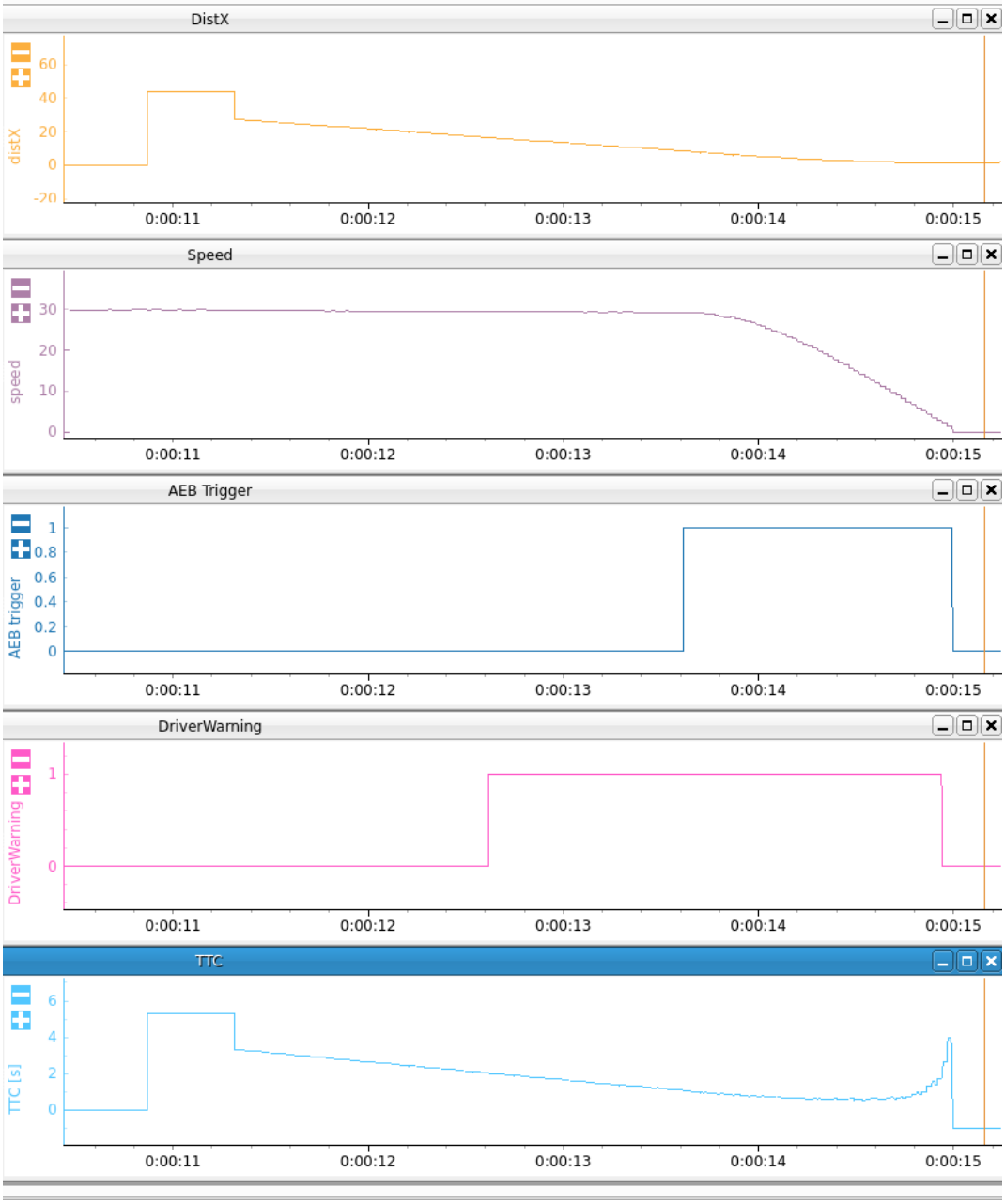

Figure 43: AEB model recording.

As the vehicle approaches the target without decelerating, the TTC decreases in a linear way. As expected, when the TTC is less than 2 seconds, the driver warning is triggered, such that the driver has the chance to manually avoid the crash.

This project has received funding from the European Union's Horizon 2020 research and innovation programme under Grant Agreement 861570.

5.2.5 V2X input to data fusion verification

The vehicle software is set up to receive detections from three different sources: a camera, radar and V2X module, as shown in Figure 44. In case V2X is not present, the baseline system is to use camera and radar.

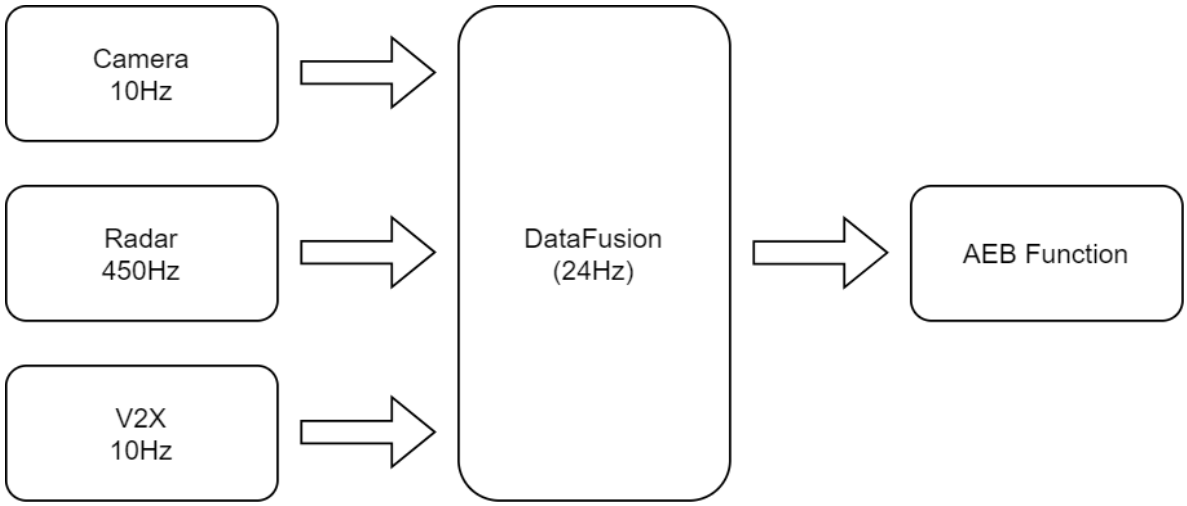

Figure 44: Vehicle module detection workflow.

Following this architecture, the verification results of the perception system (including the data fusion) are available in Deliverable (Nikolaou, Castells, Lorente Mallada, Gragkopoulos, & Tsetsinas, D3.7 Demo 4 System for on-time warning provisions to VRUs and drivers in critical condiions update, 2022).

5.2.6 Perception information's verification

For the RSU and vehicle system, the input and output of the Data Fusion is an object of the "obstacle" class which has the structure shown on Figure 45.

This obstacle class contains, for example, but not only:

- X and Y Position in local coordinates (meters from ego system)
- Obstacle size
- Obstacle speed components
- Obstacle acceleration components
- Obstacle type

With this obstacle's information and the required ego vehicle information (speed, yaw, etc.), the AEB is able to predict the trajectories and compute the TTC.

This project has received funding from the European Union's Horizon 2020 research and innovation programme under Grant Agreement 861570.

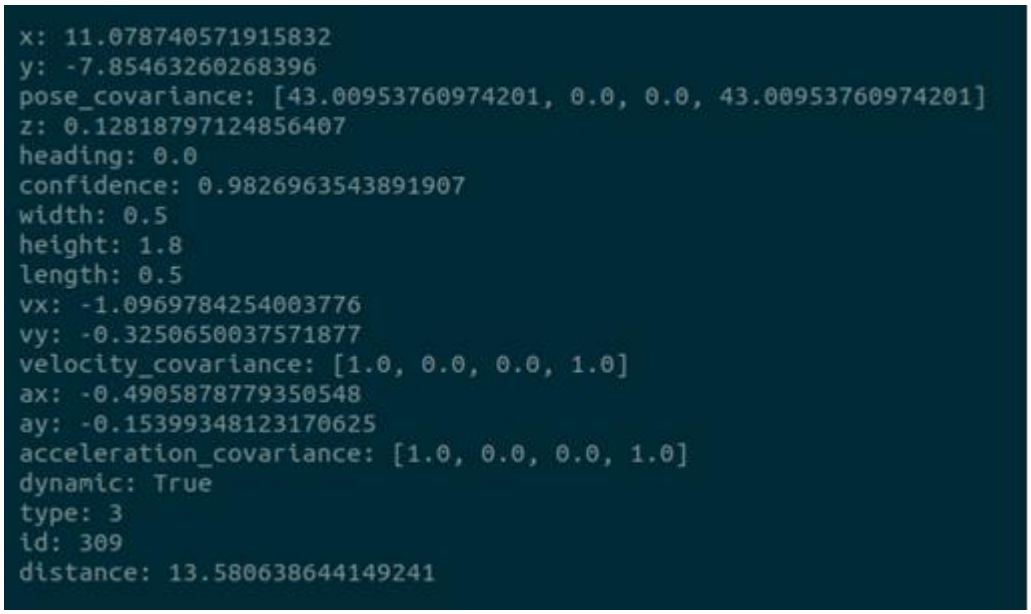

Figure 45: Obstacle message sample.

5.2.7 V2X information's verification

Minimum V2X fields to be filled are location coordinates, heading, speed and station type. RSU module system is also filling the vehicle length, width and longitudinal and lateral acceleration which are required by the Data Fusion and AEB to predict the trajectories as described in Section 5.2.6. An example decode of a real CAM message is displayed in Figure 46.

This project has received funding from the European Union's Horizon 2020 research and innovation programme under Grant Agreement 861570.

```
"cam": {
  "camParameters": {
    "basicContainer": {
      "stationType": 1,
      "referencePosition": {
        "latitude": 41.2655336,
        "longitude": 1.5211936
      }
    },
    "highFrequencyContainer": {
      "heading": {
        "headingValue": 94
      },
      "speed": {
        "speedValue": 45.6
      },
      "vehicleLength": {
        "vehicleLengthValue": 0.5
      },
      "vehicleWidth": 0.5,
      "longitudinalAcceleration": {
        "longitudinalAccelerationValue": -1.1
      },
      "lateralAcceleration": {
        "lateralAccelerationValue": -0.8
      }
    }
  }
},
"header": {
  "stationID": 385
}
```


Figure 46: Example CAM fields.

5.2.8 AEB detection rate verification

The development framework used for this project (ROS) offers a built-in tool to perform different statistical analysis of topics and messages. For validating the detection rate, this tool has been used to compute the publishing rate of messages to the data fusion output topic.

This project has received funding from the European Union's Horizon 2020 research and innovation programme under Grant Agreement 861570.

```
average rate: 24.696
        min: 0.000s max: 0.148s std dev: 0.01316s window: 336
average rate: 24.645
        min: 0.000s max: 0.148s std dev: 0.01274s window: 360
average rate: 24.586
        min: 0.000s max: 0.148s std dev: 0.01250s window: 384
average rate: 24.577
        min: 0.000s max: 0.148s std dev: 0.01222s window: 408
average rate: 24.537
        min: 0.000s max: 0.148s std dev: 0.01190s window: 432
average rate: 24.515
        min: 0.000s max: 0.148s std dev: 0.01173s window: 456
average rate: 24.494
```

Figure 47: Detection rate result.

Besides the specified requirement states that a minimum detection rate of 10Hz should be achieved, in our case we can see that this detection is done at a constant rate of 24-25Hz, which is 2.5 higher than the requirement.

5.3 Technical feasibility of Assumptions for Safety Performance Simulation

The safety performance simulation is performed in WP5 and documented in (Balint, et al., 2022) and (Kovaceva, et al., 2023). In this chapter the technical feasibility of the made assumptions are assessed. Two kinds of simulations have been performed. On the one hand, a simulation set-up where the vehicle safety system was assessed (Research Question 3), and on the other hand, a simulation set-up where the potential safety performance of a warning to the VRU was assessed (Research Question 1). The assumptions made in the simulation (Table 14) are valid for both assessment procedures.

This project has received funding from the European Union's Horizon 2020 research and innovation programme under Grant Agreement 861570.

Table 14: Technically feasibility assumptions.

Specification	Assumptions in Simulation	Achieved value in physical testing
Visibility of VRUs	All objects are visible within a range of 100m and 180° FOV	Objects are visible within a range of 100m of the RSU
VRU Classification	VRU is classified by its ground truth information	VRU has handheld device or On-Board-Unit. Classification given.
End to end Communication time	The implemented V2X information is available via ideal object information.	Information is assessed with a latency of ~60ms.
Sensor Fusion function	No sensor fusion considered, simulation just with GT object data	Sensor fusion algorithm considered.

Overall, it can be noted, that the assumptions made for the performance assessment in WP5 represent an idealised system.

5.3.1 Simulation of V2X communication: motivation and Objectives

Vulnerable Road Users (VRUs) safety presents one of the main concerns for automated mobility. Due to the lack of adequate protection and the inability to react in critical circumstances, road users, mostly VRUs, are exposed to a high risk of being involved in an accident. Advanced Driving Assistance Systems (ADAS) are intended to increase safety for driver and other road users. ADAS technologies present various solutions. Among them are safety measures relying on sensor perception and active safety based on cooperative intelligent transportation systems (C-ITS) only. Using these systems, vehicles will be able to collect information from different sources. The automotive industry has invested heavily in developing various countermeasures for VRU safety issues. A broad range of sensors such as camera, LIDAR and radar can be used for perception. Compared to other sensors, cameras are suitable for VRU detection because they provide the most detailed information about the vehicle environment. Interpreting this visual information requires complex algorithms capable of detecting objects in different conditions (e.g., day and night lighting conditions, weather conditions, and complex backgrounds).

This project has received funding from the European Union's Horizon 2020 research and innovation programme under Grant Agreement 861570.

To improve VRU detection performance, V2X technologies can also be considered as an alternative or complement that allows a wide range of road users to interact by exchanging status and location information using advanced communication technologies.

Enabling the interconnection between VRUs, drivers, and infrastructure systems is one innovative approach for improving VRU safety. C-ITS provides such functionality by allowing VRU information (location and context information) to be shared with other road users via communication technologies.

On the one hand, whenever connected, VRUs can broadcast their awareness information (VRU Awareness messages: VAM (3GPP)), received either by vehicles that are thus directly warned, or via the RSU (V2I) and/or the 4G/5G network (V2N), that will in turn warn the vehicles.

On the other hand, the presence of the VRU (connected or not) can be detected by a Road Side Unit (RSU) or by a vehicle both using their on-board sensors (camera, lidar). In this latter case, even when the VRU is not itself connected, information from vehicles' sensors is wirelessly sent to the network (V2N), or to the RSU (V2I), or possibly to both, and is further processed (fused) to improve the VRU detection probability.

Our goal is to propose a V2X-based safety solution that enables timely warning provisions. We will focus on two main scenarios, the first one similar to Demo 4 08 & 09 "bicycle crossing, without visibility", the second one to Demo 4 01 & 02 "pedestrian crossing, without visibility" (Nikolaou, Castells, Lorente Mallada, Gragkopoulos, & Tsetsinas, D3.4 Demo 4 System for on-time warning provisions to VRUs and drivers in critical conditions, 2021). In both cases, we focus on the driver reaction: we try to answer, at least partially, to the Research Question RQ2 (Nikolaou, Castells, Lorente Mallada, Gragkopoulos, & Tsetsinas, D3.7 Demo 4 System for on-time warning provisions to VRUs and drivers in critical condiions update, 2022) and (Kovaceva, et al., 2023)):

RQ 2: "What is the safety benefit of a VRU C-ITS warning system on vehicle drivers in supporting them to mitigate safety-critical events with connected and non-connected VRUs, triggered by a radio signal based (OBU, RSU, VRU-smart device) communication and detection system, in terms of KSI injury reduction on EU level in 2025 compared to the 2016 numbers for Car to VRU collisions on urban roads?"

We first consider the "bicycle" use-case, featuring a crossroad, with a vehicle coming on one branch, and a bicycle on the other, with no visibility, due to the buildings on each side of the road. We do not make a difference between bicycle coming from the right side or the left side, since the simulator generates random trajectories for cars and VRUs. Simulation results are averaged over all situations. Nonetheless, this scenario is similar to Demo 4 08 & 09 "bicycle crossing, no visibility. Both VRU and vehicle are assumed to be connected. However, our focus is on the driver reaction (even though the bicycle is also connected, we assume that only the driver reacts to an alarm triggered by reception of the bicycle VAMs). Our goal is to evaluate the probability of message reception up to the last moment when the driver can still avoid the accident. In this aim, we compare three different V2X technologies, in a representative urban scenario.

This project has received funding from the European Union's Horizon 2020 research and innovation programme under Grant Agreement 861570.

The second part of our study deals with the « pedestrian » use case, in a non-visibility situation. This scenario is similar to Demo 4 01 & 02 “pedestrian crossing, without visibility”. The pedestrian is not necessarily connected. In this latter case, his presence is detected via a depth camera, using an Artificial Intelligence image processing. The camera is either co-located with an RSU, or is on-board of a car in visibility of the pedestrian. In the first case, the RSU will broadcast back the information about the pedestrian location to all cars, including of course those in non-visibility of the pedestrian. If e.g., there is no RSU, then a car might detect the pedestrian, and (here it is a different assumption as in Demo 4), the information about the pedestrian is sent to the main 4G/5G network (we call this “centralized architecture”), which will broadcast it back to all vehicles, including those in non-visibility. Lastly, a “hybrid architecture” is envisaged, where both RSU and 4G/5G networks are involved. The RSU detects the pedestrian and broadcasts this information to all vehicles (as before), But in addition, each vehicle fuses this received information with its own perception, and sends the resulting information to the main network, which broadcasts it back to all vehicles. We compare all these approaches by simulations, including the artificial intelligence pedestrian recognition performance, via a scenario provided by a 3D real-time simulation module called 4DV–SIM[1] commercialized by 4D Virtualize©.

5.3.2 System Level Simulation Framework

Our simulation framework is composed of two blocks:.

- The first block models connected nodes on a given road topology.
- The second block calculates the statistics of correct received packets via V2X

The V2X connectivity modules (second block) follow a cross-layer simulation approach between the physical and higher layers to exploit the mobility traces from the first block. The system level simulator then includes specific data traffic, propagation channel models and V2X-equipped nodes according to the architecture of each scenario

The second block simulates VRU detection based on V2X technologies. All nodes (e.g. vehicles or VRUs) disseminate information about their location. All vehicles and VRUs are equipped with V2X technologies (e.g. IEEE 802.11 p, C-V2X, 802.11bd, see Appendix A for these standards description or 4G/5G). For each used technology, a full protocol stack from application layer to physical layer is implemented. Implementation is on ns-3, a discrete event network simulator for Internet1 4DV – SIMULATOR, systems. ns-3 is a free and open source software, licensed under the GNU GPLv2, and maintained by a worldwide community

https://www.4d-virtualiz.com/en/robotics-simulator/4DV – SIMULATOR.

This project has received funding from the European Union’s Horizon 2020 research and innovation programme under Grant Agreement 861570.

The first module models the traffic road toplology using either SUMO traffic mobility simulator (Alvarez Lopez, et al., 2018) (bicycle use case) that gives mobility traces compatible with ns-3 network simulator, or 4DV-SIM traces (Pedestrian case). As shown in Figure 48, a Python parser is developed to generate ns-3 compatible mobility traces. Its role is to convert the XML files of SUMO to the TCL ns-3 mobility format

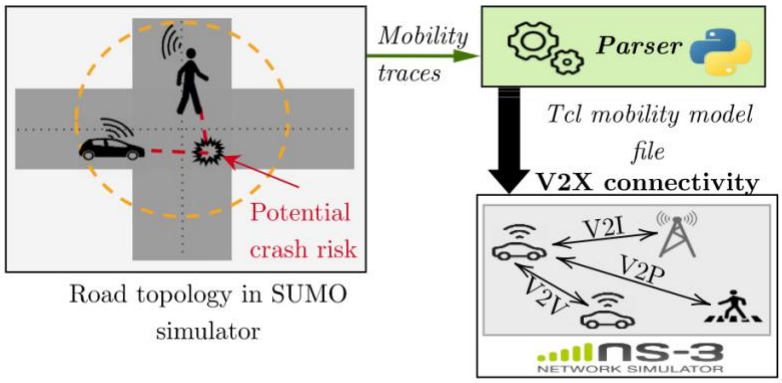

Figure 48: System level simulation architecture for the “bicycle” use case

For the “pedestrian” use case, the Road topology of Figure 48 is replaced by the scenario of Figure 54.

5.3.3 Evaluation Methodology and Assumptions

In this section, we introduce our evaluation methodology and describe the chosen scenario and system-level simulation assumptions. The obtained performance results are then analysed. For this study, we define three key performance indicators:

- **Packet reception probability P**: it is calculated as the success rate between the received packets and the sent packets over 500 ms time windows. P is given as follows:
  - P(t) = (number of successful packet P per transmission period)/ number of transmitted packets per transmission period.
- **Remaining Duration for Crash Avoidance (RDCA):** it is defined as the remaining duration before reaching the Crash Avoidance Time (CAT) threshold, defined as follows; it represents the last instant when the driver is still able to react and stop his car to avoid the crash. RDCA is therefore computed as the difference between the CAT threshold and the first time the VRU is correctly detected.

This project has received funding from the European Union’s Horizon 2020 research and innovation programme under Grant Agreement 861570.

- **Probability of driver awareness (PDA):** It is defined as the probability that the driver of the vehicle crossing the path of the pedestrian will receive at least one message/packet indicating the presence of the pedestrian.

In Subsection 5.3.4, we focus on the comparison of different technologies for a decentralized architecture in the case of an equipped VRU scenario. In this case, we use the packet reception probability and the RDCA metrics, since we want to study the impact of each technology on the reception of VRU notification messages. To this end, the packet reception probability allows us to track packet loss and conclude on the performance of each technology under LOS and NLOS channel conditions.

In Subsection 5.3.5 we focus more on the network architecture level, where we compare different VRU detection possibilities under decentralized, centralized, and hybrid network architecture. To this end, we define the driver awareness probability, which is a metric to properly quantify system-level performance. Here, our concern is to quantify the effectiveness of the V2X network architecture for VRU detection in different scenarios, compared to basic sensors (e.g., cameras). And in more detail to observe the possible gain in safety of vulnerable road users using V2X networks.

5.3.4 Scenario 1: Benefits of V2P/P2V for Cyclists in High Crash Risk Situation under Urban Intersection

5.3.4.1 Scenario Description

In this study, we evaluate the benefits of equipping VRUs with V2X radios. A hazardous situation where a cyclist is exposed to the risk of colliding with an oncoming vehicle in an urban intersection is considered. Performance results are based on a system-level simulation consisting of two components: SUMO and ns-3 simulators. Our scenario assumes that VRUs and vehicles are equipped with a V2X radio interface able to periodically broadcast awareness messages. Three V2X technologies, C-V2X, IEEE 802.11p, and IEEE 802.11bd are compared and analysed. A realistic traffic environment is considered where 63 nodes are simulated in a 400 m intersection: 30% of the nodes are cyclists and the rest of the nodes are light-duty vehicles.

This project has received funding from the European Union's Horizon 2020 research and innovation programme under Grant Agreement 861570.

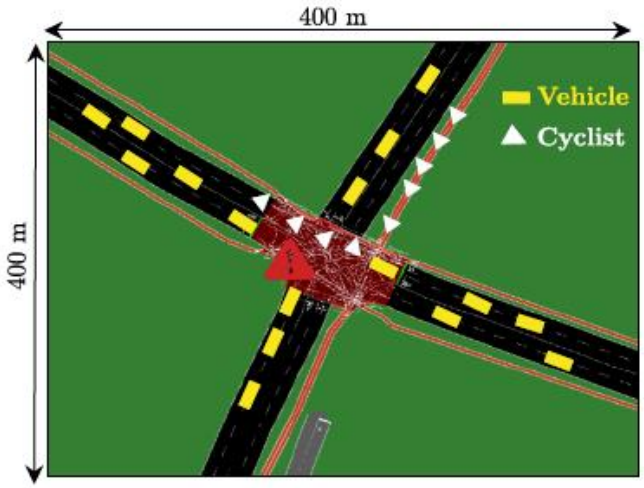

Figure 49: Simulation topology.

SUMO is used to generate a mobility model in a typical urban intersection. These mobility traces are then converted to a format called Tool Command Language (TCL) that feeds ns-3 communication models. A full protocol stack pattern of V2X communication technologies is simulated within ns-3. As shown in Figure 49: Simulation topology. we considered a real intersection of two main streets (Quai du Commerce and Pont Robert Schuman) located in the city of Lyon, France, which forms an area of 400m X 400m. Vehicles can navigate on two lanes and both directions. As for the cyclists, they can either ride on a cycle lane or on the same lane as the vehicles. The simulated vehicles can reach a maximum speed of 30 km/h, while the cyclists can reach 20 km/h. As specified by 3GPP (3GPP TR 37.885, 2018), we assume that a VRU is capable of broadcasting VAMs including its location and speed. Vehicles are also broadcasting awareness messages (CAM). Vehicles and cyclists can receive and decode these messages. The message transmission period, T, is assumed to be equal to 100 ms.

Table 15: Simulation parameters

Traffic mobility settings	
Number of V2X equipped nodes	63
Maximum vehicles speed (km/h)	30
Nominal deceleration (m/s^2)	4.5
Maximum VRU speed (km/h)	20
Simulation length (s)	26
Network communication settings	
Tx power (dBm)	23
Message size (Bytes)	300
Channel bandwidth (MHz)	10
Gross data rate (Mbps)	≈ 6
Transmission period T (ms)	100
Channel model	LOS|WINNER+B1
Number of simulation trials	100

*

This project has received funding from the European Union's Horizon 2020 research and innovation programme under Grant Agreement 861570.

Traffic mobility settings	
Number of V2X equipped nodes	63
Maximum vehicles speed (km/h)	30
Maximum VRU speed (km/h)	20
Simulation length (s)	26
Network communication settings	
Communication mode	V2V/V2P
Tx power (dBm)	23
Message size (Bytes)	300
Channel bandwidth (MHz)	10
Radio band (GHz)	5.9
Gross data rate (Mbps)	≈ 6
Transmission period *T* (ms)	100
Channel model	WINNER+B1

We can note that as well the nominal deceleration (4.5m/s2), the maximum VRU speed (20 km/h) and the maximum vehicle speed (30km/h) are all in line with respectively the maximum deceleration (9km/h) ((Kovaceva, et al., 2023) section 1.2.1.3), the VRU speed (20km/h) and the vehicle speed range (15-30 km/h). These latter two figures are those of Table 15 in (Kovaceva, et al., 2023).

We used the C-V2X sidelink (PC 5 - Mode 4) module introduced in (Eckermann, M., & Wietfeld, 2019), which is based on the Device-To-Device (D2D) communication simulation model developed and validated in (Rouli, Cintron, Mosbah, & A., 2017). PC 5 mode 4: C-V2X sidelink operates in the 5.9 GHz unlicensed band. In this standard, each user (i.e., a connected vehicle or a static RSU) can transmit packets every 100 subframes (i.e., 10 packets per second) or in multiples of 100 sub-frames with a minimum of 1 packet per second. A fixed Modulation Coding Scheme (MCS) was chosen based on a typical PC 5 mode 4 communication technology configuration and given in Table 16. In terms of MAC, the vehicles select their radio resources following the Sensing-based Semi-Persistent Scheduling (SB-SPS) algorithm (ETSI TS 36.321, 2018).

For IEEE 802.11p and 802.11bd technologies, we used the ns-3 WIFI module, specifying for each standard its specific parameters. This module uses the NIST error model as the OFDM frame error rate model, which was evaluated in (Pei, Gugangyu, & Henderson, 2020).

The impact of the channel propagation conditions on the communication performance and its influence in accident risk reduction is considered. Two propagation conditions are thus evaluated: Line-Of-Sight (LOS) and Non-line-of-sight (NLOS). LOS occurs when vehicles and VRUs drive in very open environments without large buildings and obstacles. LOS

This project has received funding from the European Union's Horizon 2020 research and innovation programme under Grant Agreement 861570.

conditions are optimistic in an urban environment and give a best-case performance scenario. NLOS occurs when communications are obstructed and provides more realistic performance estimations. For the LOS use case, we considered the channel conditions based on Appendix B 7.4. For the NLOS case, we used the WINNER+B1 channel model (3GPP TR 37.885, 2018), which allows transitions between LOS and NLOS propagation conditions based on the calculation of the LOS probability (Meinila, 2007) as detailed in Annex B.

5.3.4.2 Analysis of the Results

As performance indicators, we consider packet reception probability and RDCA, as we are interested in comparing different V2X adhoc technologies at the link granularity level. The packet reception probability enables to track packet loss in each sending period, which facilitates performance comparison.

According to our particular simulation timeline, CAT is set to time t = 20.65 seconds. This value is calculated from the crash time, which is supposed to occur at time t = 24s (i.e. in accordance with the SUMO accident risk log data) minus the reaction time and the braking time of the car. Reaction time is set to 1.5s and stopping time to 1.85s as the results from the division of the car maximum speed (8.3 m/s) by its nominal deceleration (4.5 m/s2).

The RDCA is therefore calculated as the difference between the CAT threshold, and the first time the pedestrian is correctly detected

To better understand a key element of our VRU scenario, we eventually analyse performance in a crash risk situation. To this extent, the SUMO mobility model has been intentionally modified to allow collisions between vehicles and cyclists. Packet reception performance is then analysed over time from the start of the simulation until the virtual crash. Figure 50 gives the packet reception probability over time of the VAM transmitted by the cyclist and received by the vehicle in a crash risk situation for LOS and WINNER+B1 channel propagation conditions. Two important event instants are identified in Figure 50: the crash time (i.e. red dashed line) that occurs at time 24s and the CAT threshold (i.e. the black dashed line).

This project has received funding from the European Union's Horizon 2020 research and innovation programme under Grant Agreement 861570.

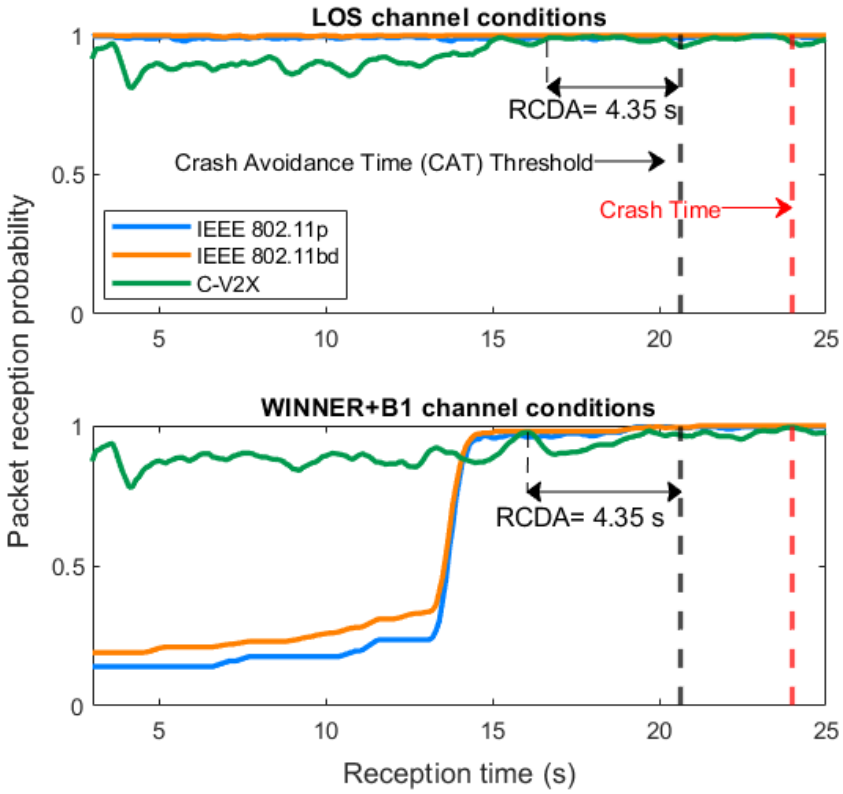

Figure 50: Packet reception probability for vehicles in a crash risk situation.

As shown in Figure 50, we measure the packet reception probability that consists to track the packet loss over a sending period of 100 ms. We compute this probability over 500 ms time windows under LOS and Winner+B1 channel conditions. Under LOS channel conditions, the probability of receiving the packet 15 seconds before the CAT is very close to 1 for both IEEE 802.11p and 802.11bd. For C-V2X, performance is consistently increasing as the distance between vehicle and cyclist is reduced. However, it seems to exhibit a pseudo-periodic behaviour, certainly induced by the periodicity of the Sensing-based Semi-Persistent Scheduling (SPS) algorithm. When considering the 5s before the CAT threshold, the packet reception probability is equal to 0.998, which can reliably guarantee collision avoidance (Boban, Kousaridas, Manolakis, & Eichinger, 2018) (5GAA).

Despite the loss of a few packets during the sending period, we note an RDCA of 4.35 s, which is sufficient to act before the crash occurs.

When more severe NLOS conditions are considered, the behaviour of the reception probability as a function of time is very different between both families of standards. For C-V2X, a degradation of the probability is consistently present along the time window of observation. An average reception probability of around 0.93 in the last 5s before CAT is measured. On the other hand, for IEEE 802.11bd and 802.11p, the probability of reception is significantly degraded when vehicle and cyclist are further apart, while when considering the last 5 s before CAT, it is consistently above 0.95 and equal on average to 0.97. This behaviour is particularly relevant to the VRU scenario and suggests that although a

This project has received funding from the European Union's Horizon 2020 research and innovation programme under Grant Agreement 861570.

significant amount of packets are lost when propagation conditions are severe, the packet reception probability is very high as the crash is approaching, so that RDCA can be again evaluated at 4,35s. This confirms the safety benefits of V2X equipped VRUs.

5.3.5 Scenario 2: Pedestrian in Blind Intersection, Performance Comparison of Connectivity- based VRU perception and Sensor-based VRU perception Cases

In this section, we describe V2X-system architectures based on both sensors' perception and V2X connectivity.

5.3.5.1 VRU Safety Systems Using Both V2X Connectivity and Perception via Optical Sensors

A. Optical sensors-based perception

Optical sensors are some of the key building blocks of Advanced Driver Assistance Systems (ADAS). The raw data output from these sensors requires efficient real-time processing. We first introduce here one of the most popular real-time object detection algorithms, called You Only Look Once (YOLO) (Redmon, Divvala, Girshick, & Farhadi, 2016). Based on regression, YOLO can typically predict the classes of detected objects, as well as their bounding boxes, over the whole image in one single run of the algorithm. YOLO employs a Convolutional Neutral Network (CNN) to detect objects in real-time, which is a widely used architecture in the fields of image recognition, image classification, object detection, etc. It can thus process any input image according to certain a priori classes (e.g., pedestrians, cyclists, cars...). The bounding box coordinates (i.e., relative to their cell coordinates) can hence be predicted, each containing the object's label and the probability of the object to be present in the cell. Each box is then associated with a confidence score. The latter reflects how likely it is that the box contains an object and how accurate is the boundary box. A class confidence score is then deduced for each prediction box, which is computed as the product between the box confidence score and the conditional class probability. The latter represents the probability that the object belongs to a certain class (e.g., pedestrian), given the actual presence of that object.

B. V2X-based System Architectures

1) Decentralized architectures: Two Use Cases (UC) are considered based on (ETSI TS 103 300-2 V2.1.1, 2020), which both rely on decentralized communication architectures (i.e., in contrast to network-based architectures).

The first scenario, which is referred to as UC-C1, relies on P2V connectivity (See Figure 51-Left). Both vehicle and pedestrian are equipped with a C-V2X sidelink radio interface (a.k.a., PC5 air interface - Mode 4). We then assume that the pedestrian intentionally shares his location in his surroundings (i.e., typically based on GPS), by periodically broadcasting VRU VAMs. However, as privacy issues are among the main factors that may prevent VRUs from

This project has received funding from the European Union's Horizon 2020 research and innovation programme under Grant Agreement 861570.

accepting the V2X technology, other alternative infrastructure-based architectures also need to be considered.

In the second use case, depicted as UC-D2, we assume that the pedestrian is not equipped but purely passive (See Figure 51- Right). It is then detected by processing data from camera sensors (See e.g., Subsection A), which are co-located with an RSU. Then, detection events are encapsulated in Collective Perception Message (CPM) messages, which are broadcast over I2V links to other connected road users.

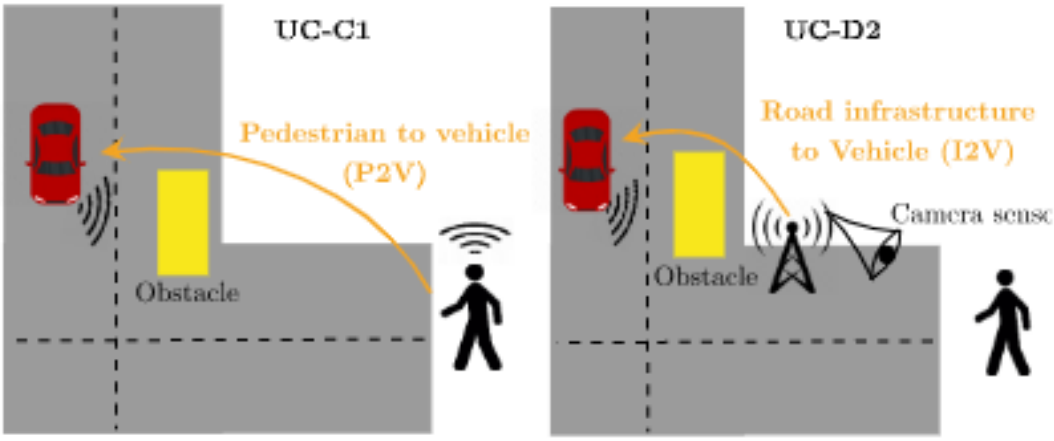

Figure 51: P2V and I2V communication architectures.

2) Centralized Architecture: Based on V2N connectivity and a centralized architecture, we also consider a third canonical use case, denoted as UC-E2 (See Figure 52. More particularly, we consider V2X communications over both Uplink (UL) and Downlink (DL) transmissions using 5G New Radio (5G-NR) Non-Standalone (NSA) deployment. As shown in Figure 52, a non-equipped (i.e., passive) pedestrian can still be detected by surrounding vehicles endowed with optical sensors and on-board processing capabilities. If these vehicles are also equipped with a 5G-NR modem, they will be able to transmit a CPM in UL to a Multi-Access Edge Computing (MEC) server (i.e., as fusion centre), notifying the presence of a pedestrian. The safety application hosted in the MEC server then merges all CPM messages coming from the different vehicles having detected the pedestrian in order to notify the presence of the pedestrian to other vehicles, through the DL transmission of a merged CPM (Mouawad & Mannoni, 2021)

3) Hybrid Architecture: The idea is to use the cooperation between the direct I2V link and a V2N-based architecture to take advantage of the redundancy of information in the distribution of the warning information. Indeed, when the RSU perceives the pedestrian in danger thanks to the on-board camera sensors, it transmits the information to vehicles in its surroundings by direct V2X communication via the I2V link. Each vehicle receives the information from the RSU, then transmits a complete encapsulated CPM message of its own perception and that of the RSU to the MEC fusion centre via the uplink. Once received by the MEC, the messages are merged and sent to the vehicle on the obstructed side via the downlink.

This project has received funding from the European Union's Horizon 2020 research and innovation programme under Grant Agreement 861570.

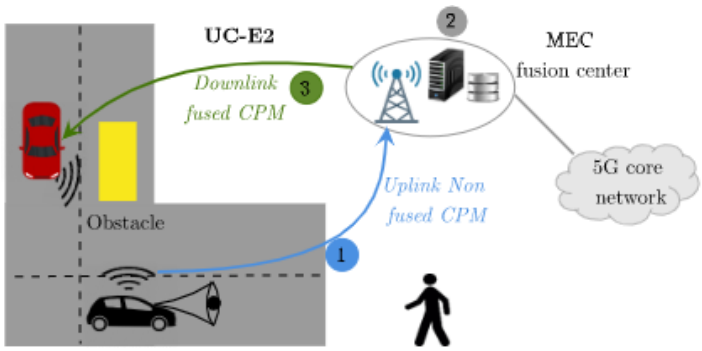

Figure 52: V2N-based architecture, exploiting the on-board sensors detection encapsulated in the CPMs and sent on the uplink, which once received by the MEC are then merged and sent to the vehicle on the obstructed side over the downlink.

5.3.5.2 Simulation Framework and Assumptions

In order to analyse the performance of the previous system architectures, we have developed a simulation framework based on three main building blocks: mobility, pedestrian detection and V2X connectivity modules.

First, a realistic accident scene involving a pedestrian VRU at an urban intersection has been modelled by means of a real-time 3D and Hardware-In-the- Loop simulation platform called 4DV–SIM, which can emulate complex ADAS systems in a 3D multi-sensor virtual environment similar to a real operational use case. The simulator includes various pre-positioned cameras, from which the user can choose. Mobility traces of all the entities involved in the accident scene (incl. all pedestrians and all vehicles) are extracted from the generated simulation dataset, along with realistic camera sensor features (e.g. field of view, pitch and frequency, etc.). Based on these traces, object detection is then conducted using the YOLO algorithm, as described in Subsection A. These mobility traces feed the ns-3 V2X connectivity modules described in Subsection B.

A. Pedestrian Detection Module

We assume that all vehicles are equipped with optical sensors, and more specifically with standard and depth cameras. We assume that the refreshment frequency of both cameras equals 10 Hz. An image processing unit is implemented using the YOLOV3 (Redmon & Farhadi, YOLOv3: An Incremental Improvement, 2018) real-time object detection algorithm, which has been specifically developed for VRUs perception. A pre-trained model on the Microsoft Common Objects in Context (MS-COCO) dataset (Lin, 2014) has then been used to predict the bounding boxes and recognize pedestrians. After the training, during the online phase, YOLOV3 thus analyses the optical sensor traces produced by 4DV–SIM. Based on this analysis, a pedestrian detection probability is then calculated. Finally, as shown in Figure 53, a mapping step between each pedestrian detection event and the depth camera information is added, relying on the centroid of the corresponding bounding box. After

This project has received funding from the European Union's Horizon 2020 research and innovation programme under Grant Agreement 861570.

matching the two information, the depth data then provides the distance at which the pedestrian has been detected.

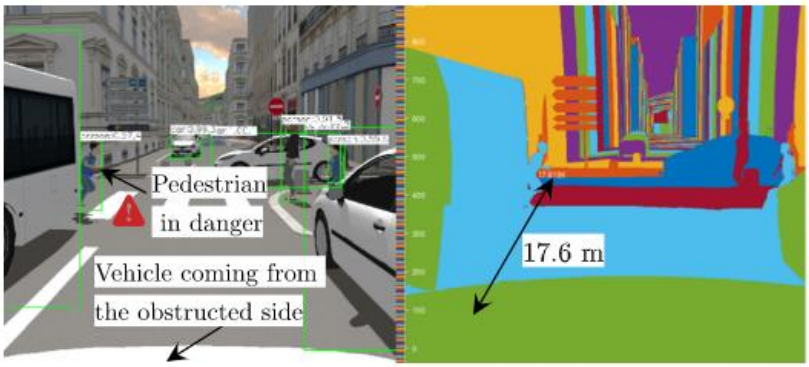

Figure 53: Subjective vision from the front standard camera of a vehicle driving towards the test intersection, along with YOLO detection results (top) and corresponding distance mapping by the depth camera (bottom), with a pedestrian VRU in danger (partly obstructed from the vehicle by the bus parked on the left).

B. V2X Connectivity Module

1) We recall that PC 5 mode 4: C-V2X sidelink operates in the 5.9 GHz unlicensed band. In this standard, each user (i.e., a connected vehicle or a static RSU) can transmit packets every 100 subframes (i.e., 10 packets per second) or in multiples of 100 sub-frames with a minimum of 1 packet per second. For propagation, the conditional WINNER B1 path loss model parameters have been used, while the channel status is identified in a deterministic manner as in (Guizar, Mannoni, Poli, Denis, & Berg, 2020) according to the scene. In other words, for each RX/TX pair, we check if the direct path intercepts buildings or intersection corners. If so, the Non-Line-Of-Sight (NLOS) link condition is considered, and the corresponding channel parameters accordingly. If a car is located between the RX/TX pair, the Obstructed Line-Of-Sight (OLOS) link condition is then considered. Otherwise, the link condition is Line-Of-Sight (LOS). In our simulations, we assume in first approximation that the RSU is systematically experiencing LOS link conditions with respect to all the vehicles involved in the scene, given that it is located at a height of 5m.

2) 5G-NR: The 5G-NR simulation framework incorporates fundamental PHY-MAC New Radio (NR) features aligned with 3GPP Release-15. We assume that our 5G communication system operates in the mid-band frequency of 3.5 GHz, as it is the common spectrum band in Europe (ETSI TS 103 300-2 V2.1.1, 2020). With regards to channel models, the simulator implements a set of 3GPP-compliant scenarios supporting urban and highway use cases. More specifically, we use here the 3GPP Urban Macro Cell (UMa) channel model defined in (ETSI, 2018) assuming that the heights of the gNodeB and User Equipments (UEs) are respectively equal to 25 m and 1.5 m, following the 3GPP guidelines (ETSI, 2018). An adaptive MCS selection is adopted depending on SINR (Patriciello, Lagen, Bojovic, & Giupponi). A Time Division Duplex (TDD) duplexing mode is used, where a single UE is

This project has received funding from the European Union's Horizon 2020 research and innovation programme under Grant Agreement 861570.

scheduled per Transmission Time Interval (TTI) in a Round Robin (RR) fashion. Table 16 summarizes the used simulation parameters.

Table 16: Main simulation parameters.

Common settings	
Number of V2X equipped nodes	18
Simulation length (s)	26
CPM periodic sending frequency	10
CPM size (Bytes)	Depending on the number of obstacles detected (from 100 to 30)
C-V2X mode 4 settings	
Tx power (dBm)	23
Number of total resource block	20 (bandwidth = 4 MHz)
MCS	10
Propagation model	WINNER+B1
5G-NR settings	
Antenna modelling	Isotropic model
gNodeB/UE antenna elements	4x8|4x2
Bandwidth (MHz)	100
MCS	Adaptive (between 0 and 28)
Channel access scheme	TDMA
Scheduler policy	Round Robin
Numerology	2

5.3.5.3 Performance Analysis

5.3.5.3.1 Tested Scenario and Performance Indicators

In this section, we assess the performance of the distinct V2X-based system architecture options introduced in Section B. We also evaluate a hybrid multi-technology approach, which consists in exploiting both I2V and V2N connectivity for better information redundancy. For this purpose, we consider the canonical accident scenario illustrated in Figure 54 (4DV-SIM) where a pedestrian unexpectedly crosses the path of an incoming vehicle whose direct perception is obstructed by a parked bus. Even more specifically, we are interested in the way the warning information (upon detection of the pedestrian) is distributed to the

This project has received funding from the European Union's Horizon 2020 research and innovation programme under Grant Agreement 861570.

approaching vehicle, prior to the accident. For the scenarios based on I2V and V2N connectivity, the pedestrian detection is performed using optical sensors, while in the P2V scenario, the pedestrian directly broadcasts his own GPS position to inform about his presence.

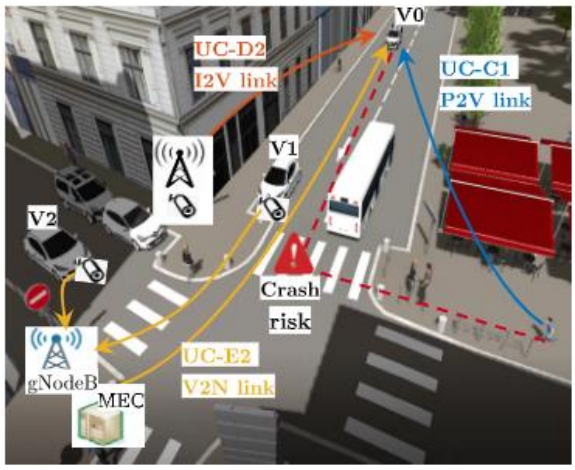

Figure 54: Simulated canonical (pre-) accident scenario.

For this evaluation, we considered two key performance indicators as follows:

RDCA and Probability of driver Awareness (PDA). According to our particular simulation timeline, CAT is set to time t=17 seconds, minus the reaction time of 1.5 seconds and the breaking delay of 1.18 seconds.

As mentioned earlier, we introduced the probability of driver awareness to quantify the effectiveness of each architecture used in VRU detection. The PDA indicates whether the driver will receive at least one notification message about the presence of a VRU on the road. PDA is then given by:

$$P_{DA} = 1 - \left(1 - P_{SuccessPerEpoch}\right)^{\frac{T}{t_p}}$$

where T is the total duration of a time window opened upon detection of the pedestrian and t_p is the transmission period of V2X packets within this time window. $P_{SuccessPerEpoch}$ is the probability of receiving a message given the presence of a pedestrian per transmission attempt. It therefore depends on the correct detection of the pedestrian in danger with probability P_D, as determined by processing the on-board sensors outputs (e.g., using the YOLO algorithm for unequipped VRU or GPS information directly in case of equipped VRU). For I2V and P2V for instance, $P_{SucessPerEpoch} = P_R * P_D$, where P_R is directly measured as the successful packet reception ratio per transmission attempt, (or so-called epoch) respectively for the CPMs and VAMs that must be received on time at the vehicle concerned by the accident situation (i.e. V_0 as shown in Figure 54). For V2N however, the successful reception per transmission attempt $P_{SucessPerEpoch}$ is conditioned by two events: First, the preliminary effective obstacle detection at one assisting vehicle i at least (with i =1….,n), with probability P_{D_i}, followed by the successful reception of the associated UL CPM from that

This project has received funding from the European Union's Horizon 2020 research and innovation programme under Grant Agreement 861570.

assisting car on the MEC side, with probability P_{ul_i} . Second, the DL successful reception of the merged CPM from the MEC at the V_0 vehicle. $P_{SucessPerEpoch}$ is therefore given by:

$$P_{SucessPerEpoch} = \sum_{i=1}^{n}(P_{ul_i} * P_{D_i}) * P_{dl},$$

where n is the number of assisting sensors-enabled vehicles (In our case n=2, referring to the vehicles V_1 and V_2 in Figure 54 which send their CPMs to the MEC fusion centre.

5.3.5.3.2 Simulation results

Figure 55 shows results of the overall driver awareness probability for different V2X-based system architectures, including the impact of sensors accuracy. We thus note that all V2X-based systems converge to a driver awareness probability of 0.99, with different RDCA, with approximately 9, 6 and 1 seconds remaining before reaching the CAT threshold for V2P, I2V and V2N respectively. This difference in RDCA can be explained by the fact that the pedestrian detection is better anticipated by the GPS-based P2V system, even when positioning errors exist. We note that the hybrid and I2V link graphs are overlaid, as the RSU provides better perception in comparison to the vehicles. Second, due to the topological nature of our scenario, the RSU camera detects the pedestrian prior to other vehicles, whose perception is used in the V2N system. The V2N case is dominated by the performance of optical sensors detection from assisting vehicles, which is more limited (again, due to both reduced and obstructed fields of view, when compared to that of the RSU). In addition, the RSU optical sensor is better positioned in height, which also contributes to a better detection performance, as already confirmed by the results of Figure 55.

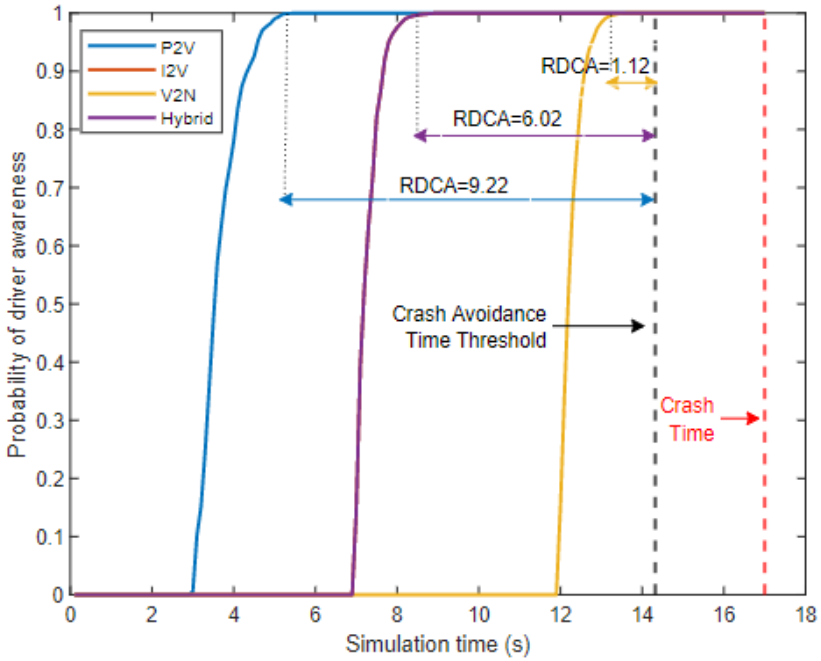

Figure 55: Performance of driver awareness.

This project has received funding from the European Union's Horizon 2020 research and innovation programme under Grant Agreement 861570.

We have investigated and discussed different V2X-based system architectures for the proactive safety of VRUs at urban intersections, considering on-board sensors detection. For this purpose, a realistic accident scene has been simulated, with a pedestrian crossing a road while being hidden from an approaching vehicle by a massive obstacle. In this context, we have illustrated and evaluated the impact of both the underlying C-V2X sidelink and 5G-NR radio technologies (along with the associated network topology options), as well as the quality of sensors detection. Our results highlight clear benefits of this V2X-based systems for improving VRUs safety in the sense of an earlier prevention of critical pre-crash situations, achieving a typical probability of driver awareness of around 1, with different remaining duration before the reaching the crash avoidance time threshold. Our results show the advantages of V2X-based systems over non-V2X equipped systems based on standalone on-board sensors. In this study, we considered a canonical VRU accident use case simulated under a full stack simulator supporting optical sensors, mobility, and V2X connectivity models.

5.3.6 Conclusion

In this deliverable, we have presented two main studies on vulnerable road user detection using V2X systems and perception sensors. These two studies cover both link and system level performance. They both focus primarily on investigating the effectiveness of V2X systems in providing early warnings to human drivers (or AEB) thus preventing accidents involving VRUs, and more specifically, are an extension of Demo 4. This extension complements demo 4 in terms of traffic density, which cannot be implemented in the real field trials. Indeed, in the first study, we simulated an urban intersection with a realistic traffic density involving VRUs and vehicles. In addition, different channel conditions, such as LOS and NLOS were also evaluated, using realsitic propagation channel models..

The first study is dedicated to equipped VRUs, and compares the different existing V2X Adhoc technologies such as IEEE 802.11p, C-V2X, and 802.11bd. We studied their impact on the reception of notifications from VRUs under different channel conditions. This study showed that equipping a VRU with a V2X radio interface enhances VRU safety and significantly increases VRU awareness compared to baseline systems (i.e., non-equipped VRU). The results also showed that when VRUs are equipped with V2X technologies, the driver can be alerted with approximately 4 s remaining duration before the crash avoidance threshold, which is sufficient to take action and avoid the crash [5GAA]. We also showed that C-V2X technology slightly outperforms 802.11 based technologies under severe channel conditions, due to its better physical link budget (Karoui, Mannoni, Denis, & Mayrargue, 2022).

In the second study, we focused on two scenarios, with equipped and non-equipped VRUs. In this latter case, we assume that it can be detected by cameras on board of neighbouring vehicles (resp. co-located with a nearby RSU). The VRU detection is then performed on board of the vehicle (resp. at the RSU level) by an image processing unit. For the transmission of CPM messages (UL) and reception of an alarm by the driver (DL), we compared different V2X architectures, namely decentralized, centralized, and hybrid, in

This project has received funding from the European Union's Horizon 2020 research and innovation programme under Grant Agreement 861570.

terms of received alarms by the driver. To this end, we proposed a new metric that we call the probability of driver awareness, which quantifies the effectiveness of each studied architecture in alerting the driver of the presence of a VRU before the accident occurs. Here again, we have shown that equipping a VRU with a V2X radio interface (i.e., a P2V link) is a promising solution for reducing accidents involving VRUs. Compared to I2V and V2N, the P2V link provides the driver with earlier warning to avoid accidents, thereby increasing the VRU's safety (Karoui, Berg, & Mayrargue, Assessment of V2X Communications for Enhanced Vulnerable Road Users Safety , 2022).

This project has received funding from the European Union's Horizon 2020 research and innovation programme under Grant Agreement 861570.

6. Conclusions and Future Work

This report verifies and quantifies the technologies within the developed Demos 2 – 4 of the research project SAFE-UP. Since all demonstrators are different in nature, the conclusions and prospects for future work are presented per demo.

6.1 Demo 2

For Demo 2, extensive measurement campaigns investigating the effect of weather on perception performance have been carried out. In addition to existing work in previous deliverables, this report also analyses the variances of radar reflection points under given weather settings. An increase in variance over measurement distance could be seen; however, the different weather effects are indistinguishable (see Sections 3.2.1.1 and 3.2.2.1.

Two models are developed from these campaigns: the FoV model and the weather filter. The FoV model, which is based on static measurement data, is validated against data from another measurement campaign consisting of data of dynamically moving VRUs. It is found that the predictions of the FoV model do not hold for dynamic cases. Here it is left for future work to improve the FoV model to stronger represent dynamic cases, i.e., moving VRUs.

The weather filter is a simulation-based tool that calculates the detection ranges for various VRU types under different weather conditions and sensor specifications. In this report, the weather filter in the state-of-the-art setting is verified against a potential weather filter with prototype sensors of a future generation. A clear performance improvement can be expected with future hardware.

For both models, it is concluded that testing in the open is required. While the test hall provides a confined environment, it is also restricting and interferes with the sensor signals. Also, another constraint for such model development is the large amount of required testing to gather sufficient data for many cases. Lastly, generalizing the results is challenging since the data is significantly dependent on the sensor hardware and signal processing software.

6.2 Demo 3

Demo 3 has primarily been quantified instead of verified. This is because of the novelty of the employed technology, for which technical specifications beyond the overall system scope (i.e., performing AES and AEB maneuvers in scenarios involving obstructions) are unknown. This is further supported by the project's research scope enabled the partners to employ novel algorithms such as MPC path planning, hybrid VRU prediction, risk-based decision-making, and flatness-based trajectory generation. Here, it is impossible to set technical specifications since these algorithms have neither been in practice individually nor in conjunction within a functional system architecture. However, it has been successfully

This project has received funding from the European Union's Horizon 2020 research and innovation programme under Grant Agreement 861570.

demonstrated with real-world experiments that such a system can avoid accidents in the presented scenarios. Additionally, the vehicle design which is beyond the state-of-the-art can be extended towards higher levels of automation. All necessary components are already embedded in the existing architecture, and many algorithms are currently artificially constrained to only serve in the given scenarios.

A key challenge that was faced is perception performance. Here, an improved perception directly leads to better avoidance rates by more accurate VRU trajectories. The vehicle has been robustified for uncertain perception and trajectory predictions of the VRU; however, further improvements would be welcome to solidify the system's performance.

Another finding constituted another challenge for future work: Are side impacts preferable over frontal collisions? And does human pedestrian behaviour even lead to rear-side collisions? The authors speculate that a side collision might be preferable and less occurring due to the human pedestrian's ability to stop suddenly. This would further strengthen the argument for AES systems.

Lastly, while our system is already constrained to only serve in specific cases, especially lifting the constraint of only performing in-lane AES maneuvers may enhance the avoidance potential of the AES. As said, the system is already designed to perform on higher automation levels than required within this project.

6.3 Demo 4

The focus of the verification of the Demo 4 was to verify the assumptions of WP5. Since WP5 assesses to overall safety benefit in simulation, this report found that the assumptions WP5 made were technically feasible. The assumptions mainly concern signal transmission timing and the correctness of such. Here an emphasis was on communication and the required protocols. Thus, it was also shown that current standardization is sufficient for such technologies.

A major challenge for future work will be the positional accuracy of the VRU. In practice, using just GPS to determine the position is insufficient and will lead to many false positive activations of the AEB.

Still, it has successfully been shown that the communication interface can increase traffic safety, especially for obstruction cases.

6.4 Commonalities

As a last argument, the authors emphasize that the logical next step for increasing overall traffic safety would be to combine the presented technologies into one system. This report can serve as a basis for future verification of such a system.

This project has received funding from the European Union's Horizon 2020 research and innovation programme under Grant Agreement 861570.

7. References

3GPP. (n.d.). Study on LTE-based V2X services, TR36.885 V14.

3GPP TR 37.885. (2018). Study on evaluation methodology of new Vehicle-to-Everything (V2X) use cases for LTE and NR.

5GAA. (n.d.). *C-V2X Use Cases, Methodology, Examples and Service Level Requirements.* Retrieved from https://cdn.everythingrf.com/live/5GAA_191906_WP_CV2X_UCs_v1.pdf

Alvarez Lopez, P., Behrisch, M., Bieker-Walz, L., Erdmann, J., Flötter, Y.-P., Hilbrich, R. L., . . . Wiessner, E. (2018). Microscopic Traffic Simulation using SUMO. *ITSC.*

Balint, A., Schindler, R., Löffler, C., Wimmer, P., Kirschbichler, S., Kolk, H., . . . Mensa, G. (2022). *D5.2 Safety Impact Assessment - Intermediate Report.*

Boban, M., Kousaridas, A., Manolakis, K., & Eichinger, J. X. (2018). Connected Roads of the Future: Use Cases, Requirements, and Design Considerations for Vehicle-to-Everything Communications. *IEEE Vehicular Technology*.

Eckermann, F., M., K., & Wietfeld, C. (2019). Performance Analysis of C-V2X Mode 4 Communication Introducing an Open-Source C-V2X Simulator. *VTC 2019.*

ETSI. (2018). 3rd Generation Partnership Project (3GPP). Technical Specification Group Radio Access Network; Evolved Universal Terrestrial Radio Access (EUTRA); Medium Access Control (MAC) protocol specification.

ETSI TS 103 300-2 V2.1.1. (2020). Intelligent Transport System (ITS); Vulnerable Road Users (VRU) awareness; Part 2: Functional Architecture and Re- quirements definition.

ETSI, E. S. (2019). ETSI EN 302 637-2 V1.4.1. *Intelligent Transport System; Vehicular Communications*.

Guizar, A., Mannoni, V., Poli, F., Denis, B., & Berg, V. (2020). LTE-V2X performance evaluation for cooperative collision avoidance (CoCA) systems. *IEEE Vehicular Technology Conference.*

iMAR. (n.d.). *iTraceRT F402/7 datasheet.* Retrieved from https://www.imar-navigation.de/downloads/TraceRT-F402-7-E_en.pdf

ISO 15288 . (2015). International Organization for Standardization. *Systems and software engineering - System life cycle processes*.

Karoui, M., Berg, V., & Mayrargue, S. (2022). Assessment of V2X Communications for Enhanced Vulnerable Road Users Safety . *IEEE VTC.*

Karoui, M., Mannoni, V., Denis, B., & Mayrargue, S. (2022). Assessment of V2X communications for Enhanced Vulnerable Road Users Safety. *ITSC .*

This project has received funding from the European Union's Horizon 2020 research and innovation programme under Grant Agreement 861570.

Kovaceva, J., Flannagan, C., Kolk, H., Wimmer, P., Schories, L., Ramasamy, E., . . . Castells, J. (2023). *D5.8 Safety Impact Assement Update Report.*

Lin, T.-Y. (2014). *Microsoft COCO: Common Objects in Context.* Retrieved from http://arxiv.org/abs/1405.0312

Löffler, C., Gloger, T., Silvas, E., Muñoz Sánchez, M., Tolksdorf, L., Weihmayr, D., . . . Smit, R. (2021). *D3.3 Vehicle demonstrator for trajectory planning and control for combined automatic emergency braking and steering manoeuvres including system for VRU detection, motion planning and trajectory control to enhance real world performance.*

Löffler, C., Gloger, T., Smit, R., Vogl, C., Tolksdorf, L., Munoz Sanchez, M., . . . Stoll, J. (2022). *D3.6 Vehicle demonstrator for trajectory planning and control for combined automatic emergency braking and steering manoeuvres including system for VRU detection, motion planning and trajectory control to enhance real world performance.*

Löffler, C., Gloger, T., Tolksdorf, L., Weihmayr, D., Vgol, C., Watanabe, H., . . . Koebe, M. (2021). *D3.2 Demo 2 Vehicle demonstrator for object detection in adverse weather conditions.*

Löffler, C., Vogl, C., Labenski, V., Weihmayr, D., Gloger, T., Schwaderer, T., . . . Koebe, M. (2022). *D3.5 Demo 2 Vehicle demonstrator for object detection in adverse weather conditions update.*

Meinila, J. (2007). Celtic WINNER+CP5-026 D5.3 WINNER+ Final channel models.

Mezzavilla, M., Zhan, M., Polese, M., Ford, R., Dutta, S., Rangan, S., & Zorzi, M. (2018). End-to-end simulation of 5G mmWave networks. *IEEE Communications Surveys & Tutorials*.

Mouawad, N., & Mannoni, V. (2021). Collective Perception Messages: New Low Complexity Fusion and V2X Connectivity Analysis. *IEEE Vehicular Technology Conference.*

Munoz Sanchez, M., Elfring, J., Silvas, E., Molengraft, v. d., & Rene. (2022). Scenario-based Evaluation of Prediction Models for Automated Vehicles.

Nikolaou, S., Castells, J., Lorente Mallada, J., Gragkopoulos, I., & Tsetsinas, I. (2021). *D3.4 Demo 4 System for on-time warning provisions to VRUs and drivers in critical conditions.*

Nikolaou, S., Castells, J., Lorente Mallada, J., Gragkopoulos, I., & Tsetsinas, I. (2022). *D3.7 Demo 4 System for on-time warning provisions to VRUs and drivers in critical condiions update.*

Nikolaou, S., Panou, M., Löffler, C., Gloger, T., Gragkopoulos, I., Tsetsinas, I., . . . Muñoz Sanché, M. (2022). *D3.9 Active Safety Systems Specification and Risk Analysis Update.*

Nikolaou, S., Panou, M., Löffler, C., Kupers, B., Sellart, X., Castells, J., . . . Tolksdorf, L. (2021). *D3.1 Active Safety Systems Specification and Risk Analysis .*

This project has received funding from the European Union's Horizon 2020 research and innovation programme under Grant Agreement 861570.

OXTS. (2023, 05). *OXTS Documentation.* Retrieved from https://www.oxts.com/software/navsuite/documentation/datasheets/RT-RangeS_ds.pdf]

Patriciello, N., Lagen, S., Bojovic, B., & Giupponi, L. (n.d.). *An E2E Simulator for 5G NR Networks.* Retrieved from http://arxiv.org/abs/1911.05534

Pei, T., Gugangyu, & Henderson. (2020). Validation of OFDM model in ns-3.

Ploeg, C., Smit, R., Teerhuis, A., & Silvas, E. (2022). Long Horizon Risk-Averse Motion Planning: A Model-Predictive. *International Conference on Intelligent Transportation Systems*, (p. 8). Macau, China.

Redmon, J., & Farhadi, A. (2018). YOLOv3: An Incremental Improvement.

Redmon, J., Divvala, S., Girshick, R., & Farhadi, A. (2016). You Only Look Once: Unified, Real-Time Object Detection. *IEEE Conference on Computer Vision and Pettern Recognition.*

Rouli, L., Cintron, F. J., Mosbah, B., & A., G. S. (2017). Implementation and Validation of an LTE D2D Model for ns-3. *Proceedings of the Workshop on ns-3.*

SAFE-UP. (2023). *Deliverable report D5.3.*

Systems Engineering. (2000). *INCOSE Systems Engineering Handbook.*

This project has received funding from the European Union's Horizon 2020 research and innovation programme under Grant Agreement 861570.

Appendix A: V2X Technologies

V2X technologies have evolved considerably in recent years. In this Appendix, we introduce the most used standards. We give a brief summary about each technology

7.1 ITS-G5/IEEE 802.11p

IEEE 802.11p is based on IEEE 802.11a standard. The physical layer of IEEE 802.11p is based on orthogonal frequency division multiplexing (OFDM), similar to most 802.11 standards. The basic idea is to divide the available frequency spectrum into narrow sub-channels (sub-carriers). The high rate data stream is split into some lower rate data streams transmitted simultaneously over some sub-carriers, where each sub-carrier is narrow band. OFDM is used with 52 sub-carriers, of which 48 are for data and 4 are for pilots.

IEEE 802.11p supports a range of up to 1000 m in different environments such as rural, urban, suburban, and highways supporting maximum relative vehicle speeds of 110 km/h.

The PHY layer reduces OFDM bandwidth from 20 to 10 MHz. IEEE 802.11p uses the binary convolutional coding (BCC) technique, where message bits are convoluted with predefined polynomials to encode the data.

The MAC layer of IEEE 802.11p is based on the Outside the Context of a Basic Service Set (OCB) operation mode, in which authentication, association, and data confidentiality services are not used. This OCB mode of operation is therefore well suited for fast delivery of short messages and a high level of mobility.

7.2 C-V2X

C-V2X is designed to support vehicular communication scenarios. It is based on ProSe (Proximity Services) communications. C-V2X, inherently, employs the SC-FDMA, enabling a UE to access radio resources both in time and frequency domain. C-V2X uses a side-link physical channel based on LTE uplink waveform.

C-V2X technology also supports hybrid automatic repeat request (HARQ) retransmissions, a combination of high-rate forward error-correcting coding (FEC) and ARQ error-control, where corrupted messages are still useful for recovering the original data.

C-V2X is used for the V2V communications use case since communication between vehicles cannot be dependent on cellular coverage. For this purpose, an autonomous Semi-Persistent Scheduling (SPS) mechanism is conceived by 3GPP.

C-V2X supports 10MHz and 20MHz channels. The channel is divided into 1 ms sub-frames and into Resource Block (RB) of 180 kHz each. Mode 4 defines a sub-channel as a group of RBs in the same sub-frame. The number of RBs per sub-channel can vary depending on

This project has received funding from the European Union's Horizon 2020 research and innovation programme under Grant Agreement 861570.

the packet size and the utilized Modulation Coding Scheme (MCS). Sub-channels are used to transmit data and control information

The distributed Semi Persistent Scheduling algorithm enables the selection of radio resources by the node without the assistance of cellular infrastructure. A vehicle reserves the selected resource(s) for a random number of consecutive packets.

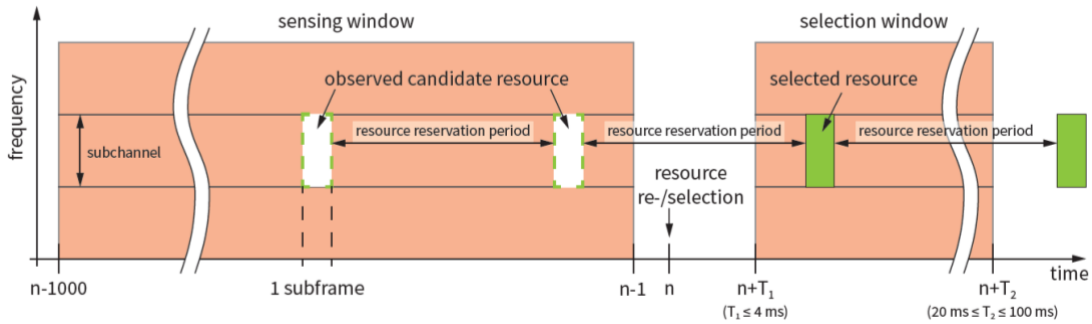

Figure 56: C-V2X Semi Persistent Scheduling (SPS)

When a vehicle wants to reserve new resources, it randomly picks a reselection counter. Following each transmission, the reselection counter is decremented by one unit. When it equals zero, new resources need to be chosen and reserved with a probability (1-P), where P represents the probability of keeping the same resource : P belongs to {0,0.2,0.4,0.6,0.8}. Each vehicle includes its packet transmission interval and the value of its reselection counter in its Sidelink Control Information (SCI). Vehicles utilize this information to evaluate what resources are available when making their reservation to reduce packet collisions.

7.3 IEEE 802.11bd

The IEEE 802.11bd standard is based on the IEEE 802.11ac (i.e. Wi-Fi 5, aka Very High Throughput (VHT)) standard making it more advanced than its predecessor IEEE 802.11p.

In the PHY layer of IEEE 802.11bd, a 10MHz or 20 MHz bandwidth channel is being used for communication, instead of only 10 MHz in IEEE 802.11p. The modulation Coding Scheme (MCS) profile supports 256-QAM. IEEE 802.11bd inherits Multiple-Input Multiple-Output (MIMO) antenna technology from Wi-Fi 5 to allow VHT feature.

The frame structure has been inspired by 802.11 ac frame format, as shown in Figure 57, midambles are introduced.

IEEE 802.11bd uses midambles, which are similar in form and function to preambles except their location within the frame. The preamble is located at the beginning of the frame, and it is used for initial channel estimation. However, for rapidly changing channels, the initial estimate can quickly become obsolete. Midambles are used for channel tracking, so that an accurate channel estimate is obtained for all data symbols. The overhead added by the new

This project has received funding from the European Union's Horizon 2020 research and innovation programme under Grant Agreement 861570.

header and preamble fields is 10 OFDM symbols (80 µs), twice as much as in the 802.11p standard.

As illustrated in Figure 57, midambles are present in the Data field of the NGV (Next Generation Vehicular networks) PPDU after every M Data symbols, where M can be 4, 8 or 16.

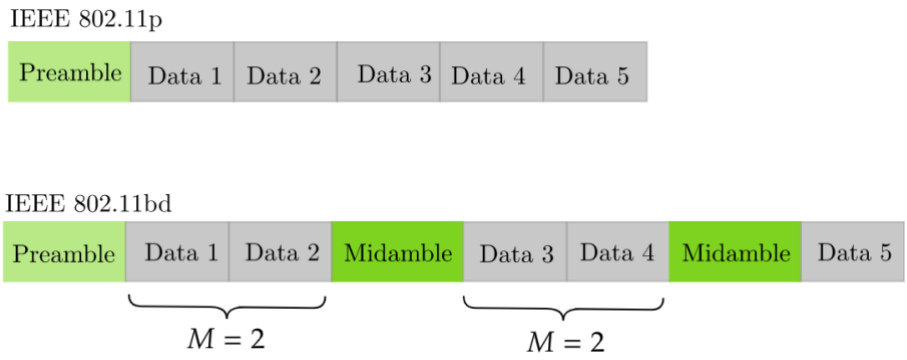

Figure 57: Midambles technique for Doppler shift.

As opposed to 802.11p, IEEE 802.11bd uses low density parity checking (LDPC) coding.

Table 17 summarises the main characteristics of V2X technologies. It also provides a comparative overview of these technologies.

Table 17 Summary of V2X technologies features

Technology Features	IEEE 802.11p	C-V2X	IEEE 802.11bd
Base technology	IEEE 802.11a	LTE	IEEE 802.11ac
Channel coding	BCC	Turbo coding	LDPC
Technique for doppler shift	None	DMRS	Midambles
Subcarrier spacing	156.25 Khz	15 Khz	312.5 Khz, 156.25 Khz, 78.18 Khz
Radio bands	5.9 GHz	5.9 GHz	5.9 GHz, 60 GHz
Retransmission	None	Blind	Congestion dependent
Modes	Broadcast	Broadcast	Broadcast, groupcast

This project has received funding from the European Union's Horizon 2020 research and innovation programme under Grant Agreement 861570.

PHY layer	OFDM	SC-FDMA	OFDM
MAC layer	CSMA	SPS	CSMA

Appendix B: Channel Model

In this Appendix, we describe the channel model that was used for CEA simulations.

We use a channel model called ***Winner + B1*** as specified in (3GPP)**.** WINNER+B1 channel model is based on realistic outdoor scenarios such as the urban Manhattan grid scenario considered by 3GPP. The WINNER channel model allows transitions between different propagation conditions based on line-of-sight (LOS) probability calculation as estimated in (Meinila, 2007)**.**

As described in (Meinila, 2007)**,** B1 model refers to urban micro-cell scenario**.** In B1 model, the height of both the antenna at the Base Station (BS) and at the Mobile Station (MS) is assumed to be well below the tops of surrounding buildings. Both antennas are assumed to be outdoors in an area where streets are laid out in a Manhattan-like grid. The streets in the coverage area are classified as “the main street”, where all locations to the BS are in LOS, with the possible exception in cases where the LOS is temporarily blocked by traffic (e.g., trucks and busses) on the street. Streets that intersect the main street are referred to as perpendicular streets, and those that run parallel to it are referred to as parallel streets. This scenario is defined for both the LOS and the NLOS cases. Cell shapes are defined by the surrounding buildings, and energy reaches NLOS streets as a result of the propagation around corners, through buildings, and between them.

7.4 Line of Sight (LoS) model

It depends on distance from RX and TX denoted as d and breakpoint distance called d_{bp}. Breakpoint distance is the distance from the antenna after which the ground reflected ray interferes with the LOS ray and reduces the field strength as shown in Figure 58.

This project has received funding from the European Union’s Horizon 2020 research and innovation programme under Grant Agreement 861570.

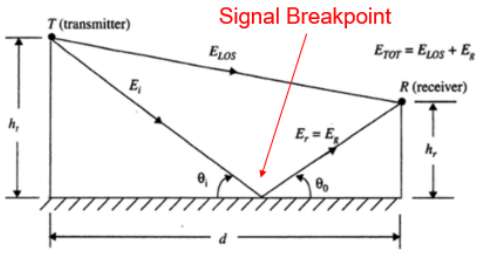

Figure 58: signal ground reflection.

The breakpoint distance, d_{bp} is computed as follows:

$$d_{bp} = 4 * h'_{BS} * h'_{MS} * \frac{f_c}{c}$$

Where: h'_{BS}, h'_{MS} are he effective antenna heights at the BS and the MS, respectively. f_c is the carrier frequency. c is the propagation velocity in free space.

The effective antenna heights: h'_{BS} , h'_{MS} are computed as follows:

$$h'_{BS} = h_{BS} - 1\,m \;, h'_{MS} = h_{MS} - 1\,m$$

Where h_{BS} and h_{MS} are the actual antenna heights, and the effective environment height in urban environments is assumed to be equal to 1.0 m.

In our case, we assume that:

$$h_{BS} = h_{MS} = 1.5\,m,\ f_c = 5.9 * 10^9 Hz\ ,\ c = 3 * 10^8\ m/s$$

LOS model is based on two cases:

- When $3 < \mathrm{d} \leq d_{bp}$

  The path loss is given as follows:

  $$PL[dB] = 22.7 * log_{10}(d) + 27.0 + 20.0 * log_{10}(f_c)$$

- When $\mathrm{d} > d_{bp}$:

  The path loss is given as follows:

$$PL[dB] = 40.0 * log_{10}(d) + 7.56 - 17.3 * log_{10}(h'_{BS}) - 17.3 * log_{10}(h'_{MS}) + 2.7 log_{10}(f_c)$$

7.5 Non-Light of Sight model (NLOS)

The NLOS path loss formula is given as follows:

$$PL[dB] = \left(44.9 - 6.55 * log_{10}(h_{bs})\right) * log_{10}(d) + 5.83 * log_{10}(h_{bs}) + 18.38 + 23 * log_{10}(f_c)$$

This project has received funding from the European Union's Horizon 2020 research and innovation programme under Grant Agreement 861570.

System level simulations require estimates of the probability of line-of-sight as follows:

$$P = \min\left(\frac{18}{d}, 1\right) * \left(1 - \exp\left(-\frac{d}{36}\right)\right) + \exp\left(-\frac{\mathrm{d}}{36}\right)$$

The selection of LOS/NLOS conditions is based on the computation of this probability that depends on distance between RX and TX.

Appendix C: ns3 V2X Modules Architecture

7.6 C-V2X module architecture

We use the C-V2X module introduced in (Eckermann, M., & Wietfeld, 2019), which is based on the LTE Device-to-Device communication simulation model for the ns-3 network simulator introduced and validated in (Rouli, Cintron, Mosbah, & A., 2017). This model implements full protocol stack layers of C-V2X as shown in Figure 59:

- The RRC entity performs the classification of the packets coming from the upper layer into the corresponding Radio Bearer.
- The RLC (Radio Link Control Protocol) entity performs an interface between the MAC layer and the MAC queue for a given bearer.
- PDCP (Packet Data Convergence Protocol) converts data and do some function such as (packet segmentation, data compression, etc.)
- MAC (Medium Access Control) layer performs different operations such as resource scheduling and the multiplexing of MAC SDUs (Service Data Units) from one or different logical channels onto transport blocks (TB) to be delivered to the physical layer on transport channels.
- Basic functionalities of the PHY layer are:
    - Transmit packets coming from the device to the channel.
    - Receive packets from the channel.
    - Evaluate the quality of the channel of the received signal by calculating the received power considering path loss models. Then the packet is judged received or lost based on Signal-To-Noise-Interference Ratio (SINR), MCS and Transport-Block Error Rate (TBLER)

This project has received funding from the European Union's Horizon 2020 research and innovation programme under Grant Agreement 861570.

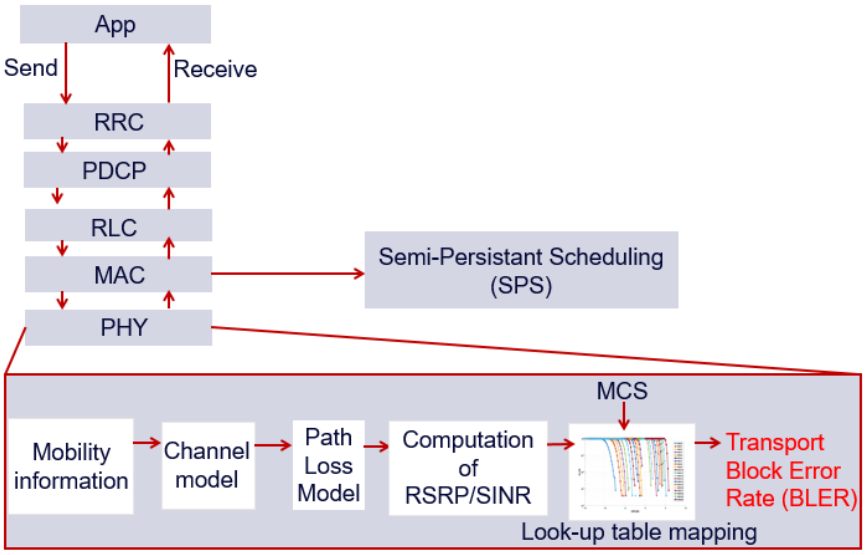

Figure 59: C-V2X full protocol stack in system-level simulation.

7.7 IEEE 802.11- based standards module architecture

IEEE 802.11 –based standards are also modeled in ns-3 using a full stack protocol layer with all upper layers (e.g., application, network and transport layers).

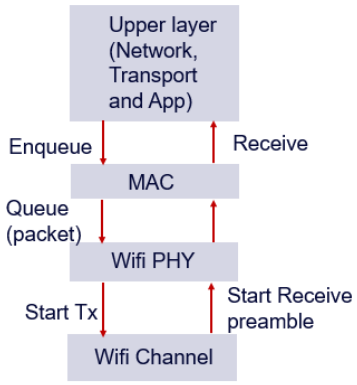

Figure 60: 802.11p/bd simulation module architecture.

ns-3 models the error rate for different modulations. A packet is divided into chunks. Each chunk is related to a start/end receiving event. For each chunk, it calculates the ratio (SINR) between received power of packet of interest and summation of noise and interfering power of all the other incoming packets. Then, it will calculate the success rate of the chunk based on pre-calculated function giving Bit Error Rate (BER) vs. SINR for the given modulation. The success reception rate of the packet is derived from the success rate of all chunks

This project has received funding from the European Union's Horizon 2020 research and innovation programme under Grant Agreement 861570.

7.8 5G LENA module

5G-LENA (Patriciello, Lagen, Bojovic, & Giupponi) is a GPLv2 New Radio (NR) network simulator, designed as a pluggable module to ns-3. The simulator is the natural evolution of LENA, the LTE/EPC Network Simulator, the development started from the mmWave module, and it incorporates fundamental PHY-MAC NR features aligned with NR Release 15 TS 38.300.

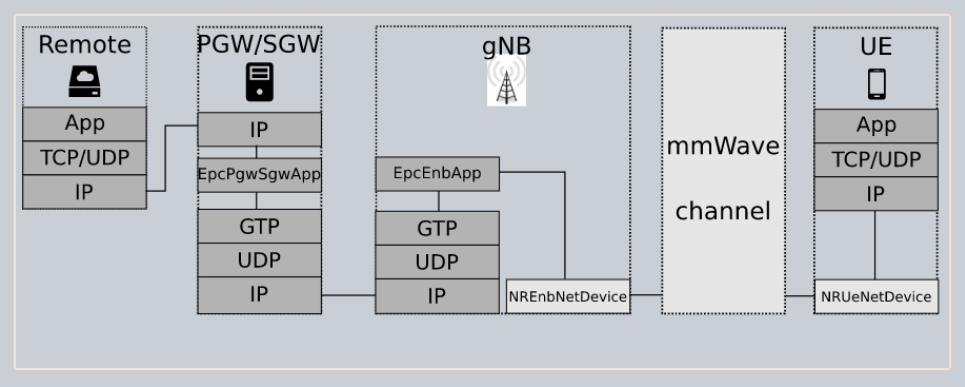

Figure 61: Architectural description of the end-to-end environment

The E2E overview of a typical simulation with the NR model is drawn in Figure 61. On one side, we have a remote host (i.e., server node) that connects to a Service GateWay (SGW)/Packet data network GateWay (PGW), through a link. Such a connection can be of any technology that is currently available in ns-3. Inside the SGW/PGW, the EpcSgwPgwApp encapsulates the packet using the GPRS Tunneling Protocol (GTP) protocol. Through an IP connection, which represents the backhaul of the NR network, the GTP packet is received by the next-Generation Node B (gNB).

The module called mmWave channel (Mezzavilla, et al., 2018) covers in fact a wide range of frequencies between 0.5 and 100 GHz and channel models based on 3GPP TR 38.901. We use it for the frequency of 3.5 GHz.

Appendix D : YOLO Algorithm for Real Object Detection

YOLO employs CNN (Convolutional Neutral Network) to detect objects in real-time. CNN is widely used in the field of image recognition, image classification, object detection, etc. It takes an input image, processes it according to certain classes (e.g., pedestrians, cyclists, cars...).

This project has received funding from the European Union's Horizon 2020 research and innovation programme under Grant Agreement 861570.

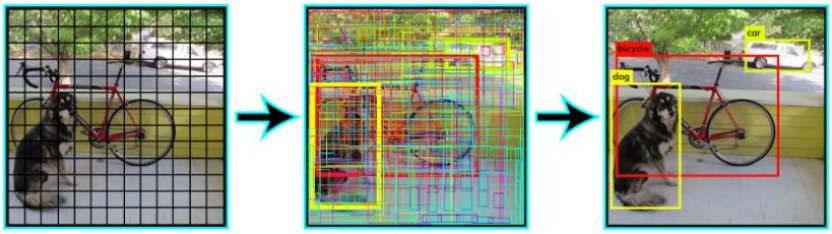

Figure 62 : Yolo grid cells.

As shown in Figure 62, the YOLO algorithm works by dividing the image into N grids, each having an equal dimensional region of SxS. Each of these N grids is responsible for the detection and localization of the object it contains.

Correspondingly, these grids predict B bounding box coordinates relative to their cell coordinates, along with the object label and probability of the object being present in the cell. Each box has one box confidence score. It reflects how likely the box contains an object (objectness) and how accurate is the boundary box. We then deduce **the class confidence score** for each prediction box is computed as:

$$Confidence\ score = box\ confidence\ score * conditional\ class\ probability$$

Where conditional class probability is the probability that the object belongs to class i given the presence of that object

In this document, we focus on unequipped VRU. Indeed, a part of VRUs will not agree to share their position and private data about their locations. In this case, vehicle should be able to detect a VRU presence using vehicle sensor (e.g. Camera, LIDAR, etc...). And this vehicle can broadcast such information to notify other vehicles.

For VRU detection, we use YOLO (You Only Look Once) real-time object detection algorithm. YOLO is a deep learning algorithm in which object detection is performed as a regression problem.

This project has received funding from the European Union's Horizon 2020 research and innovation programme under Grant Agreement 861570.

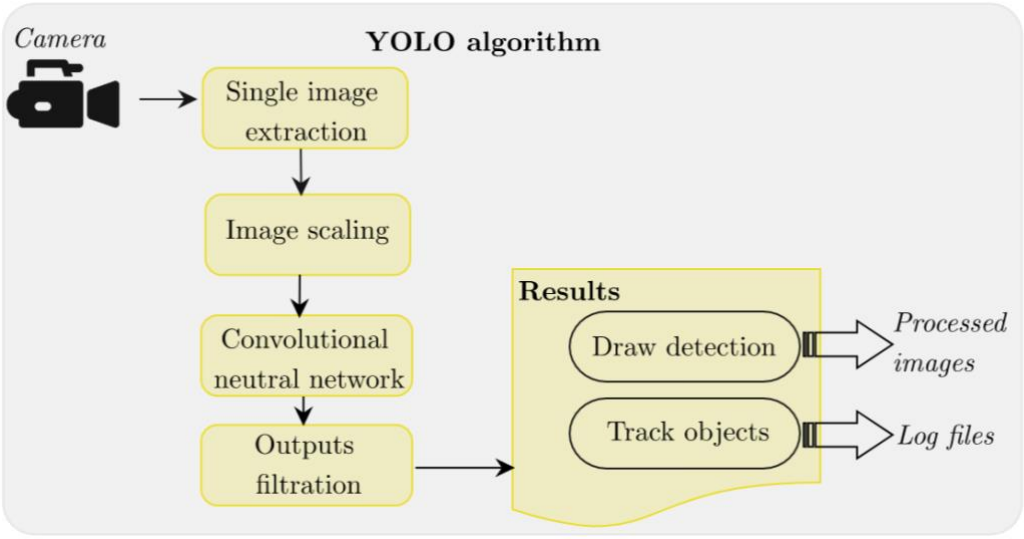

Figure 63: Simplified architecture of YOLO algorithm

YOLO algorithm employs CNN (Convolutional Neutral Network) to detect objects in real-time. CNN is widely used in the field of image recognition, image classification, object detection, etc. It takes an input image, processes it according to certain classes (e.g. pedestrians, cyclists, cars...).

Deep learning CNN models are trained and tested to make correct predictions. Each input image will go through a series of ***convolution layers*** with ***filters***, ***pooling***, ***fully connected layers (FC***) and apply a function to classify an object with probabilistic values between 0 and 1.

Figure 64 shows a complete flow of CNN to process an input image and classifies the objects based on values.

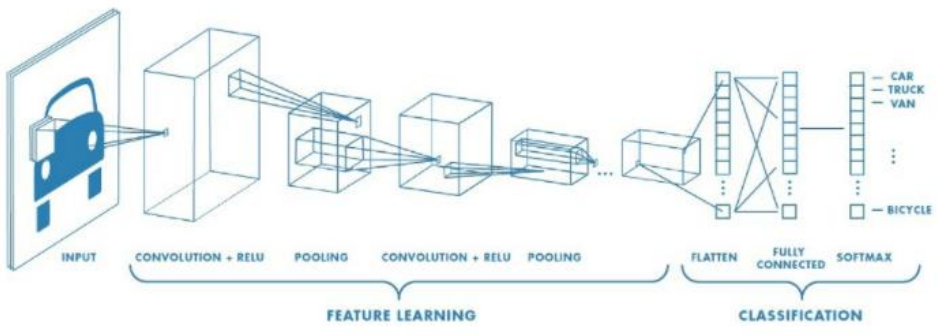

Figure 64: Flow of CNN process in YOLO algorithm.

This project has received funding from the European Union's Horizon 2020 research and innovation programme under Grant Agreement 861570.

The ***convolution layer*** is the first layer to retrieve features from an input image. Convolution preserves the relationship between pixels by learning the characteristics of the image using small squares of input data. It is a mathematical operation that involves two inputs such as the image matrix and a filter or kernel.

Different ***filters*** can be applied to perform operation such as edge detection, blur and sharpen.

Pooling layer section would reduce the number of parameters when the images are too large. Spatial pooling also called subsampling or down sampling which reduces the dimensionality of each map but retains important information.

Fully connected (FC) layer the output matrix of the former operations is transformed into a vector and fed into a neutral network.

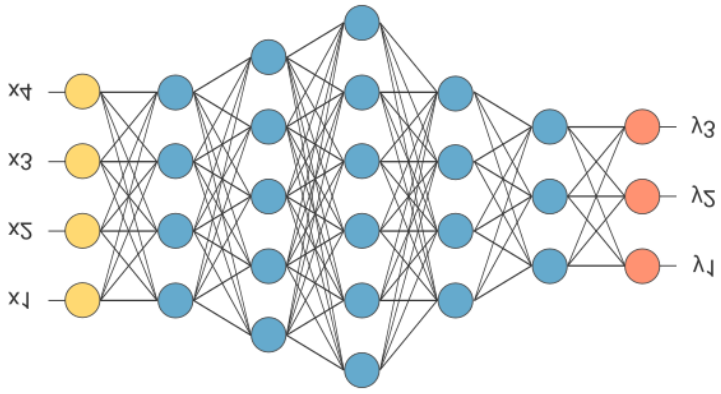

Figure 65: Fully Connected (FC) layer.

In Figure 65, the feature map matrix will be converted to a vector (x1, x2…). With the fully connected layers, these features are combined to create a model. Finally, an activation function such as softmax or sigmoid is used to classify the outputs as pedestrians, cyclists, and cars, etc .

This project has received funding from the European Union's Horizon 2020 research and innovation programme under Grant Agreement 861570.

This project has received funding from the European Union's Horizon 2020 research and innovation programme under Grant Agreement 861570.

This project has received funding from the European Union's Horizon 2020 research and innovation programme under Grant Agreement 861570.